Modeling Climate and Production-related Impacts on Ice-core Beryllium-10

Christy Veeder

Submitted in partial fulfillment of the
requirements for the degree
of Doctor of Philosophy
in the Graduate School of Arts and Sciences

COLUMBIA UNIVERSITY

2009

ABSTRACT

Modeling Climate and Production-related Impacts on Ice-core Beryllium-10

Christy Veeder

I use the Goddard Institute for Space Studies ModelE general circulation model to examine the how beryllium-10, a cosmogenic isotope which has been used in earlier studies as a proxy for changes in solar irradiance, is affected by production-related changes and also by climate-related changes. I focus on changes in total flux and snow concentration over ice-core regions. Experiments involving changes in ^{10}Be production yield latitude-dependent changes in ^{10}Be deposition. Climate-related experiments show changes in ^{10}Be flux and snow accumulation and lead to notable changes in ^{10}Be concentration over both Greenland and Antarctica. This result implies that the effects of climate should be considered carefully when determining production-related impacts on ^{10}Be during periods of large-scale climate change.

Next, I use ModelE to examine ^{10}Be's response to the combined influence of increased production and decreased solar irradiance that are thought to have taken place during historical periods of prolonged solar quiescence, such as the Maunder Minimum. I perform a suite of experiments to capture a range of possible changes in production and irradiance. Production-related changes in ^{10}Be concentration dominate over climate-related changes. Using these results in conjunction with observed values of ^{10}Be, we conclude that the solar modulation parameter ϕ is estimated to have ranged from 280-395 MeV over the course of the Maunder Minimum.

I also perform transient ensemble simulations of the 20th century, with annually varying [10]Be production and a range of climate forcings. Internal variability causes modeled century-scale [10]Be concentration trends to vary from the ensemble mean values by up to 50% and more. Lower levels of unforced variability at the Antarctic locations relative to the Greenland location suggests that, in the model at least, [10]Be from Antarctica may reflect production changes with greater fidelity.

Additionally, I configure the model with daily-varying beryllium production in order to simulate changes in [7]Be caused by an extreme solar energetic particle (SEP) event that took place on January 20, 2005. I also compare the model results with surface observations from January-February 2005. There is generally good agreement between the modeled and observed [7]Be air concentration values. The impact of the SEP event is clearly visible in the polar stratosphere and mesosphere, but at the surface the effects are too small to be distinguishable from the intrinsic variability.

TABLE OF CONTENTS

LIST OF FIGURES

LIST OF TABLES

ACKNOWLEDGEMENTS

 I'm hugely grateful for being given the chance to take on this work, and would like to express my enormous thanks to Gavin Schmidt, my advisor, for making it possible. My words here can only give a crude approximation of how valuable his patience and encouragement have been over the past five years. Despite my complete newness to climate modeling and scientific research, he was always willing to make time for my questions, or wade through thickets of code with me, or reassure me in my moments of frustration that somehow I would manage to figure things out. In addition to our research, Gavin took an active role in my professional development by encouraging me to apply for fellowships, to participate in conferences, to collaborate with other researchers around the world, and anything else that he thought might help me grow as a scientist. His openness and generosity of spirit make him a delight to work with. Thank you, Gavin. I could not have hoped for more in an advisor.

David Rind, my academic advisor, also deserves ample thanks. Throughout my time at Columbia, David has been a steadfast source of reassurance and guidance – always providing helpful advice in navigating the academic requirements of graduate school, and always interested in exploring ideas outside of the realm of climate science. His humor, kindness and curiosity have made an enormous difference over the past five years. I cannot overstate the importance of his endless patience, particularly with my many dynamics questions when I was preparing for my oral exams. His acceptance of my pace of learning has been a crucial ingredient in the accomplishments I have managed to make while at Columbia. I'm also very grateful to him for his support and encouragement in helping me to develop more connections with researchers in solar physics. David, you have been a boon.

I also thank Sidney Hemming, the third member of my advisory committee, for her assiduous guidance in our committee meetings, for helping me prepare for qualifying exams, and for her curiosity and enthusiasm in all contexts. I am grateful to have had her on my team. Many thanks to the Department of Earth and Environmental Sciences, particularly Mia Leo and Missy Pinckert, for their conscientious attention to the bureaucratic and logistical components of graduate school – their skill at keeping everything running smoothly has made me feel lucky to be in their department. Thanks also to Lorenzo Polvani, Jennifer Cho, and the IGERT program for their interest in my development as an interdisciplinary researcher, and their much appreciated financial support.

Many other colleagues and friends have also provided tremendous help: Drew Shindell, Allegra LeGrande, Reto Ruedy, Ken Bell, Jürg Beer, Ulla Heikkilä, Raimund Muscheler, Ilya Usoskin, Ken McCracken, and many others at GISS and DEES have been both kind and generous in sharing their knowledge, data and expertise. I'm also grateful for the camraderie of the DEES graduate students, especially, Jennifer Alltop Aminzade and Sonali Shukla. Scott Giannelli, Peng Xian, Li Liu and Jing Li were excellent officemates, and Peng also helped me greatly by sharing her Latex template for the Columbia dissertation format. Last but not least, profound thanks to my family, and to Wendy Lerner, Micah Boyer, Eric Sprague, and my other close friends who always told me I could do it: your encouragement has been indispensible.

CHAPTER 1

INTRODUCTION

One of the remarkable characteristics of the earth sciences as a field of research is the range of physical scale encompassed by its subdisciplines, involving everything from continental rebound to fission-track dating. In particular, earth scientists are masters at bridging that range of scale – of tenaciously seeking ways to extract information from the microscopic in order to reveal the nature of the colossal. Solar variability is one of the subjects that fall into this category. Since 1610, when sunspot counts were first made with the help of early telescopes, our ongoing interest in learning about the sun has yielded ever more sophisticated observations (Eddy, 1976; Hoyt and Schatten, 1998; Fröhlich, 2004).

Over the past several decades, solar research has taken on a new significance amid growing concern about climate change. Developing a comprehensive understanding of natural climate forcings is essential to understanding the potential scope of anthropogenic climate change, and solar irradiance changes are the most significant natural forcing on centennial timescales. Of particular interest is the existence and magnitude of long-term (multidecadal and longer) changes in solar irradiance, and how such changes might have influenced Earth's climate in the past (and possibly the future as well).

To that end, researchers have turned their attention to the study of natural archives containing cosmogenic isotopes, one of the most promising sources of information about solar variability prior to 1600. These isotopes are produced by collisions between atmospheric particles and galactic cosmic rays (GCRs) (Lal and Peters, 1967). On millennial and longer timescales, Earth's GCR flux is dominated by changes in the strength of the geomagnetic field (Mazaud et al., 1994; Christl et al., 2003); and on shorter timescales (daily to centennial and millennial), GCR flux is mainly controlled by changes in the portion of the Sun's

magnetic flux that extends into the heliosphere, called the open magnetic flux (Beer et al., 1990; Vonmoos et al., 2006; Heikkilä et al., 2008; Lean et al., 2002). The open magnetic flux makes up a relatively small portion of the Suns's total magnetic flux, most of which is comprised of sunspots (areas of intense magnetic activity that inhibit convection and result in reduced surface temperatures) and the bright facular regions that surround them. Changes in the Sun's total solar irradiance (TSI), which is the most significant natural climate forcing on centennial timescales, are controlled by the total magnetic flux. Measurements over the satellite observational period have shown that changes in open magnetic flux are positively correlated to changes in the total magnetic flux and to TSI (Lean, 1994; Lean et al., 2002). Although work is still being done to understand the physical basis for this relationship (Beer et al., 1998; Muscheler et al., 2007), periods of increased solar magnetic activity and TSI (such as sunspot maxima) are associated with increased GCR shielding and reduced cosmogenic isotope production (and vice versa for sunspot minima) (Lal and Peters, 1967; Masarik and Beer, 1999; McCracken et al., 2004).

With the knowledge (albeit imperfect) of this inverse relationship between TSI and cosmogenic isotope production, we can use natural archives such as ice cores and tree rings to learn about how those isotopes have varied in the past, and hopefully get a clearer context for contemporaneous changes in TSI. The isotopes most commonly used for this purpose are beryllium-10 (half-life of 1.5 My), beryllium-7 (half life 53 days), carbon-14 (half-life 5,730 years) and chlorine-36 (half-life 301,000 years).

Cosmogenic isotopes are produced mainly in the stratosphere and upper troposphere. Beryllium isotopes are rapidly scavenged by aerosol particles after production, and are deposited at the surface after an average atmospheric residence time of about a year (Raisbeck et al., 1981; McHargue and Damon, 1991). This relatively short time period between [10]Be's production and its sequestration in ice sheets distinguishes [10]Be from ^{14}C, which becomes incorporated in the carbon cycle after it is produced. The longer residence times of ^{14}C in the atmosphere and ocean acts as a filter that smooths out production changes on

decadal and multidecadal timescales – however on centennial and longer timescales, ^{14}C can be usefully compared to changes in ^{10}Be (Bard et al., 1997, 2007; Beer et al., 2002; Muscheler et al., 2007).

While ^{7}Be's short half life makes it unsuitable for ice-core study, its production function is very similar to that for ^{10}Be, and both are subject to the same transport and removal processes. Also, because ^{7}Be is much easier to measure than ^{10}Be (Beer, 1997), ^{7}Be observations are available in relative abundance and are useful in assessing how well both isotopes are simulated in modeling studies (Koch and Rind, 1998; Koch et al., 2006). Chlorine-36 differs from the beryllium istopes in that, after production, it stays in gaseous form as H^{36}Cl. While ^{36}Cl's half-life is long enough to make it potentially useful for study centennial and millennial timescales, when deposited over ice sheets with low accumulation rates, there is a tendency for H^{36}Cl to become partly re-released into the atmosphere while the snow undergoes the transition to ice (Wagnon et al., 1999; Beer et al., 2002).

Ice cores from Greenland and Antarctica, however, provide a rich and relatively well-dated record of changes in ^{10}Be, with time resolution that allows for study on interannual to centennial timescales. (Beryllium-10 is also found in mid- and low-latitude mountain glaciers, however ice cores from these locations generally cover much shorter time periods, are less complete and are notably more difficult to date; these records are therefore rarely used for studying ^{10}Be [Jürg Beer, personal communication].) However there are several factors that can complicate the process of interpreting ice-core records. Geographically, ^{10}Be data are relatively sparse, and are limited to high latitude locations where climate can exhibit many types of variability. To some degree, however, this problem is mitigated by the greater numbers of ^{7}Be observations that come from a much wider variety of locations. Since ^{7}Be's production and transport are very similar to ^{10}Be's, ^{7}Be observations can to some degree serve as an anolog for understanding certain characteristics of ^{10}Be. Also, since ^{10}Be observations are taken in terms of concentration in ice, they are a composite of changes in ^{10}Be production and changes in climate (Lal, 1987). Any processes that affect

precipitation (like ENSO or the North Atlantic Oscillation) or the atmospheric transport and removal of ^{10}Be can potentially impact ice-core records and obscure the production signal. In many cases, such as large volcanic eruptions which might cause tropospheric cooling and suppress snowfall, these climate effects may occur independently of production-related solar changes. However it is also possible that solar-related climate changes may amplify and occur in tandem with the effects of solar-related production changes – such as during prolonged periods of low sunspot activity like the Maunder Minimum (1645-1715 CE), which was characterized by cooling in the Northern Hemisphere and high ^{10}Be snow concentrations.

Climate effects also impinge on the issue of comparing ice-core records from different locations. While production changes should theoretically have the same effect on high-latitude ^{10}Be everywhere, snow concentrations from different ice cores often have different trends and features, and changes of varying amplitudes (Bard et al., 1997, 2007; Muscheler et al., 2007). These discrepancies raise questions about how to combine different records, and how to attribute changes in production and, potentially, TSI.

General circulation models (GCMs) provide a means by which these questions can be investigated. With their high degree of configurability, and their ability to control isotope production and climate forcing independently, GCMs can serve as laboratories in which we can simulate a wide variety of scenarios and gain insight into the interplay of the different factors involved. The Goddard Institute for Space Studies (GISS) ModelE GCM is well suited for this work since it is able to simulate the response to a wide range of climate forcings including spectrally varying solar irradiance. The GCM configuration used here features a more resolved stratosphere than the standard GCM (Schmidt et al., 2006), which is important for capturing the spatial extent of ^{10}Be production. It also has the capability to simulate daily or annual changes ^{10}Be production for transient simulations. One caveat that should be kept in mind is the limited ability of GCMs to model very site-specific (gridbox-scale) data. Toward that end, in the following chapters we have made an effort to

discuss our results in terms of broader, regional-scale trends when possible, and to provide contextual discussion for simulated gridbox-specific data.

This dissertation describes a series of experiments that have been performed with ModelE for the purpose of better understanding the different ways that changes in climate and changes in cosmogenic isotope production affect ^{10}Be in ice cores. In the remainder of this chapter, I will describe the different production functions used for this work, and also provide some background on the model's performance over Greenland and Antarctica. The second chapter is a published journal article that discusses how simulated ^{10}Be is affected by solar-related and geomagnetic related production changes; and also the impact that increased greenhouse gas concentrations, North Atlantic ocean circulation changes, and persistent volcanism have on Greenland and Antarctic ^{10}Be. The third chapter is an accepted journal article in which we perform a suite of model runs to understand the different ways that ^{10}Be might have been affected by solar-related climate and production changes during periods like the Maunder Minimum. The fourth chapter is a submitted journal article that describes experiments based on transient 20th-century ensemble simulations, designed to shed light on the differences and similarities between ice-core ^{10}Be records from Greenland and Antarctica. The fifth chapter, an accepted journal article for which I am a co-author, describes modeling experiments used to understand how ^{7}Be is affected during periods of extreme but short-lived changes in solar-related production. The final chapter summarizes the main findings from each chapter, the limitations of the work, and prospects for future study.

1.1   Cosmogenic production functions used in this work

Three different cosmogenic production schemes were used to produce the research in this dissertation. All three calculate isotope production according to the relevant degree of GCR shielding, described in terms of the geomagnetic field strength, and the solar modulation parameter ϕ (Gleeson and Axford, 1968). The solar modulation parameter describes

the potential of the Sun, against which charged particles have to propagate through the heliosphere while losing energy. The solar modulation parameter can be denoted either in terms of potential (with units of MV) or in terms of energy (MeV); however since energy is the product of potential times charge, for a proton, numerically speaking, there is no difference between the two usages independent of the units used [Jürg Beer, personal communication]. Since some GCR are alpha particles, the potential in MV is regarded as the more general description.

The first production scheme is described in Masarik and Beer (1999) (and hereafter referred to as MB); the levels of beryllium isotopes that it yields are based on Monte Carlo simulations of the cascade of spallation reactions initiated by GCR particles in the atmosphere. We use the MB production function for the experiments in chapters 2 and 3. (Chapters 2 through 5 each contain a description of the production function used in that chapter.)

The second scheme, used in chapter 4, is a revised version of the MB production function (MB-alpha) improves the treatment of isotope production due to helium nuclei (alpha particles). These alpha particles comprise only about 9% of the incoming cosmic radiation that produces beryllium isotopes. Alpha particles, however, have a smaller charge/mass ratio than the protons that make up the large majority of the GCR flux, and this makes them more resistant to changes in geomagnetic and solar modulation (McCracken et al., 2004). This revision of the effects of alpha particles results in an overall increase in ^{10}Be production of about 10%, and slightly reduces the sensitivity of beryllium isotope production to changes in ϕ. Both the MB and MB-alpha production functions are configured to simulate ^{10}Be and ^{7}Be.

The third production function, used in chapter 5, is from Usoskin and Kovaltsov (2008) (UK08). We use this scheme to model short-term (daily to monthly) production and transport effects, and it is currently only configured to simulate ^{7}Be. The UK08 production function, which is similar to the MB scheme, uses a more recent Monte Carlo simulation tool and yields about twice as much ^{7}Be production overall. The cause of this difference

in yield is still being investigated by the two teams involved, however in this thesis we discuss results in terms of relative values in order to accomodate the differences between the production functions.

The three production functions are compared in figures 1.1 through 1.3. Global ^{7}Be production values for MB, MB-alpha, and UK08 are approximately 0.035, 0.038 and 0.062 atoms/cm^2/s, respectively, for $\phi = 700$ MeV and present-day geomagnetic field strength (Usoskin and Kovaltsov, 2008). Figure 1.1 shows the zonal mean ^{7}Be production for the MB, MB-alpha and UK08 production functions averaged (respectively) over 30 years, 10 years, and 4 years of control-run data. For both the MB simulation and the MB-alpha simulation, $\phi = 700$ MeV. For the UK08 simulation, $\phi = 651$ MeV, which partly accounts for the higher amounts of ^{7}Be in that run. The higher levels of ^{7}Be in the run using MB-alpha (relative to MB) are also visible.

Figures 1.2 and 1.3 compare the concentrations of ^{7}Be in surface air for the three production schemes. Due to the interactions between solar magnetic and geomagnetic shielding, the regions of greatest beryllium isotope production are in the mid- to high latitudes and, as mentioned earlier, mostly in the stratosphere. The co-location of these high production regions with midlatitude storm tracks facilitates the transfer of cosmogenic beryllium from the stratosphere to the troposphere, and also the deposition of beryllium at the surface; this can be seen most clearly in panel c. Regions of higher concentrations also correspond to the areas of the globe with higher elevation, such as Greenland, the Rockies and the Himalayas. More importantly, despite the differences between the control runs, figures 1.2 and 1.3 qualitatively show that although the magnitudes of ^{7}Be vary from production scheme to production scheme, the patterns of ^{7}Be and the relative distributions are very similar for all three schemes. This relative constancy can be seen in panel d, which shows the departure from the percent increase (from MB to UK08) in global mean ^{7}Be surface air concentrations. (The change from MB-alpha to UK08 is very similar and not shown.) Except for some high values near the equator, the departure is fairly constant, with

Zonal Mean 7Be Production
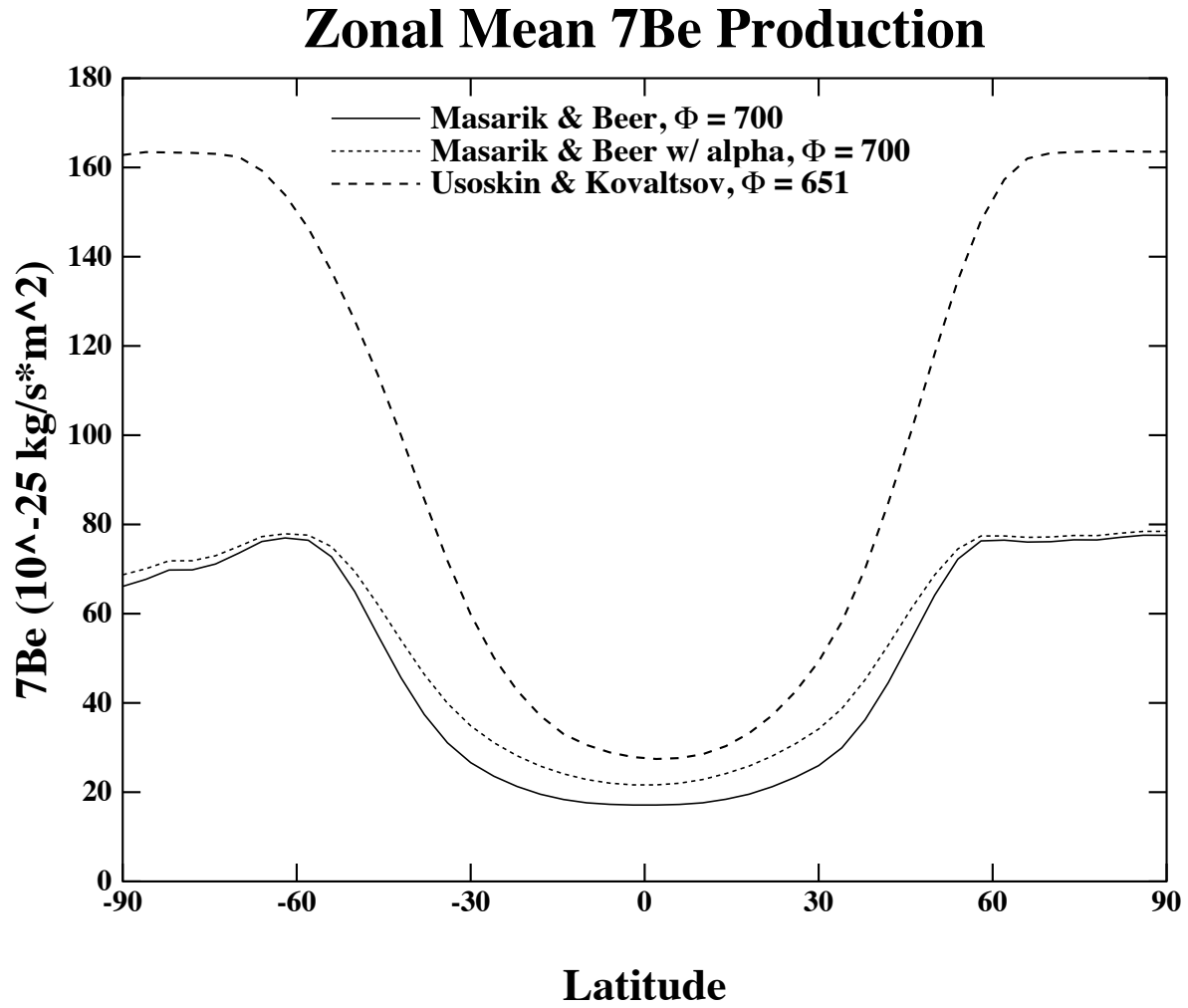
Figure 1.1: Zonal mean ^{7}Be production for the three different production functions.

values that are generally close to the percent increase in global average production from MB to UK08 (about 78%). This qualitative agreement allows us to compare results from different experiments with greater confidence. In the following chapters, results are typically discussed in terms of percent change from the control scenario, which minimizes the differences.

(a) 7Be surface concentrations, Masarik & Beer

(b) Masarik & Beer w/ alpha
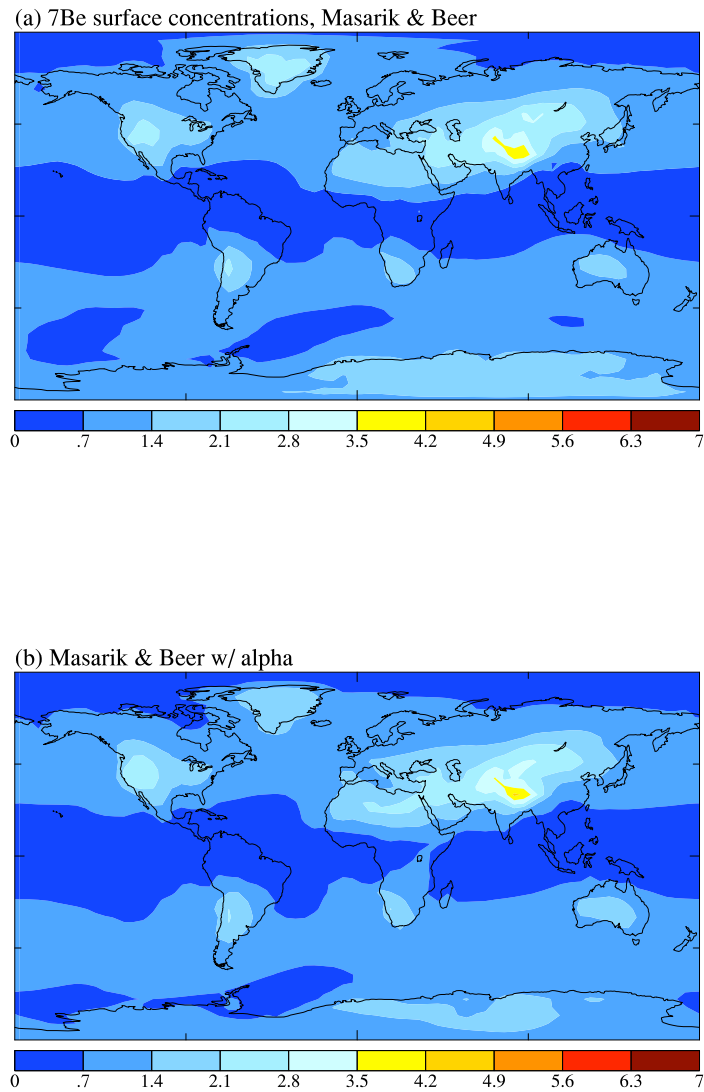
Figure 1.2: Climatological surface air concentrations of ^{7}Be for (a) the MB production function and (b) the MB-alpha production function. Units are in 10^{-22} kg/kg air.

(c) Usoskin & Kovaltsov

(d) Departure from global mean % increase in 7Be surf. air conc.
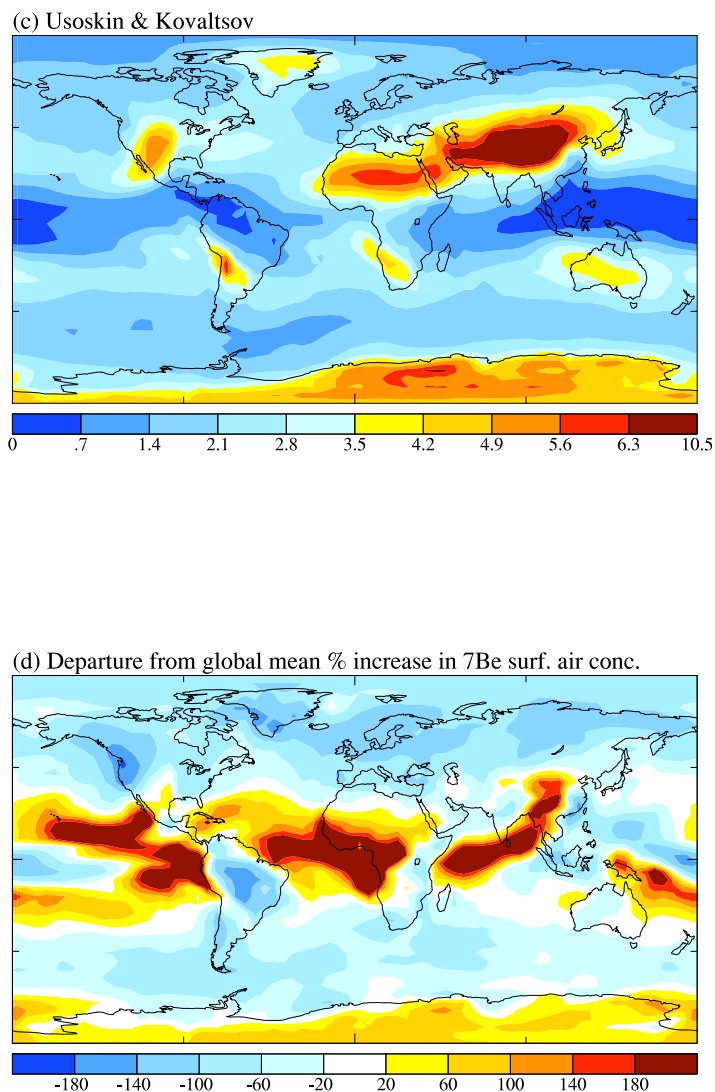
Figure 1.3: Panel (c) shows climatological surface air concentrations of ^{7}Be for the UK08 production function (units are in 10^{-22} kg/kg air). Panel (d) shows the departure from the percent increase (from MB to UK08) in global mean ^{7}Be surface air concentrations (about 78% more).

1.2 Assessment of simulated climate over Greenland and Antarctica

Given the importance of ice core regions to the results of this thesis, we compare model output with automatic weather station (AWS) data and recently published climatological observations.

1.2.1 Model description

We use a version of the Godard Institute for Space Studies (GISS) ModelE general circulation model (GCM) that is configured with 20 vertical layers and medium (4° latitude x 5° longitude) horizontal resolution (Schmidt et al., 2006). The simulations use present-day climatological sea surface temperatures and greenhouse gas concentrations. After a one-year spin-up period, the model was run for five years. Results from a higher-resolution (2° latitude x 2.5° longitude) run (with the same configuration) are also compared with the original medium-resolution simulation.

1.2.2 Greenland

For Greenland, we compare model output for monthly mean temperature, surface pressure and humidity (figure 1.4) with AWS data collected at GISP2 (Summit) between 1989 and 1995. For the inland regions of both Greenland and Antarctica, air actually warms up to about 1 km above the surface, at which point adiabatic cooling with height is seen. This inverted temperature profile complicates the process of correcting for differences between modeled and real-world altitudes. For instance, if one were modeling a location somewhere in the Rockies and topographical smoothing in the model produced a simulated altitude that was lower than the actual altitude, the straightforward adiabatic temperature profile there would allow one to adjust the simulated temperature by calculating and applying a positive lapse rate. However, it makes less sense to use this process in Greenland or Antarctica,

where temperature inversions exist. While applying an adiabatic lapse rate in these cases is not necessarily helpful or meaningful, both adjusted and unadjusted surface temperatures are presented here for the sake of comparison.

Topographical smoothing in the model results in a simulated elevation that is approximately 230 meters below Summit's actual elevation (3205 m). In this case, adjusting the modeled temperature results in a better agreement with observations, although this may be coincidental (as explained above). In making the adjustment, a value of -6.5° C/km was used. Hanna et al. (2001) use -8° C/km, which does not significantly improve the agreement.

Surface pressure benefits greatly when adjusted for altitude (done by multiplying the observed pressure by $\exp(-.23/H)$) although adjusted model pressure is too high during the winter, which suggests that there may be some issues with the location and magnitudes of the model's storm tracks. As for humidity, observations are given in terms of relative humidity at the surface. The model provides information on specific humidity, temperature and pressure at the surface, which were used to calculate surface relative humidity. As can be seen in figure 1.4, calculated relative humidity values fail to reproduce the seasonal cycle and are too high throughout the year, especially during the winter (despite the model's high bias with surface pressure). This discrepancy in relative humidity is largely due to the exponential relationship between temperature and saturation vapor pressure, and the problem of calculating relative humidity from averaged temperature values. Alternatively, I calculated "observed" specific humidity values using observed relative humidity and temperature. The monthly mean results agree strongly with the model's simulated specific humidity, but given the very strong dependence on temperature, this match is the easier target. Despite the high relative humidity values in the model, we have found that simulated ^{10}Be snow concentrations at Summit are sometimes several times higher than observed values (see Chp. 2). The high modeled concentration values at Summit in these cases seem to be mainly due to low accumulation, implying that the model's high surface

pressure bias has a dominant effect in these simulations. At Dye 3, however, both modeled accumulation and ^{10}Be snow concentrations are in closer agreement with observed values (see Chp. 4).

The model's ability to simulate temperature, pressure and humidity should be reflected in the model's success at simulating Greenland's precipitation and accumulation. These two quantities are characterized by high regional variability, which in turn is caused largely by the combined effects of Greenland's topography and two semi-permanent low-pressure systems: the Icelandic low to the southeast and the Baffin Bay low to the west. The Icelandic low directs relatively moist air from the Atlantic toward the southeast coast. The steeply rising topography causes some air to be deflected along the coast while the rest flows inland toward Summit, depositing its moisture along the way. Relatively little precipitation reaches beyond Summit to the north or west. Greenland's west coast receives moisture in a similar manner from the Baffin Bay low. The westerly winds from this pressure system originate over North America, and so are relatively dry during the winter (when the land is cooler than the ocean) and moist in the summer. In the annual mean, the overall result is high precipitation on the southeast and western coasts and reduced precipitation above 2500 m. Over the leeward, northeastern part of the ice sheet, precipitation is minimal. A more detailed description of these wind fields is given in Ohmura and Reeh (1991).

Simulated precipitation and accumulation over Greenland are shown in figures 1.5 through 1.8, which can be compared with observed values shown in figure 1.9 from Bromwich et al. (1998). Due to low levels of evaporation and sublimation inland, precipitation and accumulation over the ice sheet closely resemble each other. Qualitatively, the distribution of modeled precipitation also agrees well with the observed values, in keeping with the model's performance with respect to temperature and pressure, however model accumulation values for the Summit gridbox (0-20 cm/yr) are lower than the observed values (about 25 cm/yr). Also, on the southeast coast, model accumulation is negative, contrary to observations. This is due to the fact that in the model these are ocean gridboxes

rather than land gridboxes. The higher-resolution model has improved coastal topography and does not exhibit negative accumulation in these gridboxes, and is also more successful at simulating the higher levels of accumulation around the southeast region of the coast.
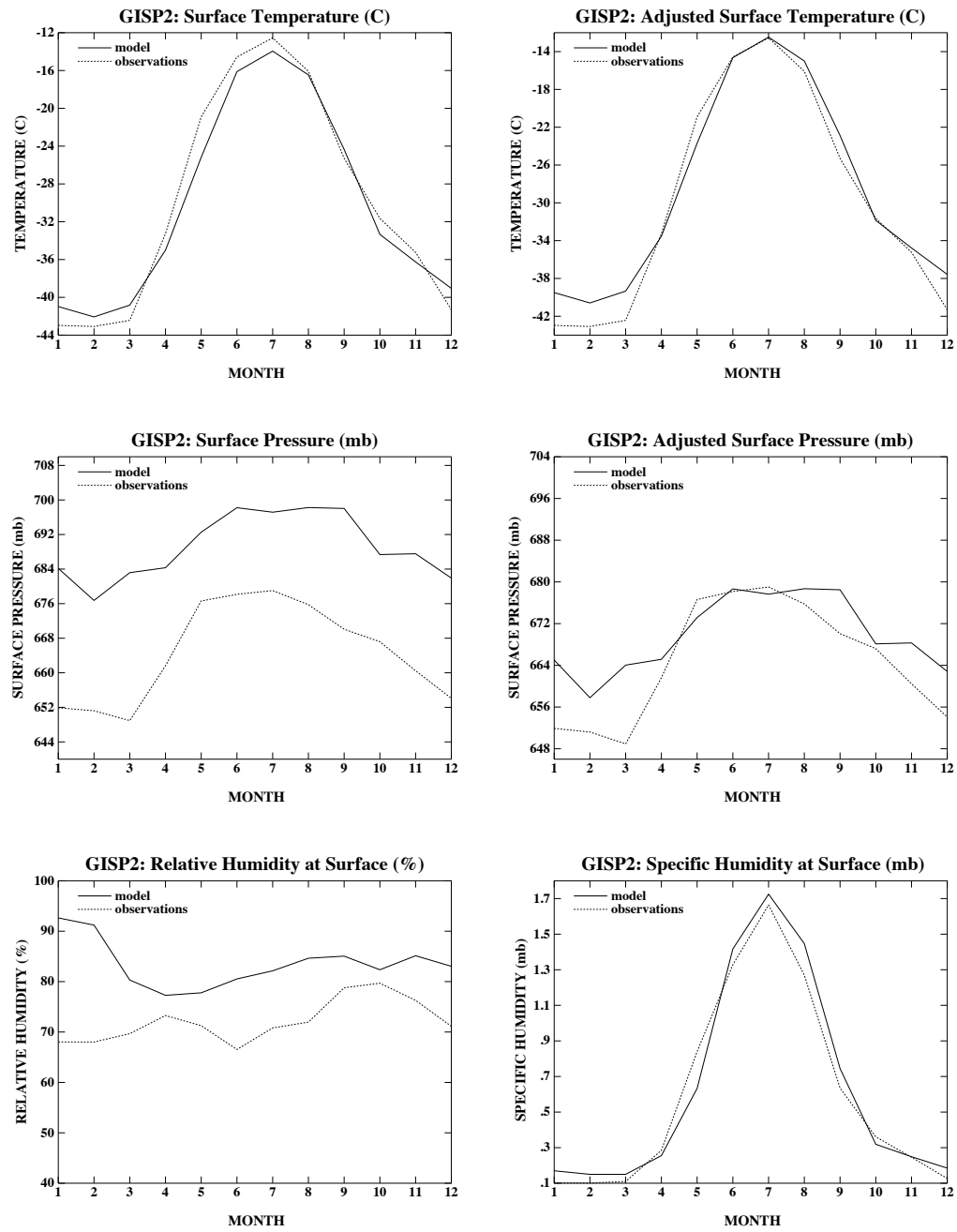
Figure 1.4: Monthly mean temperature, pressure and humidity at Summit, Greenland. Observations are from the National Climate Data Center website.

Greenland precipitation (cm/yr)
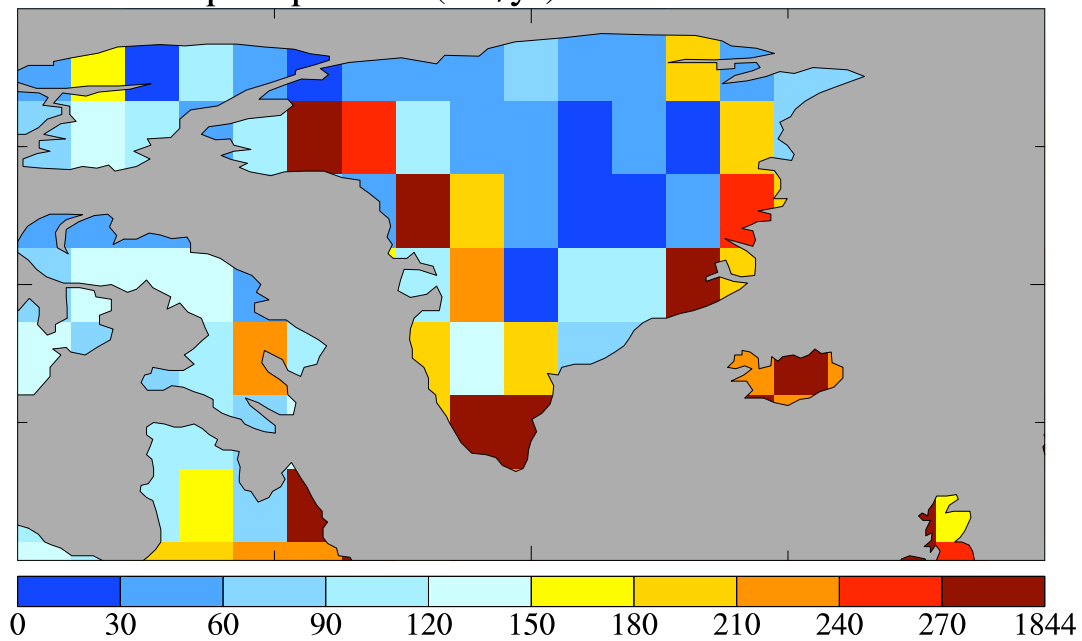
Figure 1.5: Annual mean precipitation over Greenland from the medium-resolution model. Units are in cm/yr.

Greenland accumulation (cm/yr)
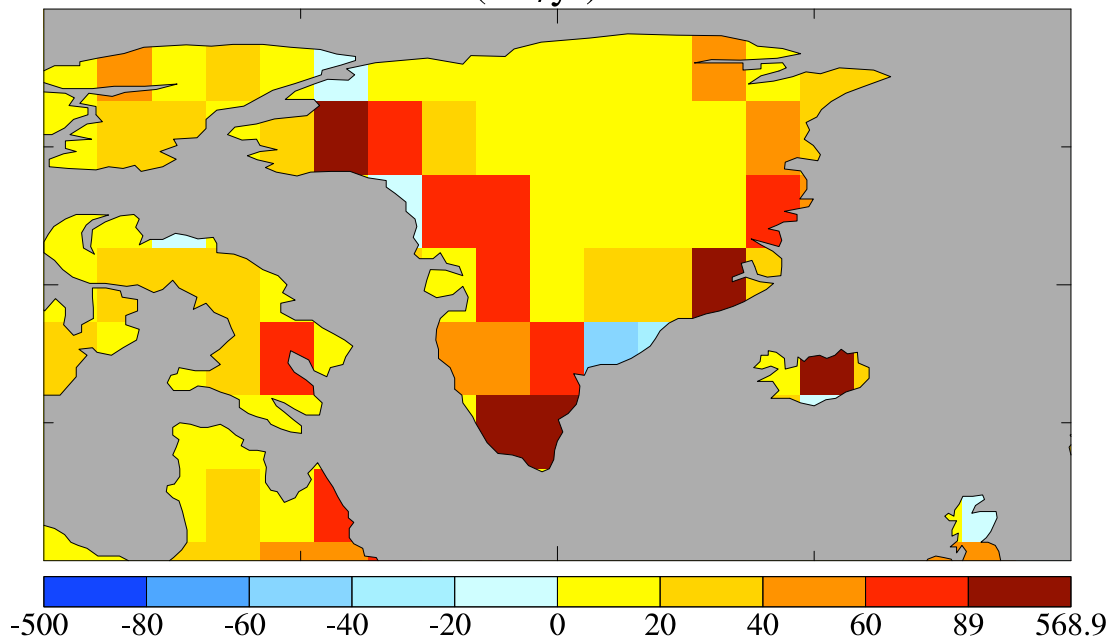
Figure 1.6: Annual mean accumulation over Greenland from the medium-resolution model. Units are in cm/yr.
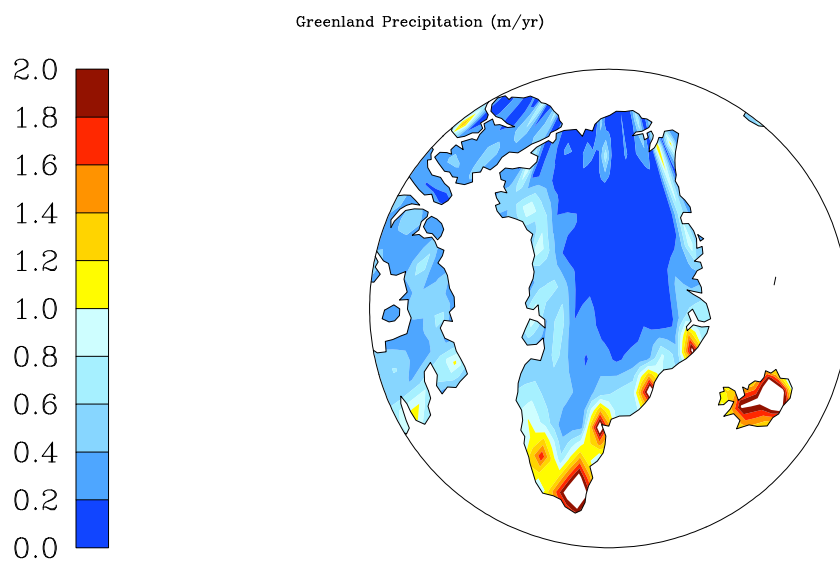
Figure 1.7: Annual mean precipitation over Greenland from the high-resolution model. Units are in m/yr.
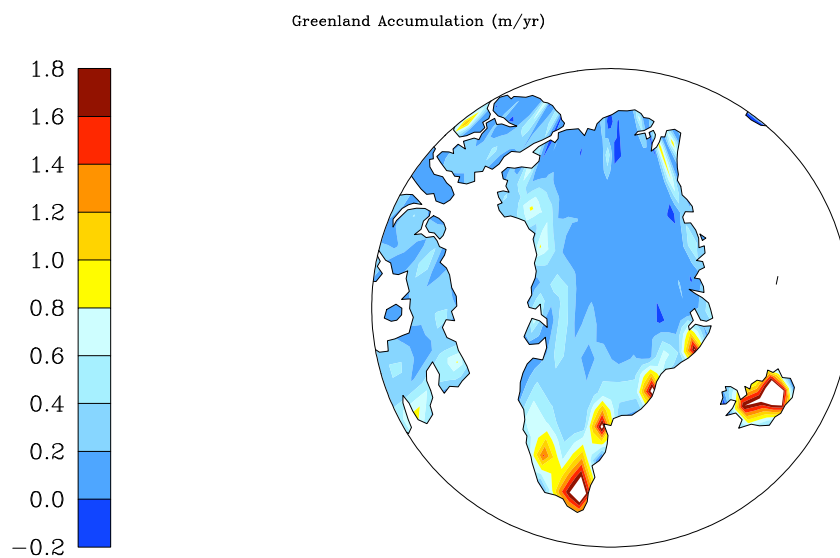
Figure 1.8: Annual mean accumulation over Greenland from the high-resolution model. Units are in m/yr.
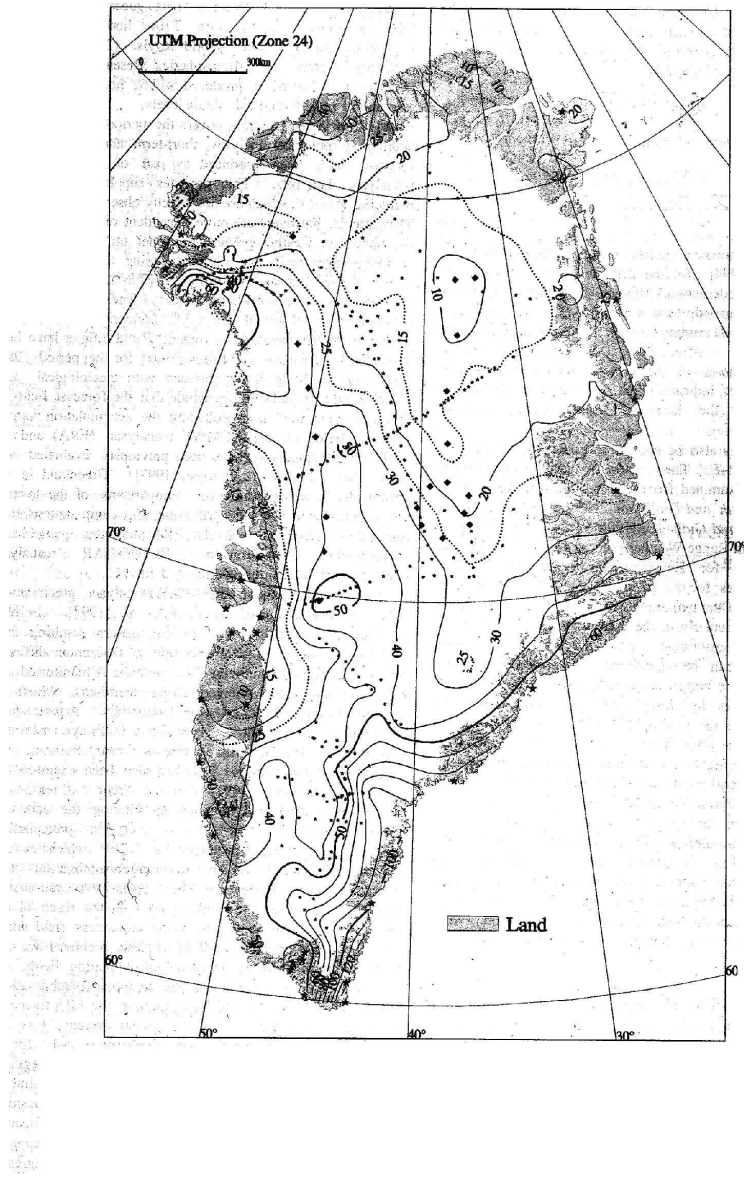
Figure 1.9: Csathó-PARCA accumulation data for Greenland, from Csathó et al. (1997) (figure 3 in Bromwich et al. (1998)). Units are in cm/yr.

Taken together, the results suggest that the model does a reasonable job of simulating climatology over the Greenland ice sheet, although the high level of spatial variability that characterizes Greenland's climate reduces the probability that modeled values for any given gridbox will strongly reflect the contents of a particular ice core.

1.2.3   Antarctica

Of the Antarctic locations for which AWS observations were available, Law Dome and Vostok have the most abundant data, and temperature data is available for a number of locations. Genthon (1994) mentions that in Fortuin (1992), the lapse rate is calculated to be about -5° C/km around the Antarctic coast and -14° C/km inland. Both values have been applied to temperature data for all individual locations, with mixed results; the seasonal cycle, however, is well represented everywhere. (For a map with locations, see figure 1.12.)

Figure 1.10 shows Antarctica's annual mean surface temperature distribution, which can be compared with observations from Tzeng et al. (1994) (figure 1.11). Temperatures appear to be in good agreement in the east around the coast, but too warm inland and to the west. The monthly mean temperatures at Law Dome and Mawson (figures 1.13 and 1.15) confirm this, as do the temperatures at Halley, Vostok and the South Pole (figures 1.15 and 1.14). A protrusion of colder air in the model at 90° W allows simulated Byrd temperatures to match observations. McMurdo's position next to the Ross Sea may account for its relatively cold simulated temperatures.

Annual mean surface air temperature (C)
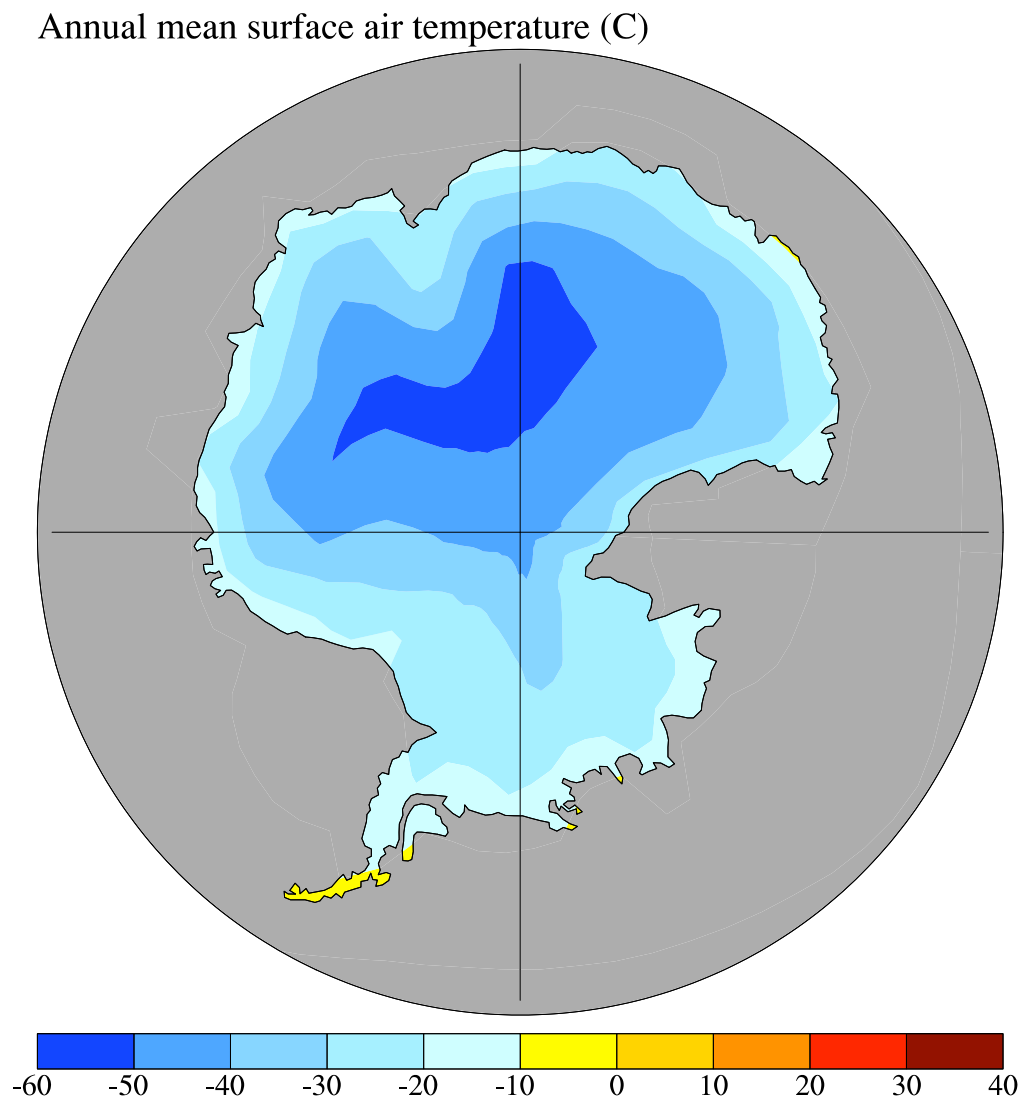
Figure 1.10: Annual mean temperature over Antarctica in degrees Celsius.
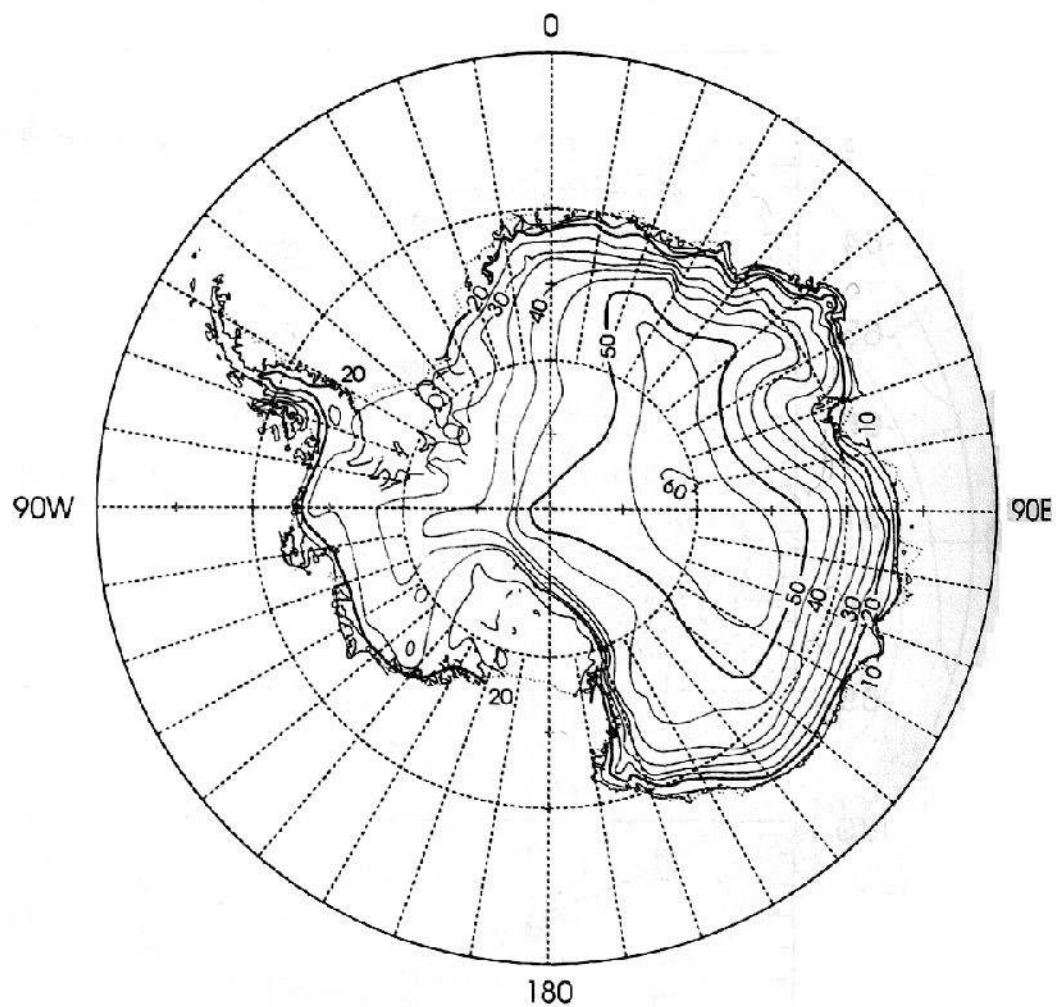
Figure 1.11: Observed annual mean temperature over Antarctica in negative degrees Celsius, from Giovinetto et al. (1990) (figure 3b in Tzeng et al. (1994)).

AWS locations
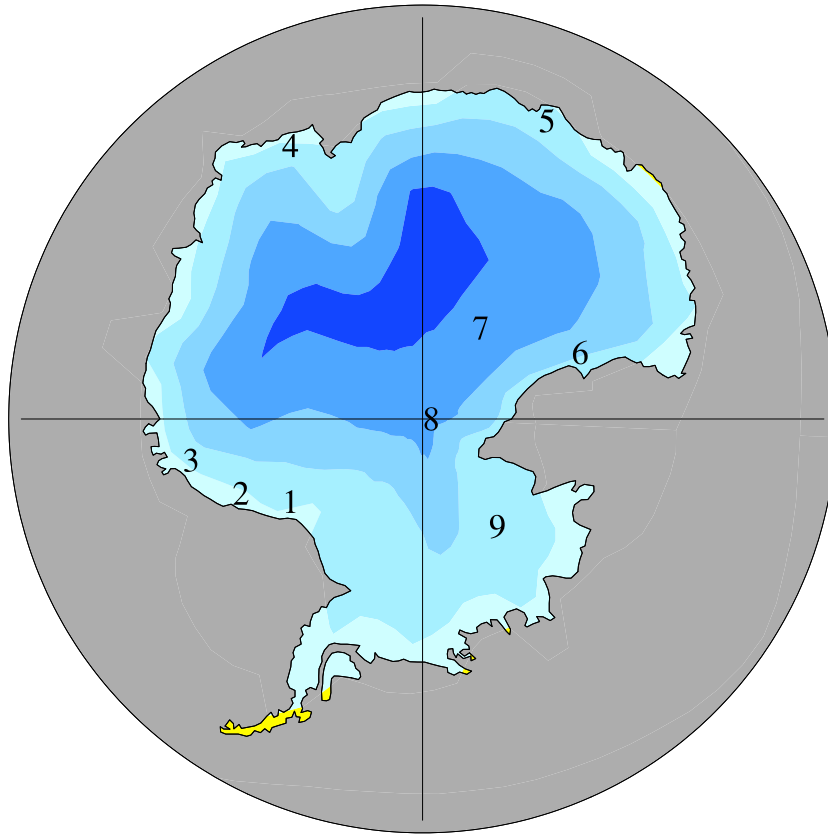
Figure 1.12: Antarctic weather station locations: 1 = Base Belgrano, 2 = Halley, 3 = Neumayer, 4 = Mawson, 5 = Law Dome, 6 = McMurdo, 7 = Vostok, 8 = South Pole, 9 = Byrd.

In general, areas over the Antarctic plateau are too warm, and coastal performance is inconsistent. Genthon (1994) blamed underestimated model albedos for the lack of appropriately cold temperatures. The GCM's albedo has since been raised to 0.8 (in Genthon's recommended range), although this would have no effect during austral winter, when temperature discrepancies are the greatest. Another possible cause of the warm inland temperatures could be excess amounts of high-level clouds, which could receive longwave radiation and emit to space at a lower temperature. According to cloud climatology data from Rossow and Schiffer (1999), cirrus and cirrostratus cloud are estimated to cover for the south polar region at 8.7% and 3.4% respectively. These cloud types are defined as having

cloud-top pressures between 440 and 50 mb. The modeled percentages are approximately the same, with the percentage of high-altitude ice clouds over the pole ranging from 2-9% in the medium-resolution model and 1-7% in the high-resolution model. A more likely explanation for the warm temperatures might be that too much coastal air is being advected inland, which is plausible considering the smoothed nature of model topography. Other dynamics-related issues, such as lack of a realistic temperature inversion or lack of kata-batic winds (both of which stem from the difficulties of accurately modeling near-surface conditions) may also contribute to the warmer modeled temperatures.

Modeled pressure at Law Dome (figure 1.13) is about 80 mb higher than the observed values, and is still about 15 mb higher than observations even after being corrected for altitude. As with Greenland, this may be due to the model not generating enough storms throughout the year. Despite the high pressure, modeled precipitation and accumulation agree fairly well with observations (figures 1.16, 1.17, and 1.18). Specific humidity was calculated from averaged temperature and relative humidity values. As mentioned earlier, there are problems with this method, nonetheless the agreement between observed and simulated values improves significantly when the calculation is applied, although modeled relative humidity is too high during austral summer and too low during austral winter. This is probably related to the fact that austral summertime temperatures at Law Dome are warmer than observations by about $5°$ C. The low simulated humidity during austral winter may also be related to the model's inability to simulate blowing snow, which can substantially increase surface humidity values (Mann et al., 2000).
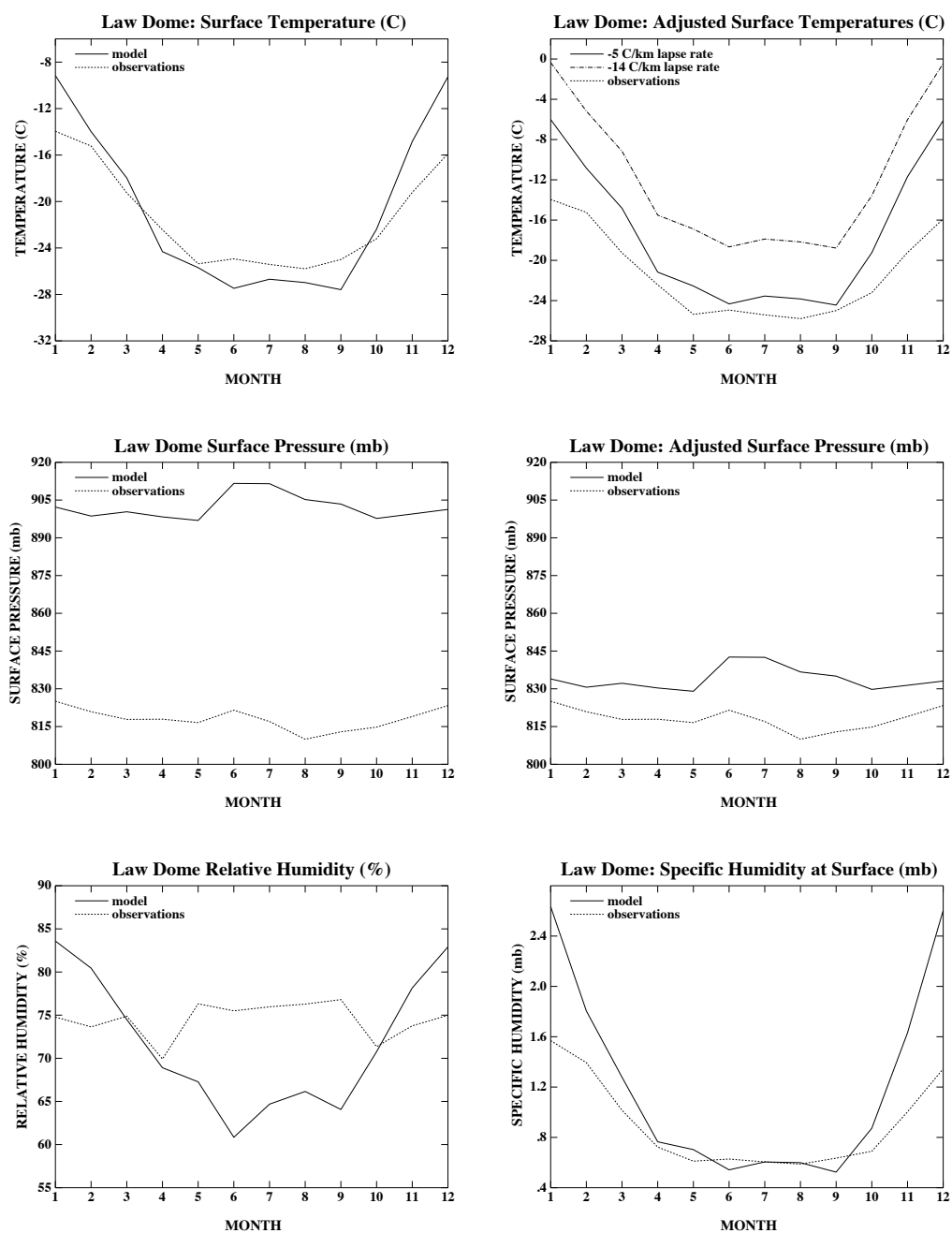
Figure 1.13: Monthly mean temperature, pressure and humidity at Law Dome, Antarctica. Observations are from the Australian Antarctic Division web site. Temperature data were collected from 1986-1998; pressure data were collected from 1987-1995 and humidity data were collected from 1998-2003.
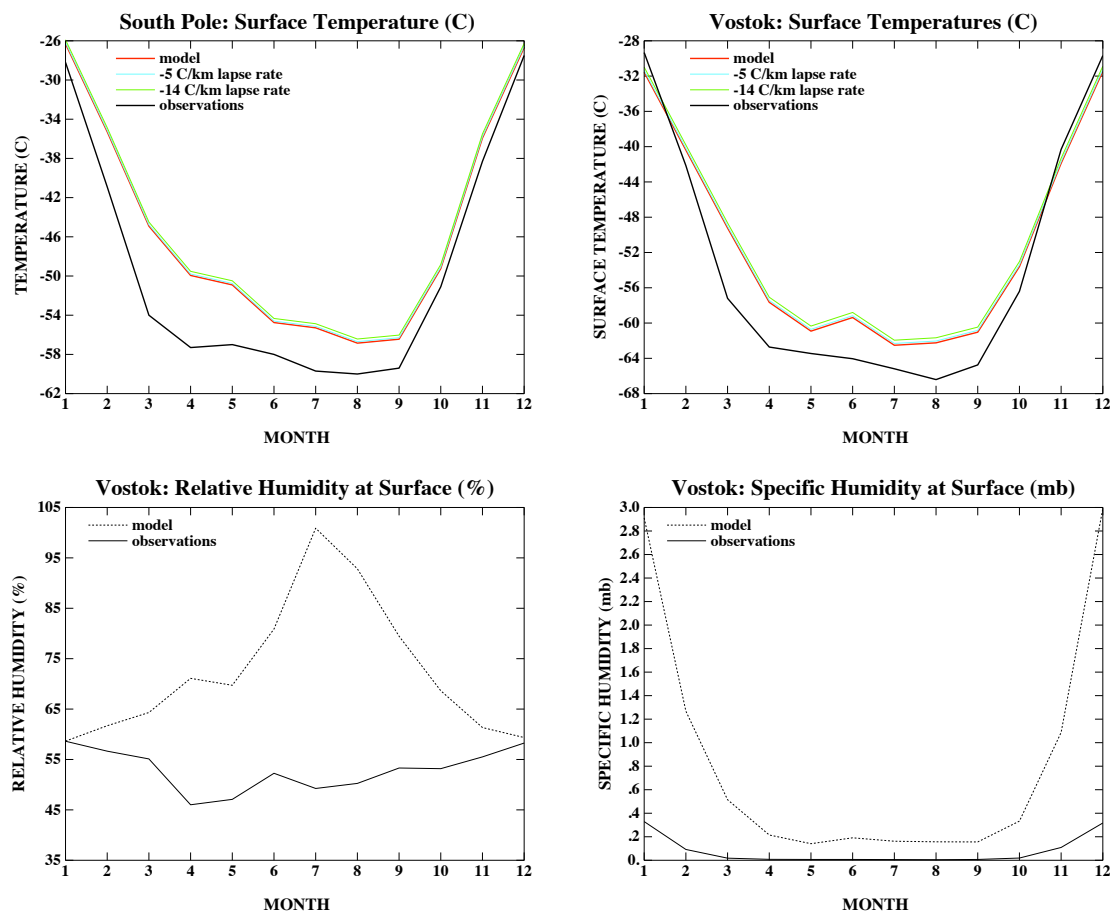
Figure 1.14: Monthly mean temperature at South Pole and Vostok; and monthly mean humidity at Vostok. Observations are from Paul Ward, www.coolantarcita.com. South Pole and Vostok temperature data were collected from 1957-1988. Vostok humidity data were collected from 2000-2004.
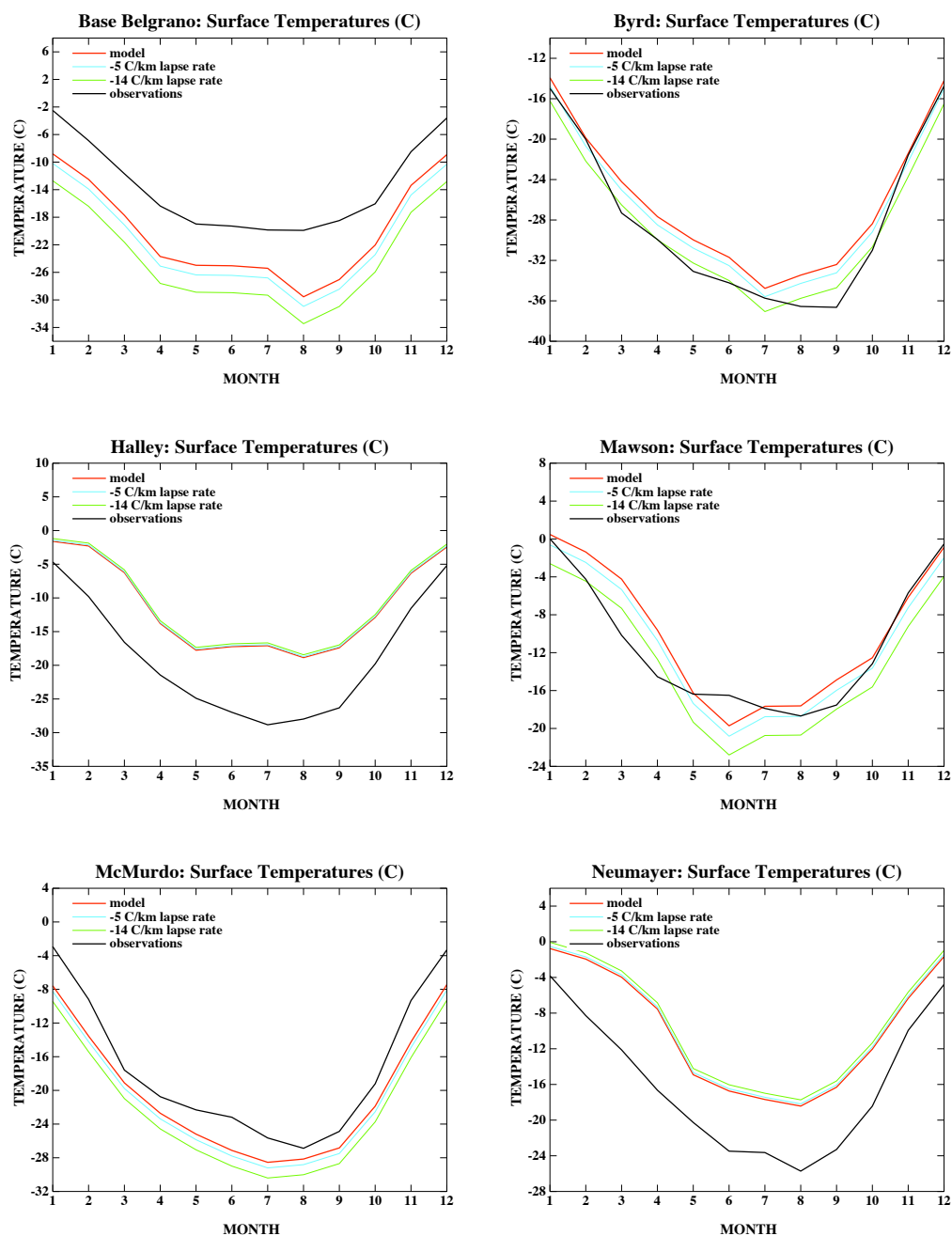
Figure 1.15: Monthly mean temperature at different Antarctic locations. Observations are from GISTEMP data (Hansen et al., 2001).
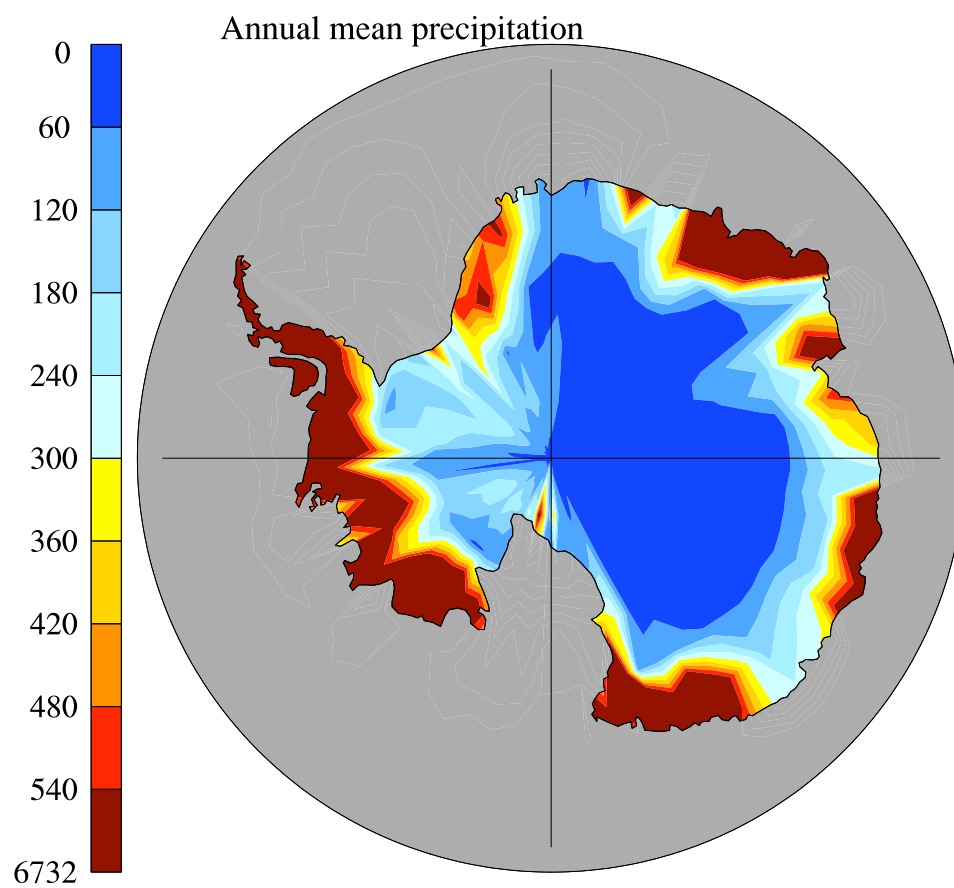
Figure 1.16: Annual mean precipitation from the medium-resolution model, in kg/m^2/yr.
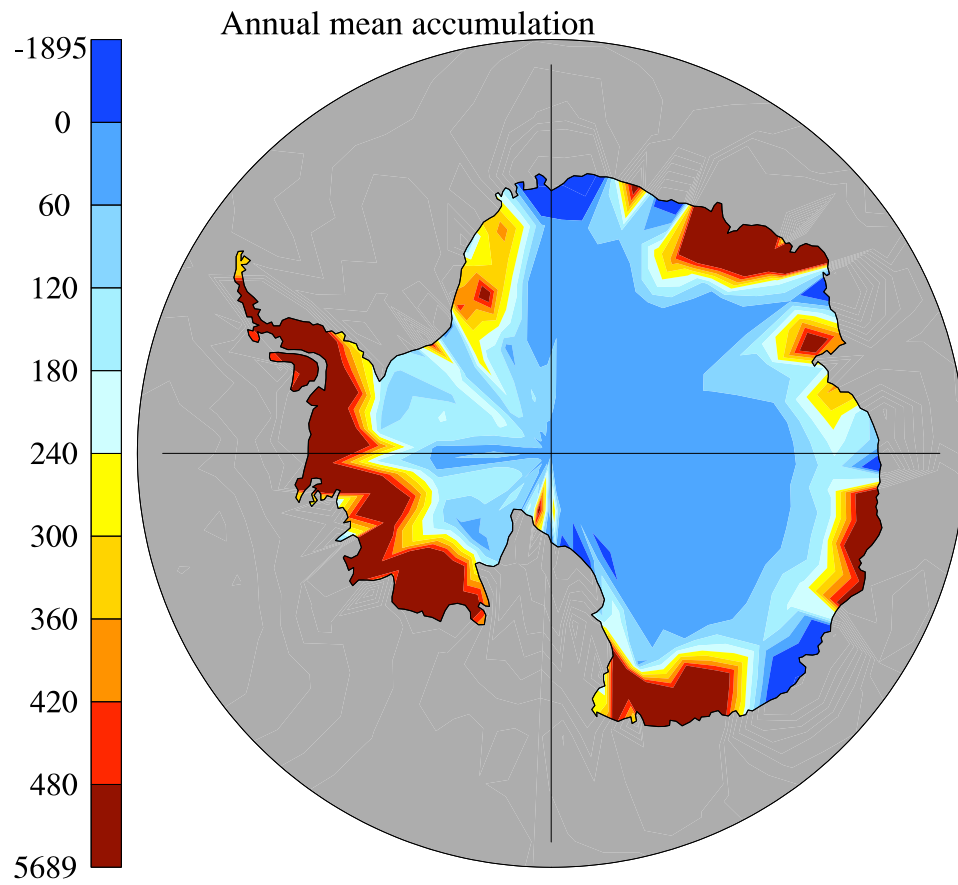
Figure 1.17: Annual mean accumulation from the medium-resolution model, in kg/m^2/yr.
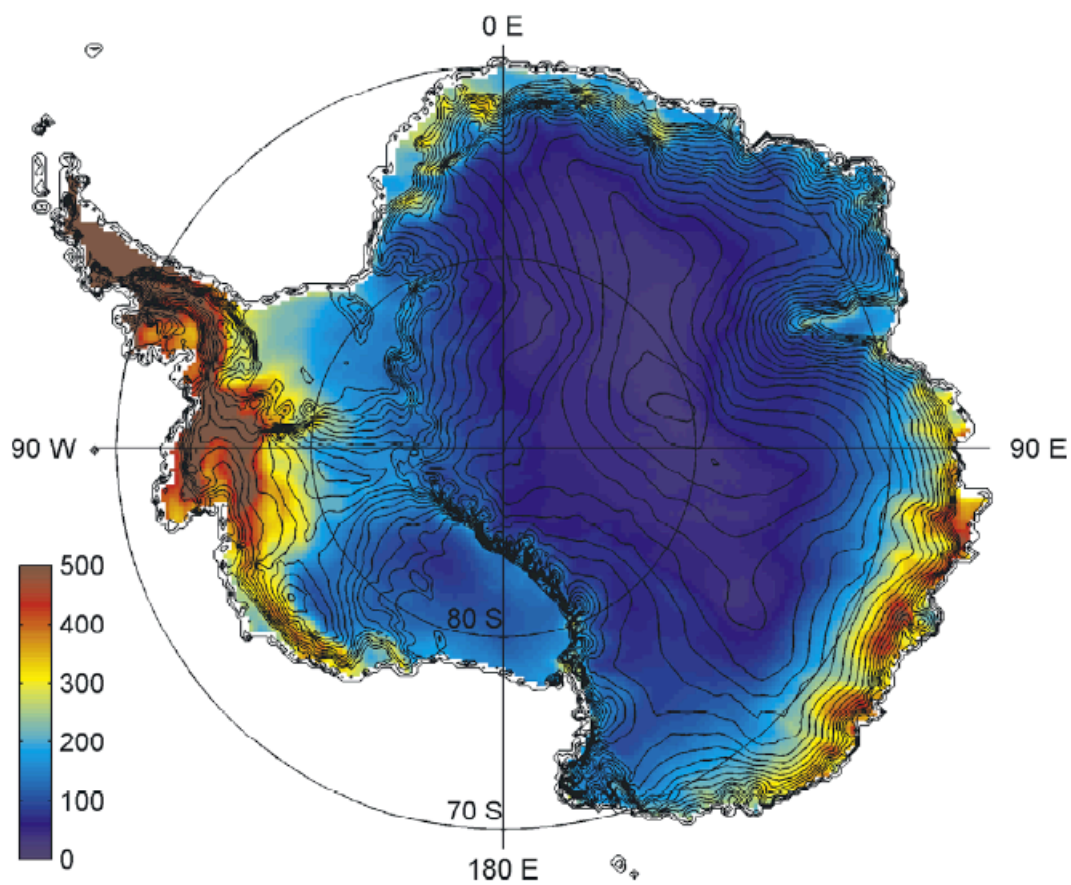
Figure 1.18: Observed accumulation over Antarctica from Arthern et al. (2006), in kg/m^2/yr.
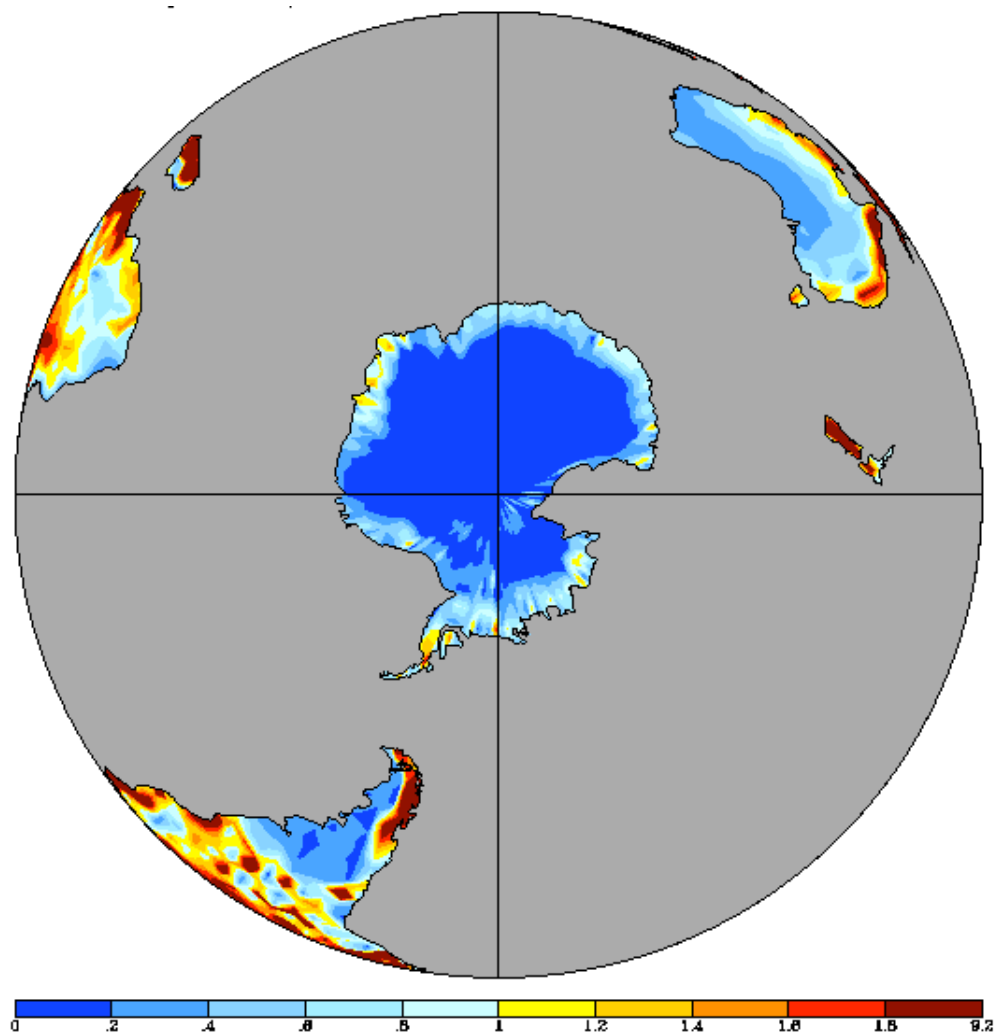
Figure 1.19: Annual mean precipitation from the high-resolution model, in m/yr.
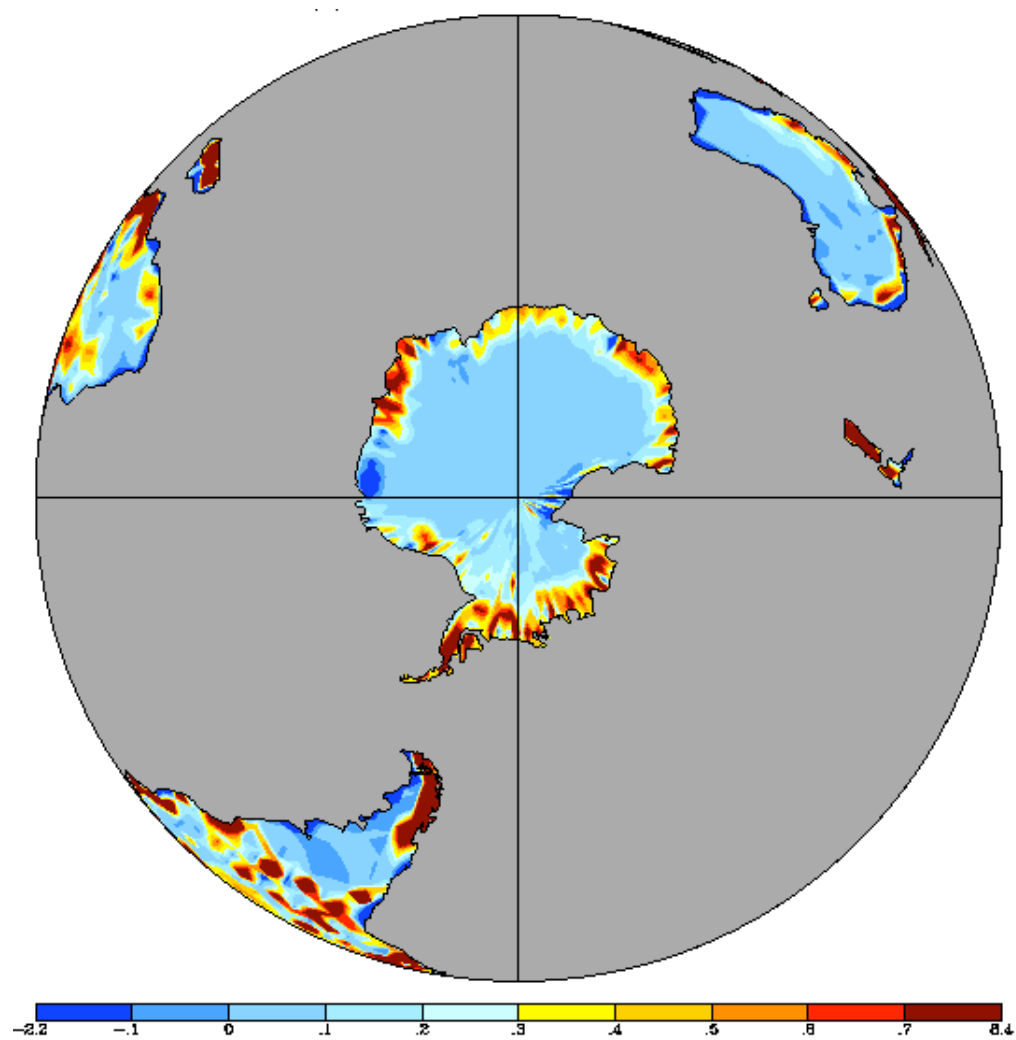
Figure 1.20: Annual mean accumulation from the high-resolution model, in m/yr.

From the observations available at Vostok, it was possible to calculate specific humidity continuously before computing the monthly mean values. Here also, the overly warm model temperatures result in a simulated specific humidity that exceeds observations throughout the year.

On Antarctica, the mechanism for coastal precipitation is similar to that for Greenland: low pressure systems propel moist air from the Southern Ocean toward the coast, where the elevation rises steeply; some air follows the contour lines along the coast, and the rest, flowing inland, is forced upward, cools and releases its moisture. In contrast, precipitation over the Antarctic plateau usually falls from clear skies, either from water vapor advected into the region, or from vapor that sublimates from the surface during the daytime in summer and precipitates at night. Cirrus clouds are also responsible for some high-altitude snow, but the cumulative effect of these processes is total snowfall that is usually less than the measuring instrument's minimum resolution. Winds frequently redistribute new and previously deposited snow, making accurate accumulation measurements even more difficult to achieve. That being said, figures 1.16 and 1.17 compare simulated Antarctic precipitation and accumulation with observations from Arthern et al. (2006) (figure 1.18). There is good first-order agreement between simulated and observed values, and simulated precipitation and accumulation also closely resemble each other, as one would expect due to Antarctica's low levels of evaporation and sublimation. Despite the model's warm temperature bias at South Pole, however, accumulation at South Pole is low, however, ranging from 0-5 cm/yr while observed values range from approximately 5-10 cm/yr (Bromwich, 1988; McConnell et al., 1997; Monaghan et al., 2006). The model's low accumulation values at South Pole lead to simulated [10]Be snow concentrations that are several times higher than observed values (see Chp. 2 and Chp. 4).

There are also several regions of negative accumulation around the coast, which are also ocean gridboxes (as was the case with Greenland). The extent of the negative accumulation areas is greatly reduced in the high-resolution model (figures 1.19 and 1.20). Overall, while

ModelE performance over Antarctica may not be as strong as over Greenland, the model is still able to qualitatively match the large-scale observed temperature and accumulation patterns. The model also does a fairly good job of simulating temperature at most locations, both in terms of magnitude and seasonal cycle. The roles that dynamic effects play with respect to inland and coastal temperatures merit investigation in future studies.

CHAPTER 2

MODELING PRODUCTION AND CLIMATE-RELATED IMPACTS ON ^{10}BE CONCENTRATION IN ICE CORES

Authors: Christy Veeder, Gavin A. Schmidt, Dorothy Koch and Colette Salyk

2.1   Abstract

The connection between the production of the cosmogenic isotope ^{10}Be and changes in heliomagnetic activity makes ice-core ^{10}Be an attractive proxy for studying changes in solar output. However, interpreting ^{10}Be ice core records on centennial timescales is complicated by potential climate-related deposition changes that could obscure the ^{10}Be production signal. By using the Goddard Institute for Space Studies (GISS) ModelE general circulation model (GCM) to selectively vary climate and production functions, we model ^{10}Be flux at key ice-coring sites. We vary geomagnetic field strength and the solar activity modulation parameter (ϕ), CO_2, sea surface temperatures and volcanic aerosols to assess impacts on ^{10}Be. Specifically we find significant latitudinal differences in the response of ^{10}Be fluxes to changes in the production function. In the climate experiments, the ^{10}Be deposition changes simulated over ice sheets in both hemispheres are comparable to those seen in the production experiments. This altered deposition combined with changes of snow accumulation results in significant climate-related ^{10}Be concentration variation in both Greenland and Antarctica. Over the Holocene, our results suggest that the ^{10}Be response to climate change should not be neglected when inferring production changes.

2.2   Introduction

To understand contemporary climate change and anthropogenic climate forcings, it is necessary to quantify solar forcing, the most significant natural forcing on centennial timescales. Sunspot observations go back to 1610, but satellite observations (which span the past 25 years (Fröhlich, 2004)) have greatly increased our understanding of solar activity as it varies over the 11-year sunspot cycle. Despite these advances, the relationship between sunspots and solar activity on multi-decadal to centennial timescales, as well as the existence of long-term solar forcing, remains largely speculative (Foukal et al., 2004).

Changes in solar irradiance (defined as the total energy output of the sun) on the 11-year timescale are positively linked with changes in solar magnetic activity (Willson and Hudson, 1988; Radick et al., 1990). In turn, the sun's magnetic field modulates galactic cosmic rays (GCR), with increased solar magnetic activity resulting in greater deflection and Earth's reduced exposure to high-energy GCR flux. Collisions between GCR and atmospheric oxygen and nitrogen result in the production of cosmogenic isotopes such as ^{10}Be (half-life of 1.5 My), ^{7}Be (half-life 53 days) and ^{14}C (half-life 5730 years) (Lal and Peters, 1967; Masarik and Beer, 1999). An anti-correlation therefore exists between ^{10}Be production and solar irradiance, since increased heliomagnetic activity implies both a brighter sun and diminished ^{10}Be production. These relationships between ^{10}Be production, magnetic activity and solar irradiance are the basis of ^{10}Be's potential use as a proxy for solar activity. However, this chain of influence depends significantly upon the link between the sun's magnetic field and irradiance changes. Various uncertainties surround these topics and are discussed in McCracken et al. (2004), McCracken (2004) and Lean et al. (2002).

The earth is also shielded from cosmic rays by its own geomagnetic field, and the combined effect of solar and geomagnetic forces leads to a production function for all cosmogenic isotopes that is stronger in high latitudes than in the tropics, and more pronounced in the stratosphere than in the troposphere (Lal and Peters, 1967; Masarik and Beer, 1999).

Solar changes impact mainly the high latitudes, while geomagnetic changes affect production closer to the equator.

Beryllium-10 (and ^{7}Be) are produced mainly in the lower stratosphere and upper troposphere; after production, ^{10}Be and ^{7}Be are rapidly scavenged by aerosols (primarily sulfates) (Lal and Peters, 1967). The average residence time in the lower stratosphere is one to two years (Davidson et al., 1981; Raisbeck et al., 1981). Eventually the aerosols descend into the lower troposphere where they are deposited at the surface by both dry (turbulent) and wet (precipitation-related) processes. This quick transition from production to deposition differentiates ^{10}Be from ^{14}C, whose response to short-term production changes is significantly damped by the carbon cycle (decreasing ^{14}C's usefulness as an indicator of multi-decadal changes in solar activity (Bard et al., 1997)), and whose records may also be affected on centennial timescales by changes in the carbon cycle. In contrast, ^{10}Be's short atmospheric residence time circumvents these complications and leads to high-resolution signals in well-dated polar ice core records (McHargue and Damon, 1991).

A complicating factor is the possibility that climatic effects may confound solar signals in the ^{10}Be record (Lal, 1987). Processes that affect the distribution of ^{10}Be in the troposphere – such as changes in stratosphere-troposphere exchange (STE) or aerosol scavenging efficiency, both of which may change with climate – could distort the degree to which ice core records reflect production changes. Similarly, because a more or less active hydrologic cycle may dilute or exaggerate ^{10}Be snow concentrations, any process that affects precipitation (ENSO events, Brönnimann et al. (2004); changes in thermohaline circulation; long-term changes in the North Atlantic Oscillation/Arctic Oscillation) could also obscure a production-rate signal. Figure 2.1 shows the climatological wet and dry ^{10}Be deposition from one of the control runs (described in the following section), demonstrating the strong link between deposition and precipitation. Midlatitude storm tracks are the dominant regions for wet deposition since the storms, which follow the latitudes associated with high ^{10}Be production, are effective in mixing ^{10}Be-rich air from the stratosphere into

the troposphere. Over ice sheets, the magnitude of dry ^{10}Be deposition is comparable to that for wet deposition. It is therefore likely that changes in hydrological and scavenging processes will be linked to changes in ^{10}Be deposition and concentration.

Annual mean wet ^{10}Be deposition (10^{-27} kg/m^2/s)

660 1320 1980 2640 3300 3960 4620 5280 5940

Annual mean dry ^{10}Be deposition (10^{-27} kg/m^2/s)

660 1320 1980 2640 3300 3960 4620 5280 5940
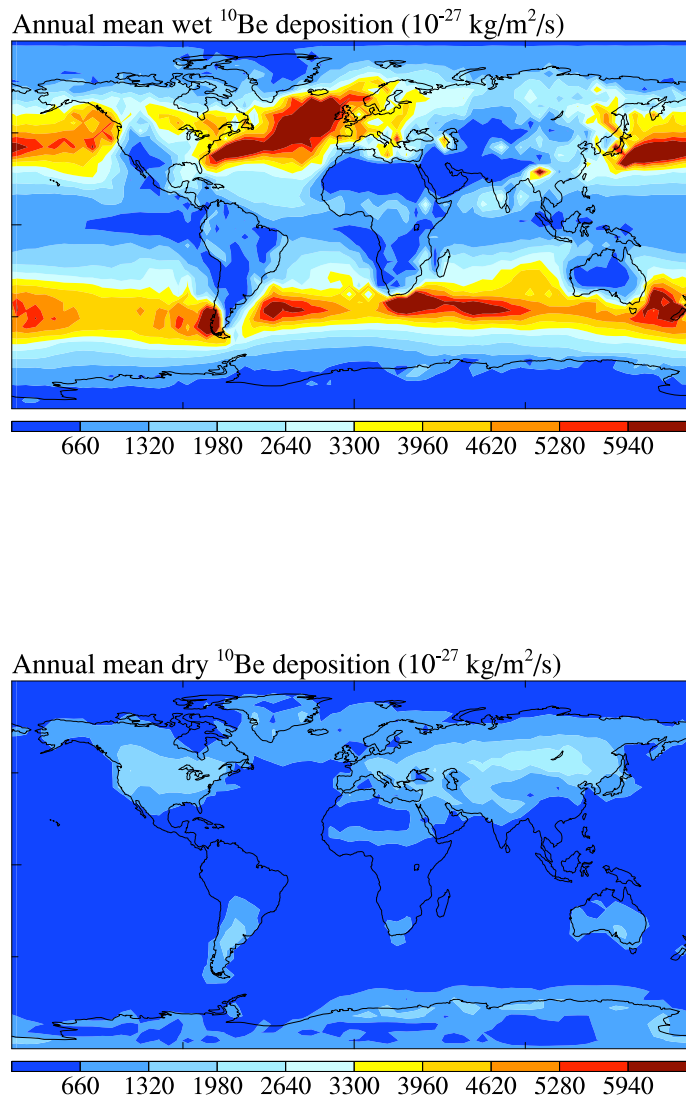
Figure 2.1: Climatological wet and dry deposition of ^{10}Be from the fixed SST control run.

Studies involving ^{10}Be have often used accumulation models (Cuffey and Clow, 1997) or oxygen isotope ratios (Dansgaard et al., 1993) to estimate ^{10}Be flux from ice core concentrations. Finkel and Nishiizumi (1997) and Muscheler et al. (2000) are two examples of such an approach. The main weakness of the concentration-to-flux method is that changes in flux may not necessarily mean that there are also changes in ^{10}Be production; also, it is not always clear whether snow concentration or flux is the most appropriate indicator for changes in atmospheric concentration (Alley et al., 1995). If ^{10}Be is to be unambiguously used to infer solar variation, we first need a way to account for the effects of climate as they appear in the ice core record; otherwise, it is possible that the coincident variation of climate signals and ^{10}Be snow concentrations may lead to a mis-attribution of the change to solar forcing. This paper will examine the ways in which production- and climate-related changes impact ^{10}Be deposition. The first experiments to be discussed focus on ^{10}Be's production function and are designed to calibrate how production changes are recorded latitudinally. We also look at simulations involving doubled CO_2 to see how ice-core records might change in a warmer climate. Next we examine how ^{10}Be flux responds during periods of reduced North Atlantic Deep Water (NADW) production using two experiments forced with ocean circulation changes. Finally, we look at potential impacts from persistent volcanic eruptions.

2.3   GISS ModelE Description

We have used the latest version of the GISS ModelE GCM (Schmidt et al., 2006). This version of the model has 20 layers in the vertical and a model top at 0.1 mb. Models with boundaries lower than this have been shown to seriously misrepresent stratosphere-troposphere exchange (STE) and poorly simulate variability in the lower stratosphere (Rind et al., 1999), which may be important in this application. Horizontal resolution is 4° x 5° (latitude x longitude). Tracers are advected, mixed and convected by all processes consistent with the model mass fluxes.

We assume that once produced, beryllium isotopes immediately attach to sulfate aerosols and are 100% soluble. This implies that there are always sufficient sulfate aerosols available to scavenge the ^{10}Be. Aerosol gravitational settling is included, as is a term that allows fine aerosols to settle faster in the stratosphere where the mean free path exceeds the particle radius (Koch and Rind, 1998). In stratiform and convective clouds, aerosol species are transported, dissolved, evaporated and scavenged (with water cloud autoconversion and by raindrop impaction beneath clouds) according to processes for each cloud type. Dissolution of beryllium isotopes is permitted only in proportion to cloud growth, and beryllium evaporation (i.e. the return of beryllium to the cloud-free portion of the gridbox) occurs in proportion to cloud evaporation.

Near the surface, tracers are handled using the same turbulent exchange coefficients as the model humidity. Turbulent dry deposition and interactive surface sources define the surface boundary conditions. The dry deposition scheme is based on the previously used resistance-in-series scheme (Koch et al., 1999) derived from the Harvard GISS chemical transport model (e.g. Chin et al. (1996)); however it is increasingly coupled to the GCM proceses, making use of the GCM-assumed leaf area indices, surface types, radiation, boundary layer height, Monin-Obhukov length, etc. A more detailed discussion of the aerosol physics in ModelE can be found in Koch et al. (2006).

The different experiments are summarized in table 2.1. For all simulations, a five-year spin-up period was used to ensure that the atmospheric distribution of cosmogenic isotopes had reached equilibrium. When we compared the fifth and tenth years of the control run, the remaining drift in the stratospheric concentration of ^{10}Be was less than 1% per year. The results for the 8.2 kyr event were averaged over ten years (instead of five in the "Younger Dryas" scenario) due to the weak nature of the forcing. For the volcanic experiment, an eruption of aerosols similar to those of the June 1991 Pinatubo eruption was set to take place once per decade. To ensure a robust model response, this simulation was run for 100 years (i.e. ten eruption cycles).

Table 2.1: Model experiments (M = present-day geomagnetic field strength)

Run	Ocean Temp.	Atmosphere	Comments
control 1	fixed SST	preindustrial GHG	$\phi = 700$ MeV, M = 1
solar min.	fixed SST	-	$\phi = 500$ MeV, M = 1
geo. min.	fixed SST	-	$\phi = 700$ MeV, M = 0.75
"Younger Dryas"	fixed SST (no NADW)	-	
8.2 kyr event	fixed SST (60% NADW)	-	
control 2	mixed layer	-	
2xCO$_2$	mixed layer	560 ppm CO$_2$	
volcanic	mixed layer	1991-2001 volcanic aerosols	
		repeating eruptions	

To simulate the production of ^{10}Be and ^{7}Be, we used the calculated production functions from Masarik and Beer (1999) and assumed a control solar modulation parameter of $\phi = 700$ MeV. This value is roughly the midpoint between recent solar minimum (400-500 MeV) and maximum (900-1100 MeV) values (Masarik and Beer, 1999). The production function also assumes present-day geomagnetic field strength (M=1). These parameters result in a mean production rate of about 0.0184 atoms/cm^2 s^1. Other ^{10}Be production-rate estimates (Lal and Peters, 1967; Oeschger et al., 1969; O'Brien et al., 1963; Masarik and Reedy, 1995) exceed that of Masarik and Beer (1999) by a factor of two or more, which attests to the difficulty of characterizing cosmogenic production in a quantitative manner.

One factor that may explain part of the difference between the Masarik and Beer (1999) production function and others is that the Masarik and Beer (1999) production function only accounts for ^{10}Be produced by impacts with cosmic ray protons; it does not account for ^{10}Be produced by helium nuclei and heavier nuclei. Although helium and "heavy" nuclei only make up approximately 9% of the incoming cosmic radiation responsible for the production of cosmogenic nuclides (the remaining 91% are protons), these heavier

particles are significant since (1) they quickly break up into neutrons and protons, each of which is as effective as a cosmic ray proton at forming ^{10}Be; and (2) their smaller charge/mass ratio makes them more resistant to modulation by changes in geomagnetic and solar magnetic field strength (McCracken, 2004). These conditions imply that the Masarik and Beer (1999) production function may underestimate the rate of ^{10}Be production and may slightly overestimate changes in the production rate. However, results for the climate- and production-change experiments are reported here in terms of percent change from the control runs, which should reduce the significance of potential errors in simulated ^{10}Be production.

2.4   Model Validation

We used a fixed SST control run to assess the model's performance for unperturbed conditions. As a sensitivity test, we performed a second control run using a 23-layer version with a higher model top (Schmidt et al., 2006), but as results were very similar, we focus exclusively on the 20-layer model. The structure of the production function for ^{7}Be is the same as that for ^{10}Be, but with a different amplitude; since ^{7}Be observations are more plentiful, we use both tracers to help validate the model's ability to simulate beryllium isotopes.

We compared annual mean surface-air ^{7}Be concentrations with observations from 91 locations worldwide; seasonal surface-air ^{7}Be concentrations were also compared with observations from 46 locations worldwide. The Environmental Measurements Laboratory is the primary source for the real-world data (see (Koch et al., 1996) for references). Also, ^{7}Be observations have been corrected to a mean solar year (as described in (Koch et al., 1996)) to facilitate their comparison with the control simulations.

Generally, the model succeeds in reproducing the seasonal cycle (figure 2.2), including the peaks during spring (due to maximum STE). Koch et al. (2006) find that compared
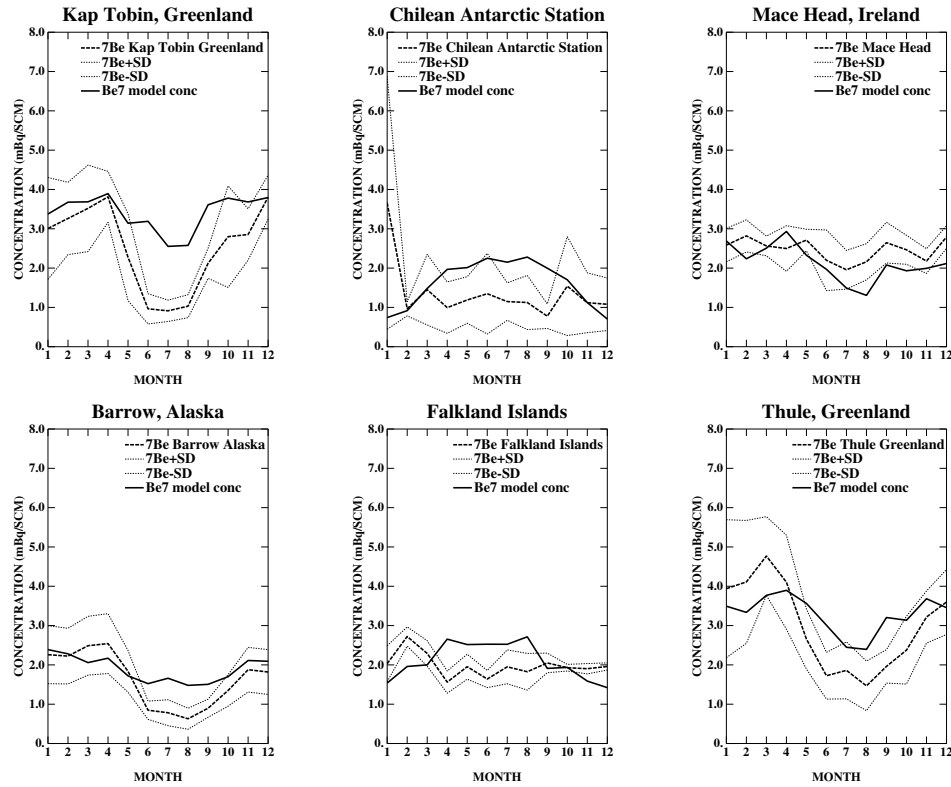
Figure 2.2: Comparison of seasonal ^{7}Be surface air concentrations with data from the control run. The six sites shown are representative of the model's overall performance. All data is from the Environmental Measurements Laboratory except for Braunschweig (from (Kolb, 1992)).

to the annual mean data, simulated ^{7}Be surface-air concentrations are sometimes too low, however model values tend to be too high at some high-latitude, northern-hemisphere locations (see Koch et al. (2006), figure 2). High-latitude discrepancies may be due to excessive STE, while the model's overall low bas may be attributed to the production function (Koch et al., 2006), which is low relative to other estimates (Lal and Peters, 1967; O'Brien et al., 1963; Masarik and Reedy, 1995). Comparison between the model and stratospheric aircraft data (see (Koch et al., 2006), figure 17) illustrates the importance of the production function more clearly: at the altitudes associated with ^{7}Be production, the model's atmospheric ^{7}Be concentrations are consistently low (by around a factor of two) relative to the observations.
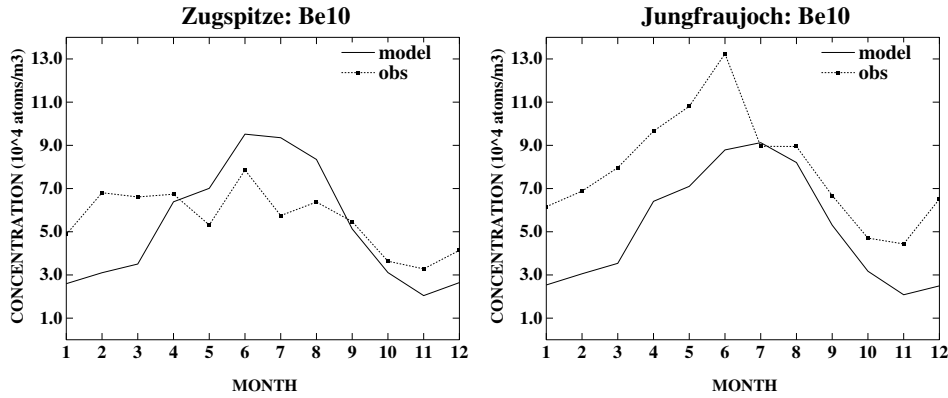
Figure 2.3: Comparison of seasonal observations of ^{10}Be surface air concentrations (Zanis et al., 2003) from Central Europe with output from the control run.

We also compare the model to sparser ^{10}Be data. Surface-air observations from the STACCATO project (Zanis et al., 2003) were taken at Jungfraujoch, Switzerland and Zugspitze, Germany (figure 2.3). The model is able to capture elements of the seasonal cycles at both locations, although the simulated ^{10}Be is sometimes too low. The data were collected during 2000 and 2001, which were years of relatively high solar activity (ϕ = approx. 860-900 MeV, but 750-900 MeV if the previous years are taken into account due to the effect of the stratospheric residence time) and low ^{10}Be production. The solar modulation was set at 700 MeV in the control run, therefore one would expect simulated ^{10}Be concentrations to be somewhat higher than the observed values. The fact that the opposite is the case suggests once again that the production function is not strong enough.

Surface-air ^{10}Be concentrations at South Pole based on six months of data (July-December 1992, Susan Harder, personal communication) show values of 3.6×10^4 atoms/m^3, which is smaller than the model's value of 5.2×10^4 atoms/m^3. Sunspot counts for 1990-1992 indicate that the solar modulation varied between approximately 750 and 1100 MeV, which may partly explain why the model's values are higher than the observations. Another contributing factor may be the convergence of the meridians at the South Pole, which is likely to make results for that gridbox less representative of Antarctic conditions than data from other Antarctic gridboxes.

Model results were also compared with aircraft data collected during 1992 and 1993 for a range of altitudes in the troposphere and stratosphere (Jordan et al., 2003). The aircraft data are instantaneous samplings, and therefore relationships between data from different latitudes will have a strong component of variability. Since most samples were taken between 30° N and 70° N, we highlight zonal mean data from this region in figure 2.4. The observed values between 40° N and 50° N, though noisy, tend to be somewhat lower than those between 30° N and 40° N; it is not clear why this is the case since ^{10}Be production increases going northward, though it may be a function of local meteorological conditions. From 1992 to 1993, the solar modulation dropped from approximately 750 MeV to 500 MeV. This rapid change, considered along with the high ϕ values in 1990 and 1991, make comparison with the model results more difficult. The agreement between the observations and the model data is also limited by the fact that the observations were taken at a wide range of longitudes while the simulated ^{10}Be values are zonal averages; there is a degree of longitudinal variability associated with planetary wave patterns. That being said, the observed values agree fairly well with the simulated ^{10}Be profiles.
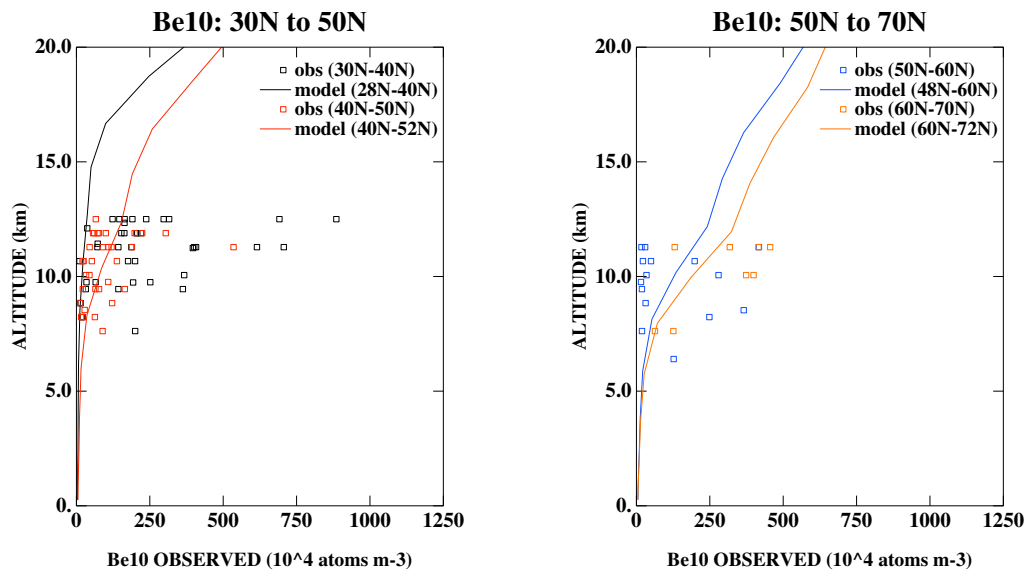
Figure 2.4: Comparison of mid-to-high latitude aircraft [10]Be observations (Jordan et al., 2003) with the control run.

The model's simulation of ^{10}Be snow concentrations at key coring sites is summarized in table 2.2. The observed values listed are the approximate values from the top of each core. Because the model has difficulty simulating sufficient accumulation over Summit, control-run ^{10}Be snow concentrations are higher than observed ($6\mathrm{x}10^4$ atoms/g in the control run vs. an observed value of approximately $1\mathrm{x}10^4$ atoms/g (Yiou et al., 1997)). Averaging the control-run values of the gridbox containing Summit with the two adjacent gridboxes to the east and south barely improves the match ($5.2\mathrm{x}10^4$ atoms/g) despite having a much better snow accumulation. While modeled snow concentrations match observations well at Dye 3, Vostok and Taylor Dome, modeled concentrations are significantly too high at South Pole (consistent with the surface air concentrations mentioned above). The high ^{10}Be snow concentration values at Summit and South Pole are consistent with the model's low snow accumulation at these sites, described in Sections 1.2.2 and 1.2.3. Another factor that may contribute to the differences between the modeled and observed ^{10}Be snow concentrations is the large uncertainty associated with aerosol scavenging by frozen precipitation. It also is possible that ModelE's tracer transport may contribute somewhat to the discrepancies, however we note that low-altitude poleward transport in the GISS model is more efficient than in other models (Textor et al., 2005); this appears to improve aerosol distributions at high latitudes (Koch et al., 2006) compared with many previous models (Rasch et al., 2000). In addition, it is important to acknowledge that the high spatial variability that characterizes Greenland's topography and climate reduces the likelihood that modeled ^{10}Be snow concentrations for a given model gridbox will strongly reflect the contents of a particular ice core (Mosley-Thompson et al., 2001); to a lesser degree, this caveat also applies to the results for Antarctica. The modeled changes in ^{10}Be are therefore less significant at the gridbox level and more likely to be useful when considered on a regional scale. Furthermore, looking at the percent change in snow concentration between the control and perturbed runs is a more robust method of assessing the model's performance and is the main way in which results will be described here.

Run	Summit	Summit ave.	Dye 3	South Pole	Vostok	Taylor Dome
observed	~1-2	-	0.5-1	3-4	~9	~2
control (fixed SST)	6	5.2	1	8.7	12.2	2.9
% change from control						
solar min.	12.2	12.2	12.2	12.4	12.4	12.4
geo. min.	8.3	8.2	8.2	8.1	8.2	8.1
2xCO$_2$	-39±6	-33±9	-12±24	-25±41	-23±11	-44±5
Younger Dryas	68±21	45±16	333±151	6±19	6±13	-10±18
8.2 kyr event	23±98	31±12	35±113	0±80	1±81	-14±70
peak volcanic	-3±11	-6±3	3±33	19±14	8±12	7±18

Table 2.2: Beryllium-10 snow concentrations at ice-core locations. Error bars are for one standard deviation (units for observations and control run: 10^4 atoms/g). Values for solar and geo. min. runs do not have "weather"-related uncertainties because only the tracers were changed in these simulations. Data: Yiou et al. (1997) (Summit), Beer et al. (1998) (Dye 3), Raisbeck and Yiou (2004) (South Pole), Raisbeck et al. (1987) (Vostok), Steig et al. (1998) and Steig et al. (2000) (Taylor Dome). Observed concentration values listed here are based on the topmost data from each core.

ModelE's ability to realistically simulate a wider, more general range of climate parameters for present-day (1979) conditions is discussed at length in (Schmidt et al., 2006). This same paper also describes the model's 20-layer version as having the highest skill relative to two other ModelE configurations (the 23-layer configuration and a 20-layer version with doubled horizontal resolution).

2.5   Experiments

2.5.1   Solar and Geomagnetic experiments

Various studies (Bard et al., 1997; Steig et al., 1996; Mazaud et al., 1994; McCracken et al., 2004; McCracken, 2004) have used statistical and mathematical techniques to estimate the degree to which solar and geomagnetic changes are enhanced or suppressed in high-latitude [10]Be records while some studies have assumed that there is no latitudinal variation in fluxes (Muscheler et al., 2004). In order to assess this, we performed one simulation with reduced geomagnetic field strength (75% of its present-day value) and one simulation with the solar modulation reduced to its approximate value during recent solar minima (ϕ=500 MeV). Both changes affect global production similarly, about a 10% increase. Geomagnetic changes of this magnitude are expected to take place on millennial timescales, while the simulated solar changes are around a third of the full maximum to minimum range. These simulations are intended to show how production changes might impact [10]Be deposition latitudinally, and can be extrapolated for other equilibrium changes.

Figure 2.5 shows percent change in total [10]Be deposition as a function of latitude. The increase in [10]Be deposition is not distributed evenly from equator to pole due to the latitudinal difference in production combined with significant mixing across latitudes. Polar deposition in both hemispheres is enhanced by approximately a factor of 1.2 (percent change in polar deposition/percent change in global average deposition) in the solar minimum run

and reduced by a factor of 0.8 in the geomagnetic minimum run. These zonal average results are reflected in the model's performance at key coring sites (table 2.2).

Percent Change in ^{10}Be Deposition
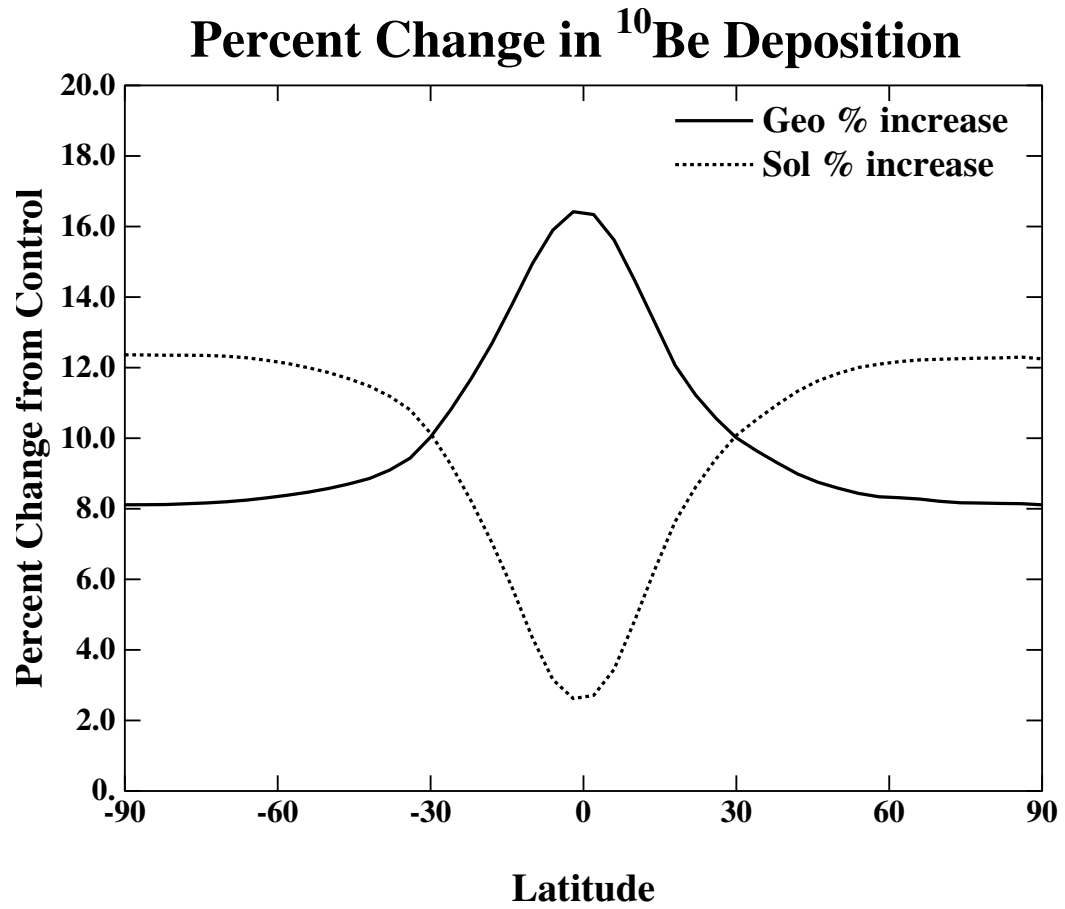
Figure 2.5: Percent change in total ^{10}Be deposition as a function of latitude. The green line shows change in deposition due to reduced solar modulation ($\phi = 500$ MeV) compared to $\phi = 700$ MeV in the control. The pink line corresponds to deposition change resulting from a 25% decrease in geomagnetic field strength. In both cases there is a $\sim$10% global mean increase in production (and deposition).

Our solar value is smaller than the enhancement discussed in (Bard et al., 1997) (approximately 1.25-2.0, when the ratio is taken as described above), however a correction of their procedure to account for the larger solar modulation for ^{14}C compared to ^{10}Be (Masarik and Beer, 1999) implies a slightly smaller range of 1.0-1.6. Our geomagnetic value is very close to the reduction of 0.75 based on observations from Vostok (Mazaud et al., 1994). Together these results suggest that the expression of geomagnetic impacts on ^{10}Be is muted (relative to the global mean) over both polar ice-sheet regions, while the effects of solar changes are augmented. Atmospheric mixing of ^{10}Be from lower latitudes to higher latitudes is clearly implicated as in previous results (Koch and Rind, 1998), since changes in high-latitude deposition occur despite the fact that the decrease in geomagnetic field strength does not affect ^{10}Be production poleward of approximately $60°$ latitude (Masarik and Beer, 1999). However, the mixing is not strong enough to remove all latitudinal variation.

2.5.2 Climate change experiments

In the following sections, we look at how climate affects STE and atmospheric ^{10}Be concentrations in the model. We also examine the response of snow accumulation, ^{10}Be deposition and ^{10}Be snow concentration (total dry and wet deposition divided by accumulation) over the Greenland and Antarctic ice sheets. In all of the climate change runs, cosmogenic production functions were kept constant consistent with present-day geomagnetic field strength and mean solar modulation for recent levels of solar activity.

2.5.3 2xCO$_2$ experiments

In order to assess the possible climate and transport effects that have influenced ^{10}Be flux during warm periods in the past, we conduct a standard 2xCO$_2$ equilibrium simula-

tion. This allows for a very clear signal-to-noise ratio in the results, and may be compared directly to another similar experiment (Land and Feichter, 2003).

For this simulation, we ran the model with a mixed-layer ocean (again, keeping ^{10}Be production constant) and compared the results with the mixed-layer control run. The atmospheric CO_2 concentration in this run is 560 ppm compared to the control value of 280 ppm, giving a global radiative forcing of around 4 W/m^2 and a global mean temperature increase of 2.7° C. In the model, there is greater warming over land masses and over northern North America; also, precipitation increases over the intertropical convergence zone as well as over mid- to high northern latitudes and Antarctica. These changes agree qualitatively with those reported in numerous other similar experiments (Cubasch et al., 2001).

(Land and Feichter, 2003) found that, in a warmer climate, the transformed Eulerian mean meridional circulation increases in the stratosphere, while stratospheric ^{10}Be concentrations decrease. In our simulation, streamfunction values increase between 7% and 35% throughout the stratosphere, implying an intensification of the Brewer-Dobson circulation. Beryllium-7's relatively short half life (compared to ^{10}Be) can be used to evaluate changes in different loss processes in the warmer climate. Loss of ^{7}Be by decay decreases from 71.1% in the control run to 69.3% in the 2xCO$_2$ run, implying that less ^{7}Be is undergoing radioactive decay in the stratosphere and more ^{7}Be is being transported to the troposphere, where it is deposited at the surface. We also find that concentrations of ^{10}Be (figure 2.6) and ^{7}Be (not shown) in the lower stratosphere decrease up to 49% and 33% respectively relative to the control run. These reduced atmospheric concentrations, as well as the the changes in streamfunction and loss by radioactive decay, are all consistent with an increase in the rate of transfer of beryllium isotopes from the stratosphere to the troposphere, similar to the results seen in the previous study.
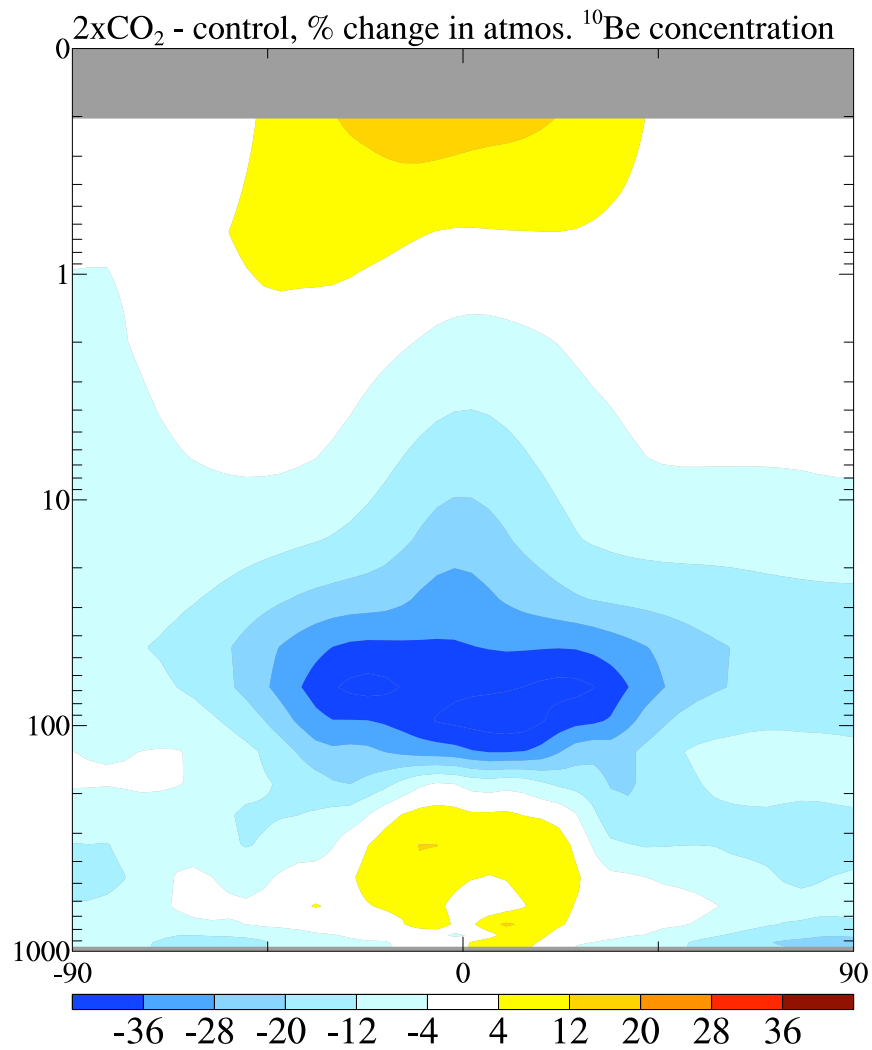
Figure 2.6: Percent change in atmospheric [10]Be concentration for the $2xCO_2$ simulation relative to the control run (latitude on x-axis, pressure in mb on y-axis).

$2xCO_2$ - control, % difference in ^{10}Be concentration
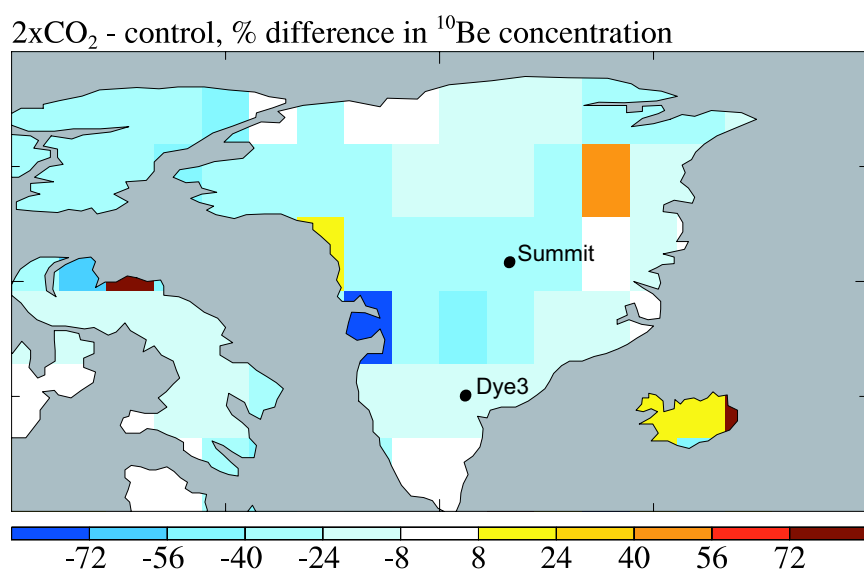
Figure 2.7: Percent change in ^{10}Be snow concentration for the $2xCO_2$ simulation relative to the control run.

$2\text{x}CO_2$ - control, % difference in ^{10}Be concentration
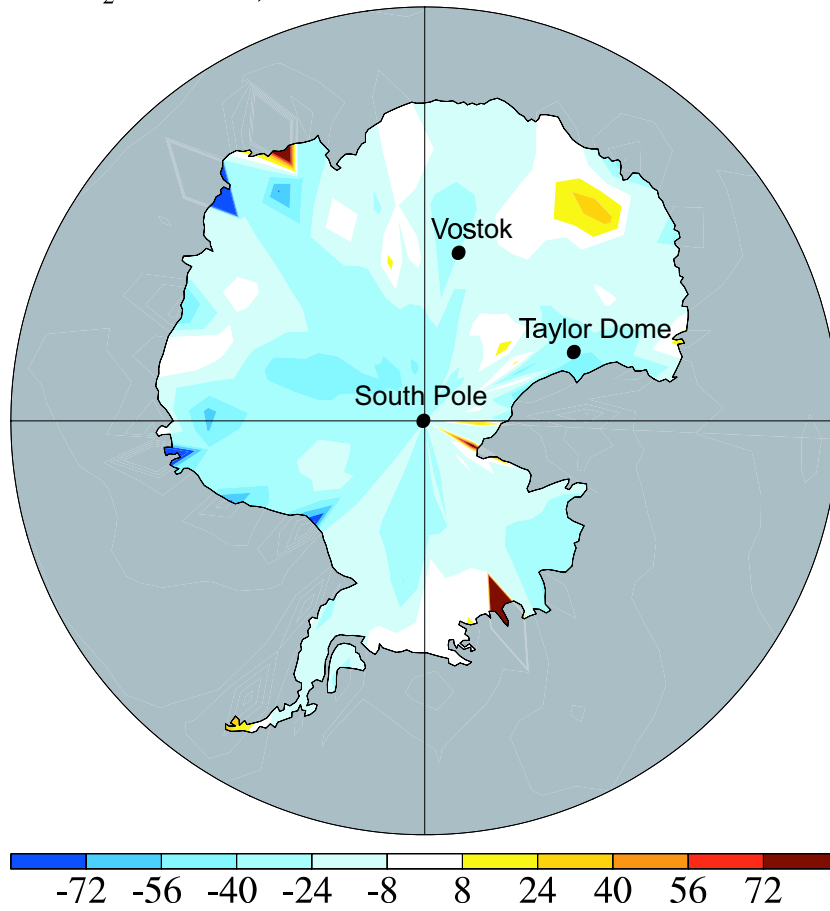
Figure 2.8: Percent change in ^{10}Be snow concentration for the $2\text{x}CO_2$ simulation relative to the control run.

The reduced tropospheric ^{10}Be concentrations seen in figure 2.6 appear to be due to increased hydrological activity at high latitudes and resulting rainout. Changes in precipitation dominate over deposition changes, which comprise small increases and decreases in total ^{10}Be deposition over Greenland's east and west coasts, respectively. Deposition changes of similar magnitude take place over Antarctica. For both ice sheets, accumulation increases by 10-50%, and ^{10}Be snow concentration drops accordingly by 8-40% (figures 2.7 and 2.8). Beryllium-10 records during warm climates therefore seem likely to be characterized by a "dilution" effect, with only slight modifications due to changes in deposition.

2.5.4 North Atlantic Ocean Circulation Changes

As a counterpoint to the 2xCO$_2$ simulation, we look at how the ^{10}Be record might change in response to a cooler climate forced by NADW changes. The Younger Dryas (YD) cold event is thought to have been accompanied by an abrupt reduction in NADW production (Broecker and Denton, 1990; Rind et al., 2001) and is apparent in the GISP2 ice core from approximately 13 to 11.7 kya. In this core, the YD interval is characterized by a halving of accumulation rate, as well as rapid oxygen isotope and dust concentration changes (Alley et al., 1993). Beryllium-10 snow concentrations roughly double during this time (Finkel and Nishiizumi, 1997), in accordance with the reduced accumulation. The "8.2 kyr event", a period of cooler Northern Hemisphere climate and hypothesized reduced NADW, is thought to have been caused by the final meltwater pulse from proglacial lakes (Barber et al., 1999). This event is characterized by approximately a 20% decrease in snow accumulation in the GISP2 record (Alley et al., 1997) and a ^{10}Be snow concentration increase of 38% in the GRIP record. This change was calculated by comparing the average ^{10}Be snow concentration from 8.15-8.11 kya (spanning the peak cooling period) with the average concentration from 8.21-8.16 kya (Yiou et al., 1997). New higher resolution data (Muscheler et al., 2004) may give a somewhat different result, and so our value should be seen as indicative, rather than definitive.

We simulate the YD and 8.2 kyr event using SST and sea-ice parameters fully derived from coupled ocean-atmosphere model simulations of these events. The SST changes for the YD scenario were based on a simulation of complete NADW shutdown (Rind et al., 2001), resulting in cooler SSTs poleward of 40° N with maximum cooling of 7-9° C off the southeast coast of Greenland. Northern hemisphere sea ice increases from 7-11% with the greatest increases between 45° N and 75° N. Small sea ice increases (0.6%) also occur around Antarctica. For the 8.2 kyr event, the SST changes were based on the impact of a small meltwater pulse from Lake Agassiz (LeGrande et al., 2006), resulting in a 40% reduction in NADW. The cooling is confined to the north Atlantic with maximum cooling of 1.5-3.5° C to the south of Greenland. In the northern hemisphere, sea ice increases by 2% with the greatest gains in the same latitudes as for the YD; sea ice changes around Antarctica are negligible.

During the YD and the 8.2 kyr events, other climatic changes may have occurred that may or may not have been connected to changes in NADW production, however the changes in climate and [10]Be described in this section are based on model runs that are forced only with direct impacts of NADW production changes. Furthermore, the reduced NADW used in our experiments was imposed on a preindustrial climate, which may be substantially different from the actual climates that preceded the YD and the 8.2 kyr event. These factors could therefore impact the applicability of our results, which should only be regarded as the model's response to NADW changes that may be considered characteristic of the YD and 8.2 kyr events.

2.5.5   Greenland

The results for Greenland are shown in figures 2.9 through 2.13. Results for the 8.2 kyr run are very similar to those for the YD run and are not shown except for changes in [10]Be snow concentration. In the YD run, global mean temperature drops 1° C and

temperatures over central Greenland drop by 3-5° C. In the 8.2 kyr run, global mean and Greenland temperature decreases by 0.2° C and 0.5-1.3° C respectively (about 75% smaller than those in the YD run). Estimates of Greenland cooling associated with the 8.2 kyr event are based on a 1.5-2.0 change in $\delta^{18}O$ (Alley et al., 1997; von Grafenstein et al., 1998) and are relatively poorly constrained. The model roughly captures the ratio of the observed estimated Greenland temperature changes (approximately 3:1) between the YD (approximately 15° C cooling, (Johnsen et al., 1995; Schwander et al., 1997; Severinghaus et al., 1998)) and 8.2 kyr event (4–8° C cooling, (Barber et al., 1999)), if not the magnitude of the cooling.

The model's lack of success in simulating YD and 8.2 kyr temperatures as cold as those implied by the $\delta^{18}O$ records is reflected in the accumulation and ^{10}Be concentration changes for both scenarios. In the YD run, Greenland accumulation decreases by 12-60% while total ^{10}Be deposition increase 5-45% over the northern half of the ice sheet and decreases slightly (5-15%) on the southeast coast. The combined changes in accumulation and deposition result in snow concentration increases greater than 36% over most of eastern Greenland, with a 68% increase at Summit – roughly two-thirds of the observed change of approximately 100% described in (Finkel and Nishiizumi, 1997). Had the simulated climate over Greenland been colder, it is likely that accumulation would have been further suppressed and snow concentrations would be closer to the observed values.

Similar changes occur in the 8.2 kyr run: accumulation is reduced by 12-60% while total ^{10}Be deposition increases by 2-14% over the southern part of the ice sheet and by 2-18% over northern Greenland. These changes lead to ^{10}Be snow concentration increases of 12-60% over most of the central and eastern parts of the continent. The simulated changes in snow concentrations at Summit (23%) are about half as large as the 40% increase observed in the GRIP record.

YD - control, % change in total deposition
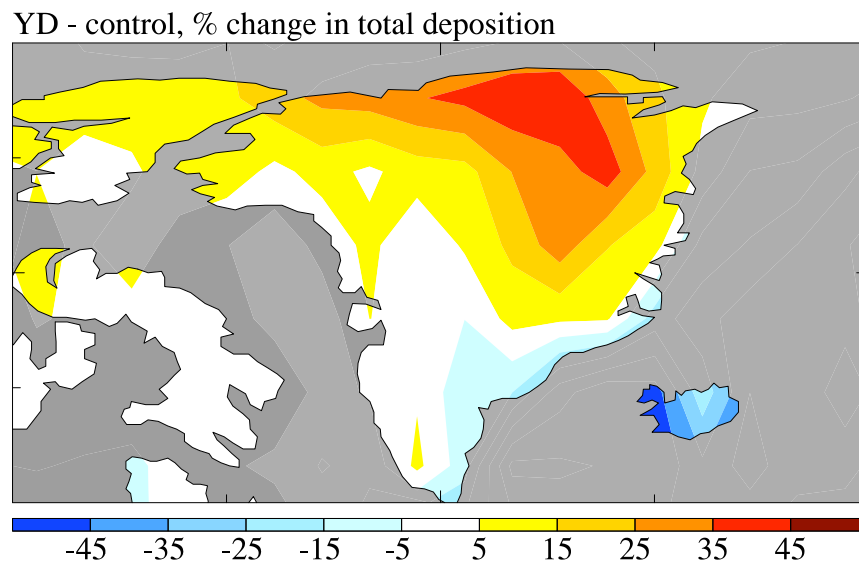
Figure 2.9: Percent change in total ^{10}Be deposition for the YD simulation relative to the control run.

YD - control, % change in accumulation
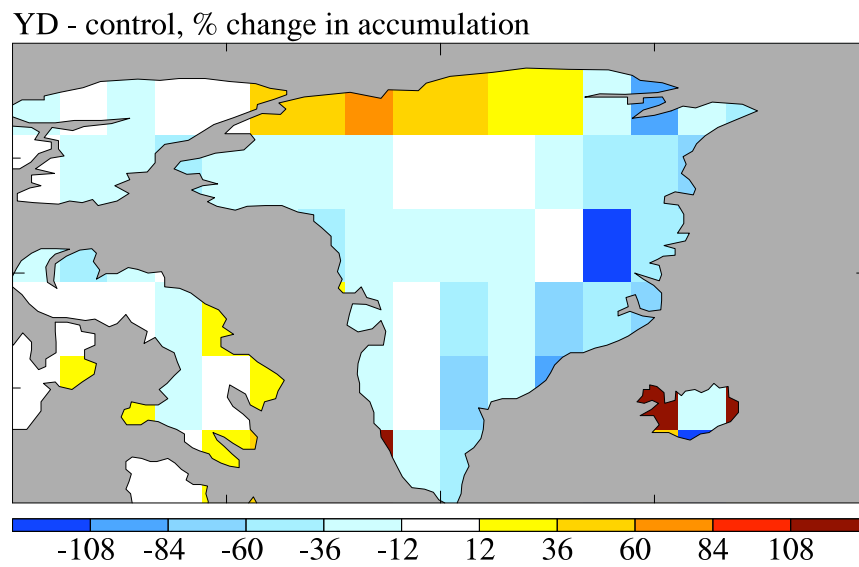
Figure 2.10: Percent change in accumulation for the YD simulation relative to the control run.

YD - control, % difference in ^{10}Be concentration

-108 -84 -60 -36 -12 12 36 60 84 108
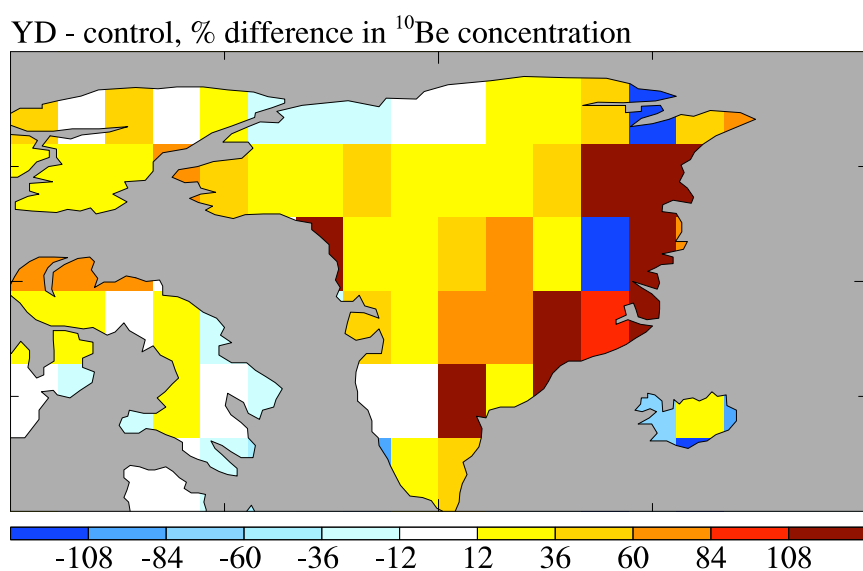
Figure 2.11: Percent change in ^{10}Be snow concentration for the YD simulation relative to the control run.

8.2 kya - control, % difference in ^{10}Be concentration

-108 -84 -60 -36 -12 12 36 60 84 108
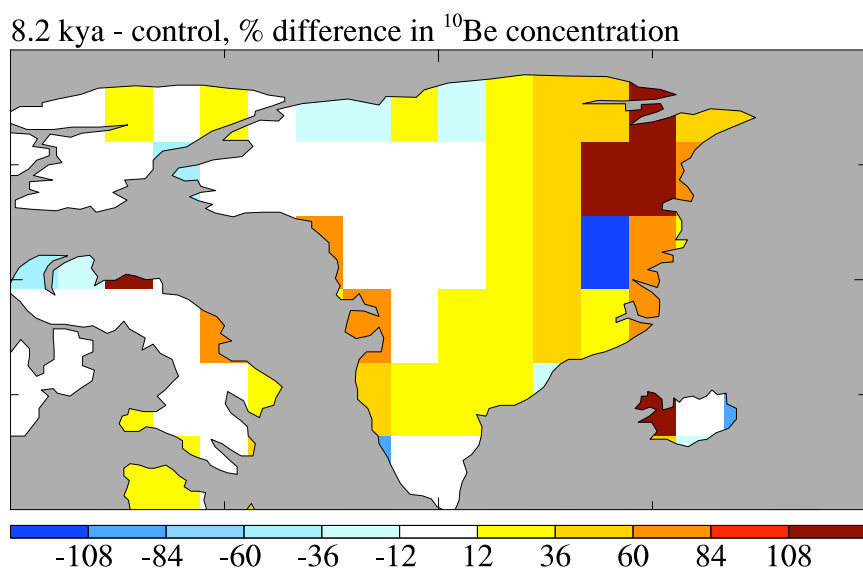
Figure 2.12: Percent change in ^{10}Be snow concentration for the 8.2 kyr simulation relative to the control run.

YD - control, % change in atmos. [10]Be concentration
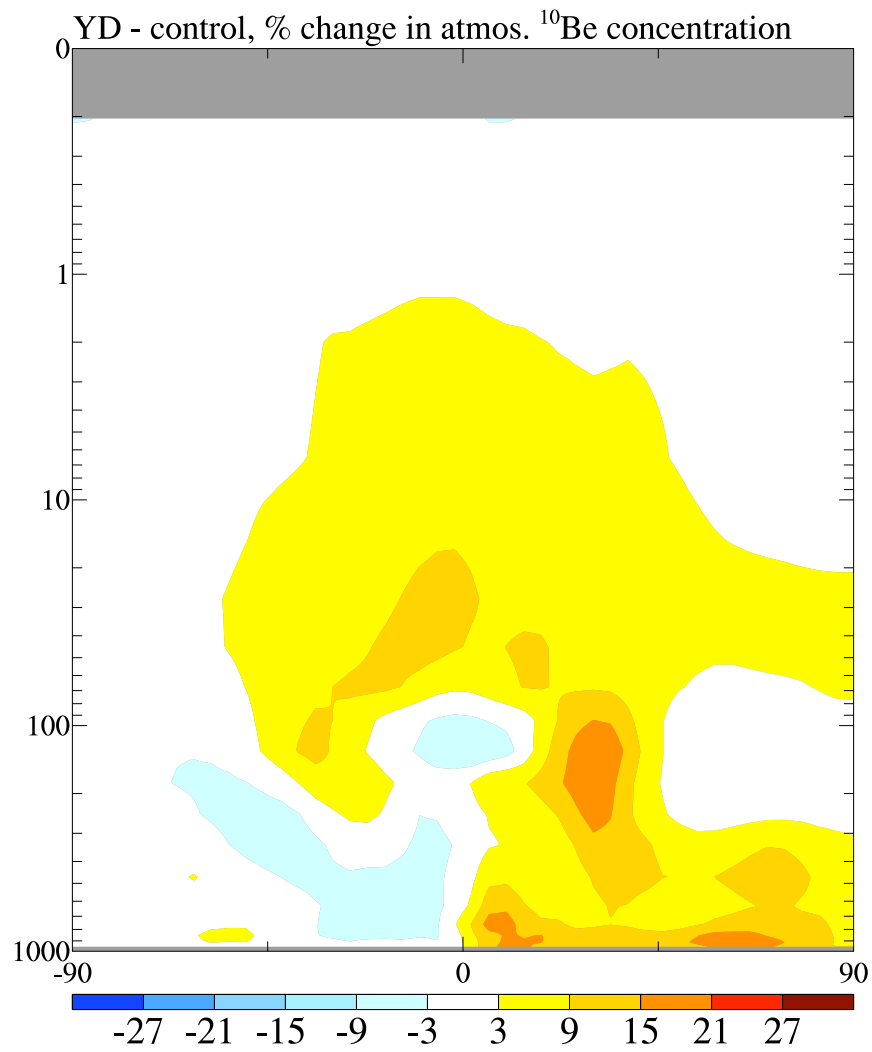
Figure 2.13: Percent change in atmospheric [10]Be concentration for the YD simulation relative to the control run (latitude on x-axis, pressure in mb on y-axis).

The apparent explanation for the increased ^{10}Be deposition in these simulations are the cold SSTs off Greenland's southeastern coast: the cold ocean cools air over the northern North Atlantic, increasing surface pressure and reducing precipitation. As a result, atmospheric ^{10}Be concentrations between $50°$ N and $90°$ N increase by 3-21% in the YD (figure 2.13) and between 3-7% in the 8.2 kyr experiment (not shown). The ^{10}Be-enriched air leads to increased concentrations in wet deposition (snow) and increased dry deposition over Greenland. This increased deposition combines with reduced snow accumulation to produce significantly higher snow concentrations.

To see if transport processes in the YD run might have been affected in a way similar to that seen in the 2xCO$_2$ scenario, we looked at changes in streamfunction, atmospheric concentrations and decay rates. Streamfunction changes are negligible throughout the stratosphere ($\pm5\%$). Beryllium-10 concentrations in the stratosphere increase 3-15% compared to the control run (figure 2.13), however the percent of ^{7}Be lost to radioactive decay increases only modestly, from 71.1% to 71.7%. Collectively, these results imply that large-scale changes in beryllium advection play a relatively unimportant role in the cold North Atlantic runs.

2.5.6 Antarctica

Changes similar to those over Greenland take place over Antarctica, though on a smaller scale; the relative magnitudes of the YD and 8.2 kyr changes are, however, similar to those over Greenland. Temperatures cool slightly in the YD run, with significant cooling over Dronning Maud Land (1.4-1.9° C). There are variable increases in ^{10}Be deposition, however accumulation generally decreases (5-35%) due to the cooler temperatures. Consequently, snow concentration increases 5-35% with small regions of higher concentration changes (45% and greater) over parts of Dronning Maud Land and near the Ross ice shelf (figure 2.14). Although ^{10}Be snow concentrations around Taylor Dome decrease in this

run, concentrations increase on a larger regional scale. This result is consistent with observations showing that YD [10]Be snow concentrations at Taylor Dome exceed preindustrial levels by approximately 100% (Steig et al., 1998), however changes seen in Antarctica may be more directly related to the Antarctic Cold Reversal. We would therefore not expect to capture these changes in a model forced solely with altered NADW production. In the 8.2 kyr run, changes in temperature are not statistically significant, and accumulation and snow concentration changes are smaller and more variable (figure 2.14).

2.5.7 Volcanic experiments

Explosive volcanic eruptions whose output reaches the stratosphere are typically followed by a period of global cooling due to shortwave absorption and longwave emission of the increased stratospheric aerosol load (Shindell et al., 2003). Since the residence time for stratospheric aerosols is generally one to two years, the duration of the aerosol-induced cooling is limited to this timescale. In order to assess whether these short period events can impact deposition, we analyze data from a hundred-year (10-eruption) simulation and compare data from the two coldest years following each eruption (20 years total) with data averaged over the entire simulation. Since we assume that [10]Be attaches immediately to sulfate, the increased amounts of stratospheric sulfate resulting from an eruption do not affect the rate of scavenging in our experiments; additionally we do not account for possible reductions in settling time due to the potentially larger size of volcanic sulfates.

In the model, the global mean temperature decreases on average by $0.23°$ C during the peak cooling period and is associated with a mean radiative forcing over that period of approximately -1.7 W/m^2. Temperatures over Greenland cool by 0.1-0.4° C and accumulation is reduced over most of Greenland, resulting in a 3-9% decrease in wet [10]Be deposition over the southern and northern parts of the ice sheet. There is basically no change in dry deposition, and snow concentration changes are negligible (within $\pm 6\%$ of the 100-year average

values). Changes in atmospheric [10]Be concentrations and in the transformed Eulerian mean streamfunction are also within $\pm 6\%$ of average levels (not shown), which implies that any potential STE changes are relatively unimportant.

66

(b) 8.2 kya - control, % difference in ^{10}Be concentration

(a) YD - control, % difference in ^{10}Be concentration
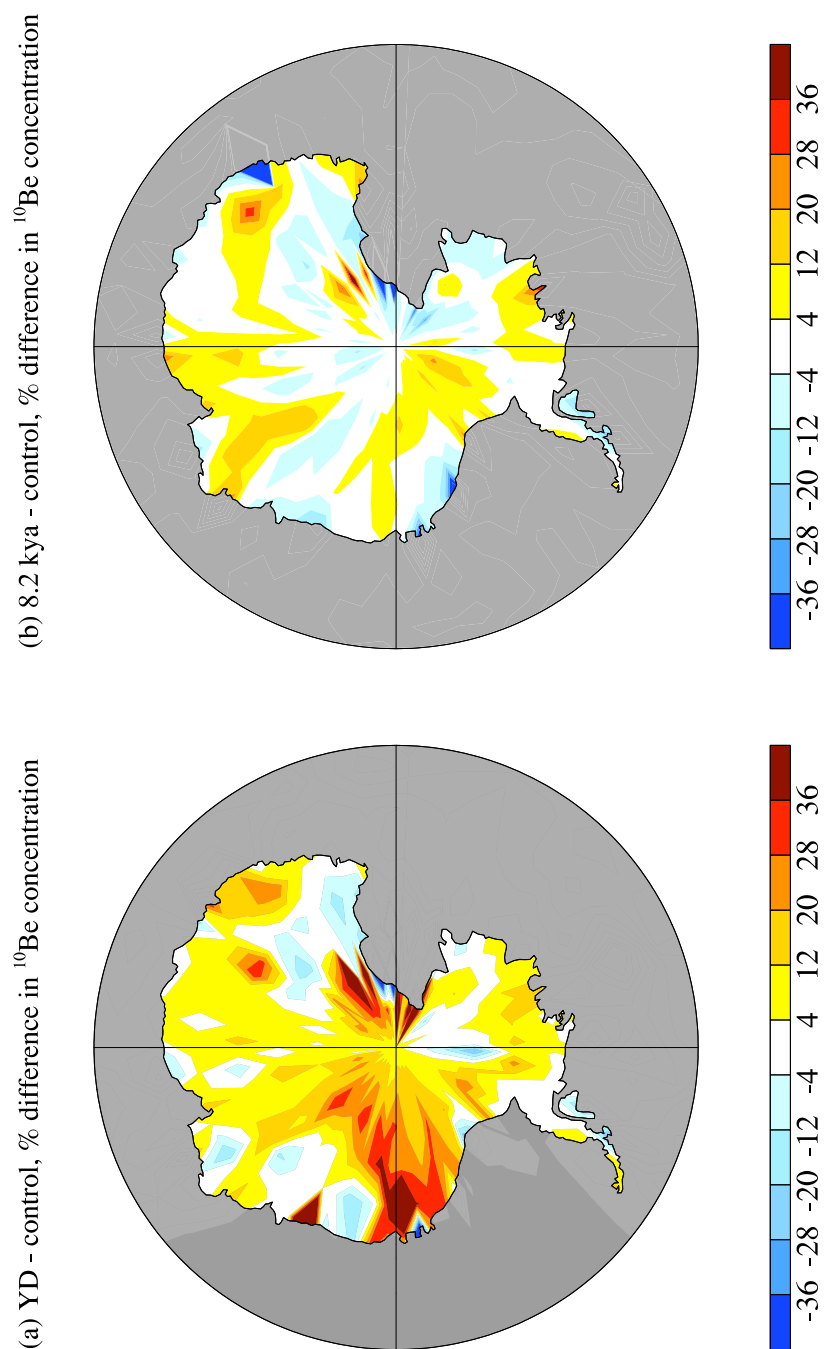
Figure 2.14: Percent change in ^{10}Be snow concentration for the (a) the YD and (b) the 8.2 kyr simulation relative to the control run.

peak volcanic - 100-year mean, % difference in ^{10}Be concentration

-45 -35 -25 -15 -5 5 15 25 35 45
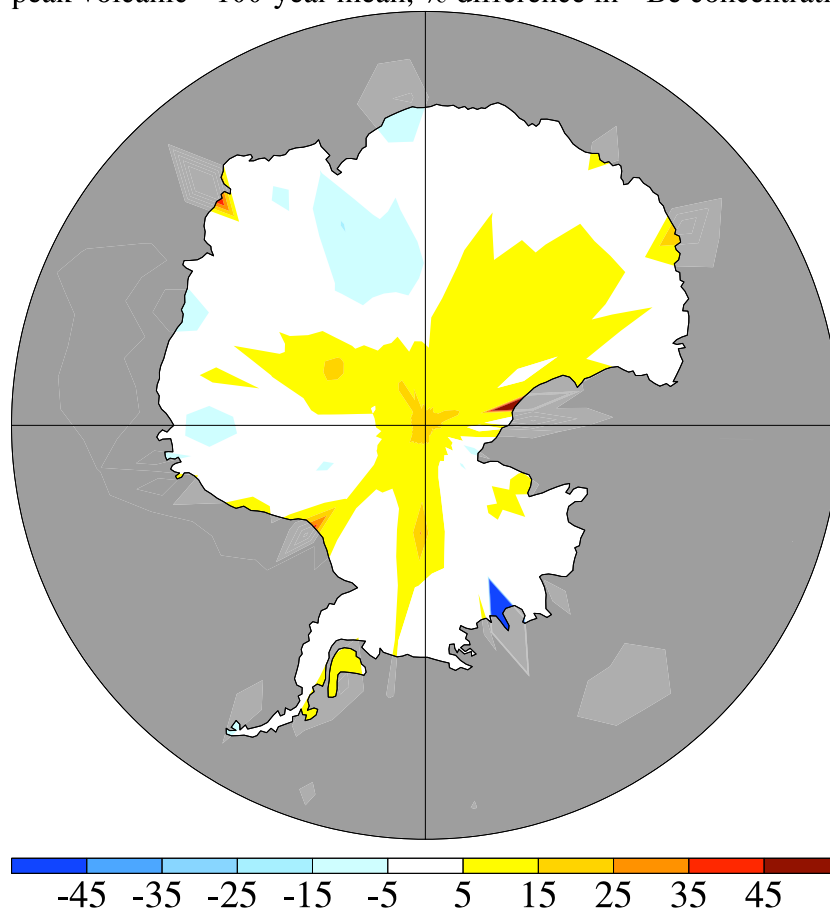
Figure 2.15: Percent change in ^{10}Be snow concentration for the peak years of the volcanic simulation relative to the 100-year mean.

Similar changes in deposition and temperature take place over Antarctica: temperatures cool 0.1-0.6° C and accumulation decreases 3-15% over most of the central and eastern parts of the ice sheet. The lowered accumulation is accompanied by reduced wet deposition (2-10% less than the 100-year mean), with negligible changes in dry deposition. However the decreased accumulation has a more dominant effect on snow concentration changes, which increase 5-15% over parts of central and eastern Antarctica (figure 2.15), with slightly greater increases at the South Pole (19%). The results collectively suggest that climate changes associated with volcanism are unlikely to impact Greenland ^{10}Be records significantly, but may have a more variable impact on Antarctic records.

2.6   Conclusions

Model simulations using beryllium isotope tracers were performed to see how changes in production function and climate may impact ^{10}Be flux over polar ice-coring areas. In the production change experiments, a lower level of solar activity enhances polar ^{10}Be deposition relative to global average deposition (or production) by a factor of 1.2; reduced geomagnetic activity lowers polar ^{10}Be deposition by a factor of 0.8. Both values are similar to those inferred in earlier studies (Bard et al., 1997; Mazaud et al., 1994). When interpreting ice core records, however, one must bear in mind the timescales typically associated with production-related changes: ^{10}Be enhancement associated with geomagnetic changes is more likely to present itself as a long-term trend extending over centuries or millennia, while solar changes such as those related with Spörer and Maunder minima appear to take place over multidecadal to centennial timescales.

In both of the reduced NADW experiments (YD and 8.2 kyr event), the model simulates ^{10}Be snow concentration increases at Summit that are roughly half those seen in the ice core record, possibly consistent with the underestimated temperature response in Greenland. The modeled increases in both snow concentrations and atmospheric concentrations are

accomplished without any change in solar modulation, implying that the observed changes may not be indicative solely of a solar-forced response (Muscheler et al., 2004). We also note the relatively linear change in ^{10}Be snow concentrations between the YD and 8.2 kyr scenarios, which suggests that while concentration changes seen during the YD are significant, they should not necessarily be considered the anomalous result of a large-scale climate shift, but rather part of a continuum that also encompasses the changes seen in the 8.2 kyr simulation.

In the runs with radiative forcings, changes in ^{10}Be snow concentrations are dominated by changes in precipitation: warming in the $2xCO_2$ run leads to a dilution of ^{10}Be over ice sheets, and cooling in the volcanic run leads to lower precipitation and higher snow concentrations. The $2xCO_2$ run is characterized by competing increases in both STE and precipitation, demonstrating that increased stratospheric transport does not necessarily translate into increased ^{10}Be snow concentration. Conversely, changes in snow concentration are not always linked to changes in STE, as shown in the YD simulation.

Snow concentration changes over Antarctica appear to be roughly scalable to the degree of radiative forcing. In the volcanic run, the forcing is approximately -1.7 W/m^2 and Antarctic ^{10}Be snow concentrations increase by 5-15%. In the $2xCO_2$ run, the radiative forcing is approximately 4 W/m^2 and snow concentrations decrease by 8-40%. These results suggest a tentative rule of thumb of approximately a 10% change in Antarctic snow concentration for every 1 W/m^2 of forcing. The more variable nature of Greenland's climate, as well as its much smaller size, is the most likely cause for its exclusion from this relationship.

Changes in radiative forcing from roughly 1850 to the present have been around 1.6$\pm$1 W/m^2 (of which approximately 0.8 W/m^2 has not yet been realized (Hansen et al., 2005)). Temperature change has been around 0.8° C, which is approximately 30% of the change seen in equilibrium $2xCO_2$ runs. Thus it is conceivable that concentration changes of $\sim$10% may have occured as a result of 20th century climate change. We stress, however, that

this remains to be demonstrated in full 20th century transient experiments. More work is required to understand responses over both ice sheets under various conditions, and to assess the strength of any potential link between snow concentration and radiative forcing in general.

Over the course of the 11-year solar cycle, ^{10}Be snow concentration changes by roughly $\pm$ 10-20% relative to the concentration during an average solar year (or a 40% decrease from min. to max.) (McCracken et al., 2004; Steig et al., 1996). This response is mostly larger than the concentration changes seen in the climate perturbation experiments. However on centennial timescales, ^{10}Be's response to longer-term solar variability may be more comparable to the synchronous climate-related concentration changes. These considerations make it more difficult to ascribe specific causes to changes in the ^{10}Be ice core record, and in particular to distinguish between climate-related and solar-related changes. Furthermore, if changes in the solar magnetic field are accompanied by changes in solar output, then a less active sun is likely to result not only in increased ^{10}Be production, but also in climate changes that may significantly enhance the (already heightened) ^{10}Be snow concentrations over ice sheet regions. Interpreting the ^{10}Be record without accounting for possible climate-related changes carries the risk of inferring the existence of solar changes that are larger than those which actually occurred.

One time period of particular interest is the Maunder Minimum (late 17th century) during which ^{10}Be snow concentrations increased by $\sim$50% at Dye 3 and $\sim$40% at the South Pole (1690–1710 CE compared to 1730–1750 CE) (Bard et al., 1997; McCracken et al., 2004). Reduced sunspot activity and increased volcanism most likely contributed to significant global cooling at this time. (McCracken et al., 2004) estimate that this period was characterized by values for ϕ as low as 84 MeV, which correspond approximately to a 40% increase in global mean ^{10}Be production relative to average present-day conditions. However, accounting for the cooler climate and the impact of solar activity (including the response of ozone to UV variability and related dynamic effects (Shindell et al., 1999)) may

imply that some fraction of the ^{10}Be change was climatic. In future work, we hope to be able to improve the calibration of ^{10}Be by examining the combined effects of climate and production-related changes both during the Maunder Minimum and over the course of the 11-year solar cycle. Comparison with observed and modeled ^{14}C data from the Maunder Minimum may also help to distinguish between production and climate-related impacts on isotope records.

The results presented here are also relevant for longer-term variability. During the last 10 ky, ^{10}Be snow concentrations at Summit and the South Pole vary from the mean values by up to approximately $\pm 45\%$ (Finkel and Nishiizumi, 1997; Yiou et al., 1997; Raisbeck et al., 1981) on centennial timescales. Given that there have been significant changes in greenhouse gases, volcanism and North Atlantic circulation changes over this period, the associated climatically forced ^{10}Be snow concentration changes could therefore be significant. Further investigation of specific time periods with more clearly defined forcings will be required to better quantify this relationship.

CHAPTER 3

INTERPRETING ^{10}BE CHANGES DURING THE MAUNDER MINIMUM

Authors: Christy Veeder, Gavin A. Schmidt, and Drew Shindell

3.1   Abstract

Beryllium-10 archives are important resources for understanding how solar activity may have varied in the past. Climate simulations using the Goddard Institute for Space Studies ModelE general circulation model are used to calibrate the impacts of production changes, solar forcings and volcanic aerosol forcing on ^{10}Be concentration during periods such as the Maunder Minimum (1645-1715 AD). We find that for the preindustrial period, production-related ^{10}Be changes are the dominant signal in snow concentration, and that the effects of both solar and volcanic forcings on climate are relatively minor. Ambiguities in determining the observed changes in ^{10}Be snow concentration during the Maunder Minimum complicate the process of estimating changes in the solar modulation strength during that time. Given those limitations, we estimate that the average value of the solar modulation parameter ϕ was between 280-395 MeV over the course of the Maunder Minimum, and was approximately 142 MeV during the years of peak ^{10}Be concentration as recorded in the Dye 3 and South Pole ice core records.

3.2   Introduction

As the study of present-day climate change continues to evolve, so does the need to develop a more comprehensive understanding of natural climate forcings, including changes in solar irradiance. The variations in solar output associated with the 11-year sunspot cycle do not seem to have a strong impact on surface climate (Camp and Tung, 2007; Gray et al., in press) however the so-called "Grand Minima" – periods of prolonged quiescence in solar activity which appear to have taken place several times during the past 1000 years – may have had a greater impact (McCracken et al., 2004). One of the more recent and pronounced of these periods, the Maunder Minimum (MM), occurred from 1645-1715 AD (Eddy, 1976; Stuiver and Quay, 1980; Ribes and Nesme-Ribes, 1993; Lean, 2000) and was characterized by very low sunspot numbers (Hoyt and Schatten, 1998), which has been assumed to imply a reduction in solar irradiance (of uncertain magnitude) (Willson and Hudson, 1988; Radick et al., 1990; Foukal et al., 2006). The reduced solar activity during the MM also coincided with a period of reduced temperatures, increased volcanic activity and glacial expansion in the northern hemisphere (Overpeck et al., 2004; Jones et al., 1998; Jones and Mann, 2004; Crowley, 2000; Crowley et al., 2008; Free and Robock, 1999), particularly during the late MM (approx. 1680-1710, however reconstructed estimates vary as to when the greatest cooling occurred).

Only satellite data provide direct observations of changes in solar irradiance, but since such observations are not available during any of the Grand Minima, we must turn to proxy indicators. Cosmogenic isotopes such as beryllium-10 (^{10}Be) are particularly useful in this regard, since their production by high-energy galactic cosmic rays (GCR) is modulated by the strength of the solar magnetic field (Lal and Peters, 1967; Masarik and Beer, 1999). (Changes in geomagnetic field strength also affect GCR flux, but generally on much longer timescales than the decadal or centennial changes associated with solar activity (Muscheler et al., 2007).) The production of cosmogenic isotopes takes place mainly in the stratosphere

and upper troposphere, and is the result of spallation reactions between cosmic ray particles and atmospheric oxygen and nitrogen (Lal and Peters, 1967; McHargue and Damon, 1991). Increases in solar magnetic activity, which are correlated with increases in solar irradiance over the 11-year sunspot cycle (Lean, 1994; Lean et al., 2002), cause Earth's atmosphere to be more strongly shielded from the GCR flux. Such shielding, typically described using the solar modulation parameter ϕ (Gleeson and Axford, 1968), results in lower levels of cosmogenic isotope production (Masarik and Beer, 1999; Stuiver and Quay, 1980; McCracken et al., 2004). This inverse relationship is consistent with the relatively high concentration of ^{10}Be stored in ice core archives during the MM (figure 3.1), when sunspot activity was persistently low (although the ^{10}Be record at Dye 3 shows evidence of an 11-year cycle during this time (Beer et al., 1990), implying that some kind of solar modulation was taking place despite the very low sunspot numbers). The high MM ^{10}Be snow concentrations also suggest that reduced solar irradiance may have contributed to the colder conditions during the MM (Eddy, 1976).

The excellent (annual to decadal) time resolution available with ice-core records makes ^{10}Be data from Greenland and Antarctica the preferred archives for estimating solar changes over the entire Holocene. There are, however, potential complications when interpreting ^{10}Be records. In ice cores, ^{10}Be is primarily measured in terms of its concentration per gram of snow water equivalent. Changes in climate (which may affect wet deposition, dry deposition, atmospheric transport and precipitation – and which may occur independently of changes in solar irradiance) and changes in ^{10}Be production therefore both play a role in determining ^{10}Be snow concentrations. For instance, if reduced snowfall and increased ^{10}Be production occur simultaneously, the ^{10}Be concentrations in the ice-core record will be higher than they would be due to changes in production alone (Field et al., 2006; LeGrande et al., 2006). Under such circumstances it could be possible to infer larger changes in solar magnetic activity and GCR shielding than actually took place.

Disentangling solar- and climate-related impacts on ^{10}Be ice-core records is particularly relevant for understanding total solar irradiance (TSI) changes during the Maunder Minimum. The coincidence of such a prolonged solar anomaly with a well-documented period of northern hemisphere cooling; the timing of these events prior to the onset of anthropogenic climate change; the recent invention of the telescope and hence the abundance of sunspot observations during the MM; and the existence of several sets of ^{10}Be data spanning the time period collectively provide a rich set of resources for interpreting not only how irradiance changes impact Earth's climate, but also how climate changes and production changes are expressed in ^{10}Be ice core records.

General circulation models have the capability to play a key role in answering these questions since they provide the opportunity to vary climate and ^{10}Be production independently. During the MM, the relevant climate forcings are from the cooling effects of stratospheric aerosols due to increased levels of volcanic activity, and from direct and indirect changes associated with reduced TSI. In addition to the direct TSI change, capturing the variability in the UV bands is also important. Satellite observations have shown that changes in solar UV radiation are significantly larger in percentage terms than changes in the visible spectrum (Lean, 1994; Lean et al., 1995). They affect the distribution of stratospheric ozone over the course of the sunspot cycle and can significantly change the vertical temperature profile, particularly at low latitudes (Haigh, 1996; Shindell et al., 2006). The temperature changes may in turn affect the propagation of planetary wave energy and can impact surface temperature and storminess at high latitudes (Shindell et al., 1999, 2001; Rind et al., 2007). The effect of these changes on storm track patterns is another mechanism by which solar-induced climate change might affect the ^{10}Be record.

In this paper, we vary TSI, ozone, spectral irradiance, stratospheric volcanic aerosols and ^{10}Be production rates to present a suite of climate simulations spanning a range of possible MM scenarios. We then examine how the modeled changes in climate and production affect ^{10}Be at different ice-core locations, and how our results compare with the

observational record.

3.3 GISS ModelE Description

Our experiments were performed using the latest version of the Goddard Institute for Space Studies (GISS) ModelE general circulation model (GCM) (Schmidt et al., 2006). This version of the model has a horizontal resolution of 4° x 5° (latitude x longitude) and a vertical resolution of 23 layers. The model top is at 0.002 mb, which allows us to simulate the full stratosphere. This degree of stratospheric resolution is important, as previous studies have shown that models without a full stratosphere may misrepresent stratosphere-troposphere exchange (STE), a significant consideration in this case as approximately half of all ^{10}Be is produced in the stratosphere. Also, models with limited representations of the stratosphere have been shown to be less skilled at simulating lower stratospheric variability than models with higher pressure boundaries (Rind et al., 1999). The formulation for the gravity wave drag is slightly changed from Schmidt et al. (2006) to allow for improved stratospheric circulation and STE. In general, GCMs tend to have levels of STE that are higher than the observed values, and, correspondingly, younger ages of stratospheric air. While the age of air in ModelE's stratosphere also somewhat younger than observations (Rind et al., 2007), it is well simulated in comparison to other GCMs (Shindell et al., 2006).

In all runs, we used the calculated cosmogenic production functions from Masarik and Beer (1999) (see figure 1 of Field et al. (2006) for climatological plots of wet and dry ^{10}Be deposition). All tracers in the model (including ^{10}Be) are subject to the advection, mixing and convection processes consistent with the model air mass fluxes. We assume that there are always sufficient sulfate aerosols available to scavenge the ^{10}Be, and that beryllium isotopes attach to sulfate aerosols immediately after production and are 100% soluble. Aerosol gravitational settling is included, and in stratiform and convective clouds, aerosol species

are transported, dissolved, evaporated and scavenged according to processes for each cloud type. The model also allows for faster settling of fine aerosols in the stratosphere, where the mean free path exceeds the particle radius (Koch and Rind, 1998).

In the boundary conditions near the surface, ^{10}Be is handled using the same turbulent exchange coefficients as the model humidity. The dry deposition scheme, which is based on the resistance-in-series scheme described in Wesely and Hicks (1977) derived from the Harvard GISS chemical transport model (e.g. Chin et al. (1996)), is fully coupled to the GCM processes and makes use of the GCM-assumed leaf area indices, surface types, radiation, boundary layer height, Monin-Obhukov length, etc. (Koch et al., 2006).

3.4   Experimental Design

To simulate the climate changes that might have taken place during the MM, we performed a suite of model runs to capture a range of possible solar forcings, volcanic changes and climate responses. The different experiments are summarized in Table 3.1. The yardstick for our solar forcing was the spectral and TSI changes between a present-day solar maximum and solar minimum (1979 and 1986 respectively). There is not a straightforward relationship between sunspot number and TSI, nor between cosmogenic isotopes and TSI. Therefore, estimates for how much solar irradiance might have decreased during the Maunder Minimum vary widely, ranging from 0.05% to 0.5% (Hoyt and Schatten, 1993; Lean et al., 1995; Lean, 2000). To address this uncertainty, we performed four sets of experiments to simulate what the solar-related impact on ice-core ^{10}Be would be like for a ΔTSI equivalent in magnitude to one, two, three, and four times the change from 1979 to 1986. The ΔTSI from 1979 to 1986 is 0.075%, which places our 1xΔTSI experiments at the low end of the estimated MM range (Foukal et al., 2006). We simulate the 2xΔTSI scenario using data from 1912 (TSI = 1364.57 W/m^2, about a 0.15% change from 1979) (Lean et al., 2002).

To simulate the 3xΔTSI and 4xΔTSI scenarios, we calculated the 1979-to-1986 changes for TSI, tripled and quadrupled them, and forced the model with the resulting changes. The same process was also applied to the three UV wavelength bands in the GCM (100-295 nm, 295-310 nm, and 310-366 nm) that affect stratospheric ozone in the model, giving an enhanced UV variability compared to the changes in TSI. For the different amounts of UV changes, ozone concentrations are prescribed according to the results of previous model experiments involving fully coupled ozone chemistry (Shindell et al., 2006). Over the UV bands, the radiation changes range from 0.5% to 5.2% for the 3xΔTSI and 4xΔTSI runs, with greater varibility at the shorter wavelengths.

For the control scenario, we set [10]Be production equal to what it would be for ϕ = 700 MeV, which is the approximate midpoint for solar modulation between present-day solar maxima and minima (Masarik and Beer, 1999). To simulate the increased production expected during the MM, we ran the model with ϕ = 500 MeV (the approximate value observed during recent solar minima) and also with ϕ = 100 MeV, which is comparable to the MM production value estimated in McCracken et al. (2004) using [10]Be records from Dye 3 and South Pole (ϕ = 84 MeV); to the average value from 1645-1715 (ϕ = 127 MeV) estimated from ^{14}C data in Muscheler et al. (2007); to the value estimated in Vonmoos et al. (2006) using [10]Be from the GRIP ice core (ϕ = approx. 200 MeV); and to the value estimated in Steinhilber et al. (2008) based on a composite of three ϕ reconstructions (ϕ = approx. 290 MeV).

Along with solar changes, volcanic eruptions were also an important climate forcing in the preindustrial period. We performed an additional set of experiments to assess the possible impact. According to Crowley (2000), the mean negative volcanic forcing between 1660-1690 was about 0.16 W/m^2 compared to a century later. To simulate the combined effect of volcanism and TSI changes, we ran the model with a constant stratospheric aerosol radiative forcing of -0.16 W/m^2 and ϕ = 100 MeV. We performed these volcanic simulations with TSI values for 1979, 1xΔTSI and 2xΔTSI. Volcanic aerosol properties are defined as

Table 3.1: Maunder Minimum experiments

Run	TSI (W/m^2)	% Change from 1979	Additional forcing
solar max (Sx), 1979	1366.68	-	
1 x solar min (1Sn), 1986	1365.65	0.075%	
2 x solar min (2Sn), 1912	1364.57	0.15%	
3 x solar min (3Sn)	1363.59	0.23%	
4 x solar min (4Sn)	1362.56	0.30%	
volcanic runs:			
0SnV, 1979	1366.68	-	-0.16 W/m^2 stratospheric aerosol forcing
1SnV, 1986	1365.65	0.075%	same as above
2SnV, 1912	1364.57	0.15%	same as above

in Sato et al. (1993).

For all experiments, we configured the model with a preindustrial atmosphere and a mixed-layer ocean since the multidecadal duration of the MM would make it possible for ocean temperatures to respond to potential irradiance changes. In all simulations, a 20-year spin-up period was used to ensure that equilibrium had been reached for sea-surface temperatures and for the atmospheric distribution of cosmogenic isotopes. The results for all experiments were averaged over the 30 years following the spin-up period.

3.5 Climate Response to Solar Forcing

Reconstructions of northern hemisphere (NH) surface air temperature from various proxies (ice cores, corals, tree rings and other sources) indicate that during the late 17th century, NH temperatures are estimated to have cooled 0.2 to 0.6° C relative to the 1961-1990 mean value, and to have changed (with less definitive cooling) from +0.1 to -0.3° C

relative to the 1850-1900 mean value (Jones et al., 1998; Briffa et al., 2001; Mann et al., 1999; Briffa, 2000; Overpeck et al., 2004; Crowley and Lowery, 2000). In Europe during the same time period, wintertime temperatures are estimated to have been about -0.25° C compared to the 1850-1900 mean (Luterbacher et al., 2004). We performed our solar max. simulation with a preindustrial atmosphere in order to avoid the effects of anthropogenic climate change; for this reason, we would expect our simulated cooling to correspond more closely to the reconstructed temperature estimates relative to the 1850-1900 values, as solar forcing is a much larger fraction of the total probable forcing relative to 1850-1900 than it is relative to 1961-1990. The degree of global, NH and European cooling in the different solar min. runs relative to the solar max. run is shown in Table 3.2. The amount of global cooling that takes place in the model is fairly linear with respect to the magnitude of the TSI changes, with approximately 0.11° C of cooling for each multiple of sunspot-cycle forcing. For the global mean and NH temperature changes, all of the simulated values fall within the reconstructed range except for the 4Sn run, which is somewhat cooler; for European wintertime temperatures, both the 3Sn and 4Sn simulations are cooler than the reconstructed estimates. The temperature changes in these experiments are similar to those from other MM modeling experiments, such as Shindell et al. (2001) (global mean cooling of 0.34° C, driven by solar forcing only, approx. 2xΔTSI). The model used in Shindell et al. (2001) is an older version than is used here, in particular having lower horizontal resolution (8° x 10°) and older versions of the climate model parameterizations. Our temperature changes are also comparable to those found in Langematz et al. (2005) (0.86° C cooling for the NH relative to present-day conditions, forced with greenhouse gas changes and irradiance changes of about 2.5xΔTSI) and Heikkilä et al. (2008) (global mean cooling of 0.7 ° C relative to the present day, forced with prescribed SSTs, greenhouse gas changes and approximately 1.5xΔTSI).

Around the Mediterranean, simulated temperatures stay the same or warm slightly as irradiance decreases. This warming is accompanied by small increases in wintertime pre-

cipitation (up to 0.3 mm/day). The combination of warm, moist wintertime conditions around the Mediterranean is indicative of the negative phase of the North Atlantic Oscillation (NAO) – the large-scale dipole of atmospheric pressure that acts as the dominant mode of winter climate variability over the North Atlantic. The NAO index is typically defined as the difference in sea-level pressure between Iceland and the Azores, and is described as being in a negative phase when that pressure gradient is lower than usual. Reconstructions of the NAO using ice cores, tree rings, documentary evidence and other proxies indicate that the NAO index was predominantly negative during the MM (Luterbacher et al., 2004; Appenzeller et al., 1998; Rodrigo et al., 2001). While differences in model configurations can lead to different degrees of sea level pressure response (Miller et al., 2006; Palmer et al., 2004), previous modeling experiments have shown a sensitivity to NAO changes caused by external forcings (Shindell et al., 1999, 2001; Gillett et al., 2002). A comparable response is seen here, with positive sea-level pressure anomalies on the order of 0.8-3.2 mb over Iceland and negative anomalies of 0.1-1.1 mb over the Azores for decreasing solar irradiance.

The negative phase of the NAO seen in the model stems in part from the parameterized change in stratospheric ozone associated with the changes in solar irradiance (Shindell et al., 2006). Because the UV radiation in the solar min. simulations is reduced, temperatures in the upper stratosphere are cooler – which, combined with the changes in ozone, results in radiative cooling up to 2.4° C in both the upper and lower stratosphere. This cooling reduces the equator-to-pole temperature gradient in the lower stratosphere. A reduction in stability caused by the cooling aloft leads to increased eddy kinetic energy in NH midlatitudes. This can lead to changes in planetary wave propagation at higher altitudes and towards the pole, causing a reduction in the northward eddy transport of zonal momentum (up to -10 m^2/s^2). This equatorward momentum transport is accompanied by a weakening of the NH zonal winds (up to -2.2 m/s) and an increase in the northward Eliassen-Palm (EP) flux, producing an anomalous EP flux convergence. The EP flux convergence is as-

sociated with reduced poleward transport of quasi-geostrophic potential vorticity, implying less positive vorticity at higher latitudes and therefore higher sea-level pressure, which is consistent with the negative NAO seen in the model results (Shindell et al., 2001).

Overall, the model can simulate the approximate degree of cooling and also the NH sea-level pressure changes (associated with the negative phase of the NAO) that are thought to have characterized the climate during the MM. With the exception of the cooling in the 4Sn scenario (which exceeds the estimates of most temperature reconstructions), the range of the estimates for the reconstructed MM temperatures makes it difficult to select a single solar min. run as a best match for the MM paleodata.

3.5.1   Climate Response to Volcanic Forcing

The global, NH and European wintertime cooling for the volcanic runs is shown in Table 3.2. In the global mean and also for the NH, the volcanic forcing used in these experiments is enough to cause temperature changes of about the same magnitude as a single solar cycle's worth of TSI forcing. For the European wintertime temperatures, the cooling in the 0SnV run is approximately the same as for the 1Sn run (-0.16 vs. -0.15), however the cooling in 1SnV and 2SnV is less than the cooling in 2Sn and 3Sn respectively, suggesting that European winter temperatures do not respond linearly to the volcanic forcing used here. Volcanic aerosols also warm the tropical lower stratosphere, which can affect wave energy propagation and high latitude response.

Previous experiments with GISS ModelE have demonstrated that volcanic aerosols lead to a positive phase of the NAO for the winters immediately following an eruption, but also that the effect of reduced TSI dominates when solar forcing and volcanic forcing are applied in tandem, leading to a NH climate response similar to that seen during the late MM (Shindell et al., 2004). In our runs, the phase of the NAO relative to the control is negative in all three scenarios with volcanic forcing. In the experiments with only solar forcing,

atmospheric cooling at low latitudes extends from the troposphere to the stratosphere. In the volcanic runs, the low-latitude cooling is limited to the troposphere, since the aerosols in the stratosphere absorb solar radiation and create moderate warming aloft. However the resulting changes in the latitudinal temperature gradient are sufficient to trigger dynamical changes that are basically the same as those in the solar-only runs, demonstrating the dominance of TSI-related climate changes relative to the effects of moderate, continuous volcanic aerosol forcing.

In these simulations, the cooling associated with volcanic aerosol forcing and also the persistence of a negative phase of the NAO suggest that a range of volcanic and solar changes could have created conditions that match reconstructions of the MM climate. Further simulations with longer durations will be needed in order to determine more specific constraints on how solar and volcanic changes each might have contributed to the observed climate changes.
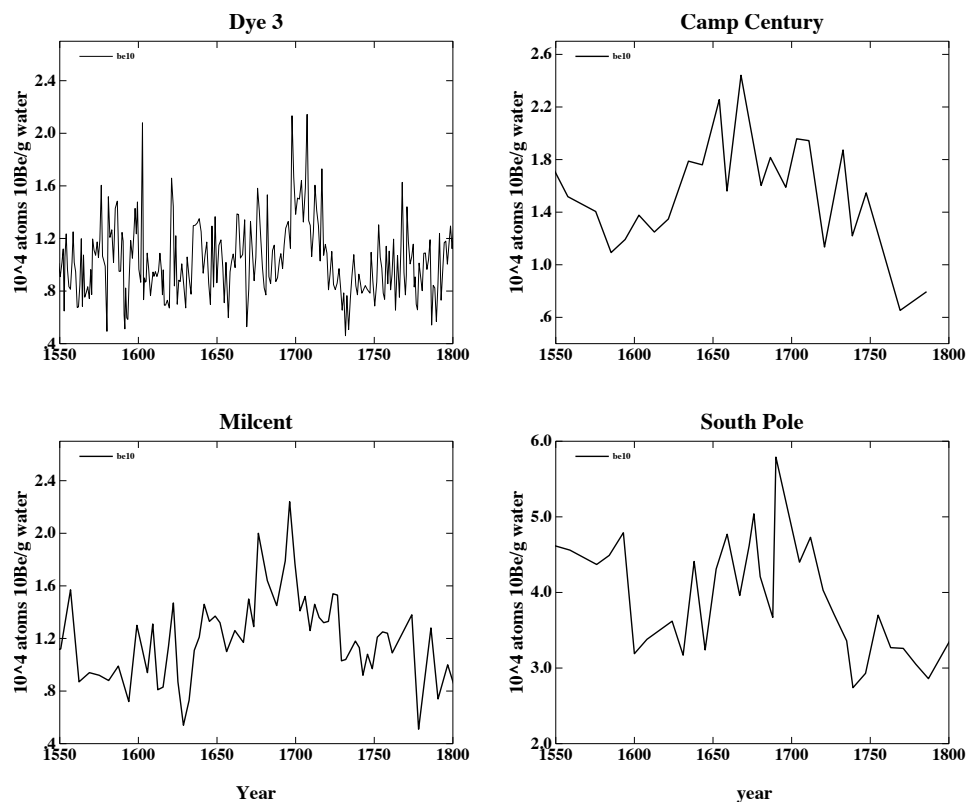
Figure 3.1: [10]Be snow concentration at ice-core locations for 1550-1800. Data: Beer et al. (1990) (Dye 3), Beer et al. (1988) (Camp Century), Beer et al. (1983) (Milcent), Raisbeck et al. (1990)(South Pole).

Table 3.2: Model results: surface air temperature changes, relative to Sx run ($^\circ$ C)

Run	Global Mean	N. Hem.	N. Hem. Land	Europe, winter
1Sn	-0.14	-0.12	-0.15	-0.15
2Sn	-0.21	-0.24	-0.26	-0.30
3Sn	-0.30	-0.31	-0.38	-0.41
4Sn	-0.44	-0.45	-0.55	-0.53
0SnV	-0.12	-0.11	-0.16	-0.16
1SnV	-0.21	-0.21	-0.27	-0.22
2SnV	-0.31	-0.32	-0.40	-0.30

3.6 ^{10}Be Response to Production and Climate Change

3.6.1 Solar impacts

In our simulations, climate changes resulting from reduced TSI affect the atmospheric transport of ^{10}Be in some respects, however changes in ^{10}Be deposition and concentration at the surface tend to be relatively small. Land and Feichter (2003) found that the transformed Eulerian mean meridional circulation in the stratosphere increases in a warmer climate, and that stratospheric ^{10}Be concentrations tend to decrease. Consistently, in our solar min. runs, we find that transformed streamfunction values decrease by 5-35% in the NH stratosphere relative to the solar max. scenario. As a result of the changes in stratospheric circulation, stratospheric ^{10}Be concentrations increase up to 7%, comparable to the increases shown in figure 2.13.

In both hemispheres, colder temperatures at the surface and increased high-latitude sea level pressure lead to reduced precipitation over Greenland and Antarctica, which allows tropospheric concentrations of ^{10}Be over these areas to increase. Dry deposition of ^{10}Be at

high latitudes increases accordingly, however because of the relative predominance of ^{10}Be in wet deposition, the impact of climate changes on total ^{10}Be deposition (wet plus dry) is negligible. (In contrast, Heikkilä et al. (2008) show depositional changes in ^{10}Be over Greenland that range from 20 to 200%, however their simulations feature a global cooling of 0.7 $^\circ$C and a change in ϕ from 700 MeV to 200 MeV and so are not strictly comparable.) The limited impact of solar forcing on our ^{10}Be deposition is illustrated in figure 3.2, which shows the zonal average percent increase in total ^{10}Be deposition for the four solar min. runs relative to the solar max. run (results are shown for $\phi = 500$ MeV, which closely resemble both the results for $\phi = 100$ MeV and the runs with volcanic forcing.) Despite the different levels of solar forcing, the levels of zonal mean deposition change for the four runs agree with each other within several percent. The higher levels of ^{10}Be deposition at mid- and high latitudes reflect the fact that ^{10}Be production is greater at those latitudes, and also indicate the degree to which ^{10}Be deposition at higher latitudes is representative of the global average production rate (high levels of atmospheric mixing) or the local production rate (limited atmospheric mixing). The polar enhancement in ^{10}Be deposition relative to other latitudes (calculated as the percent change in high-latitude deposition divided by the percent change in solar-related global average production) is approximately 1.3, similar to previously modeled and estimated values (Field et al., 2006; Bard et al., 1997).

Similarly, figure 3.3 shows the percent change in ^{10}Be snow concentration over Greenland (due only to TSI-related climate changes, not to production change) for the 1Sn, 2Sn, 3Sn and 4Sn scenarios relative to the Sx run (results are shown for $\phi = 100$ MeV, which closely resemble the results for $\phi = 500$ MeV (not shown)). Excepting the anomalous behavior of a few of the Greenland gridboxes (likely due to limitations in the model's topographical and spatial resolution), there is a consistent pattern of increased ^{10}Be snow concentration over northeast Greenland. However, despite the progressive cooling evident in Table 3.2, there is no clear trend in the pattern or magnitude of the concentration changes as TSI decreases. When data are grouped instead by the amount of production change (ϕ

= 500 MeV and ϕ = 100 MeV) rather than by the amount of TSI change, a clear distinction emerges. Table 3.3 shows simulated changes in ^{10}Be snow concentration values at six coring sites for the two different levels of production change. Data are shown for 1Sn-4Sn climate forcings, and also for the case of no change in TSI (0Sn). The concentration changes for ϕ = 500 MeV and ϕ = 100 MeV are closely clustered around low and high values respectively, with no overlap between concentration values for the two different levels of production. Changes in production therefore have a much more robust impact on ^{10}Be snow concentration than do TSI-related climate changes for this range of forcing.

In order to quantify the relative importance of production changes and climate changes, we used multiple linear regression of modeled ^{10}Be concentration with respect to ϕ changes and TSI forcing for the six ice-core locations. The impacts of production change and climate change were only both significant at one location (Summit); at all other locations, only production change had a significant impact on ^{10}Be concentration. When we performed the same analysis on all Greenland locations collectively, climate and production both were significant over Greenland, with ^{10}Be concentration changing about 9% per 100 MeV change in ϕ and 1.3% for each solar cycle of TSI change. When we analyzed both Antarctic locations, only production was significant, again with approximately a 9% change in ^{10}Be concentration per 100 MeV change in ϕ.

Figure 3.4 summarizes the effects of both production change and TSI-related climate change for four ice-core locations. Each line shows the percent change in ^{10}Be snow concentration relative to the control run for a given value of ϕ. For the ϕ = 700 MeV data, the model was forced with TSI changes while ^{10}Be production was kept constant. The plots show how concentration is affected at each level of solar forcing and also for the case of no solar forcing (only production changes). The changes in concentration for each given value of ϕ are clear and consistent from location to location: for each plot, ^{10}Be snow concentration for ϕ = 500 MeV is about 11% greater than the level for ϕ = 700 MeV, and the level for ϕ = 100 MeV is about 50% greater. However there are no clear trends associated with the

Percent change in total 10Be deposition
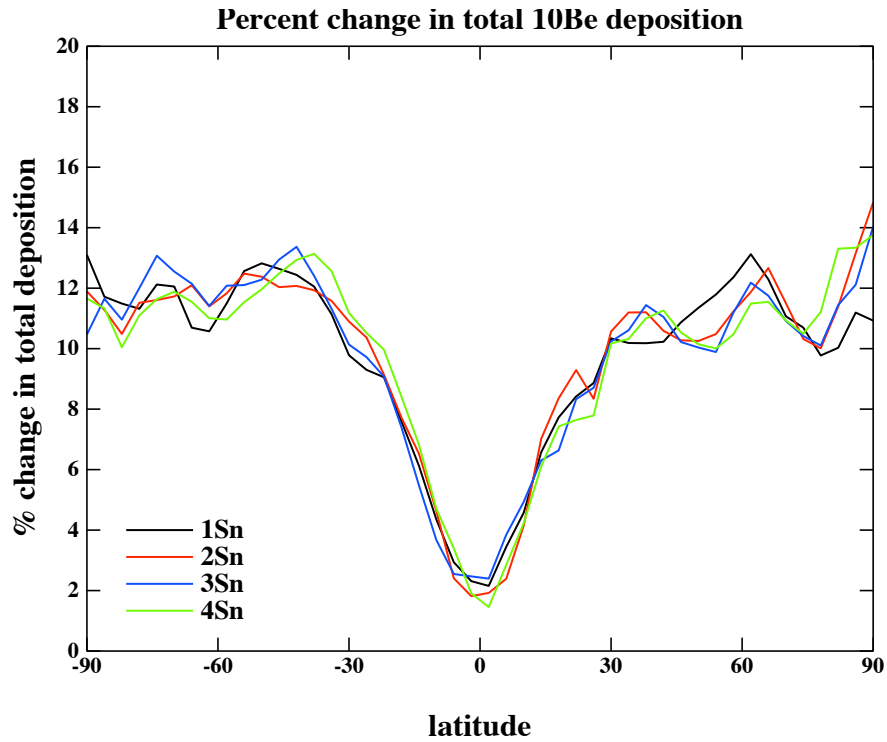
Figure 3.2: Percent change in zonal mean total deposition of modeled ^{10}Be. All data shown are for runs with ϕ = 500 MeV, relative to the solar max. run (ϕ = 700 MeV), and all data are 30-year averages. The pattern of change is dominated by the production change, while climate has little impact on the zonal mean deposition.

effects of solar-related climate change, which in almost all cases are relatively small and not necessarily monotonic.
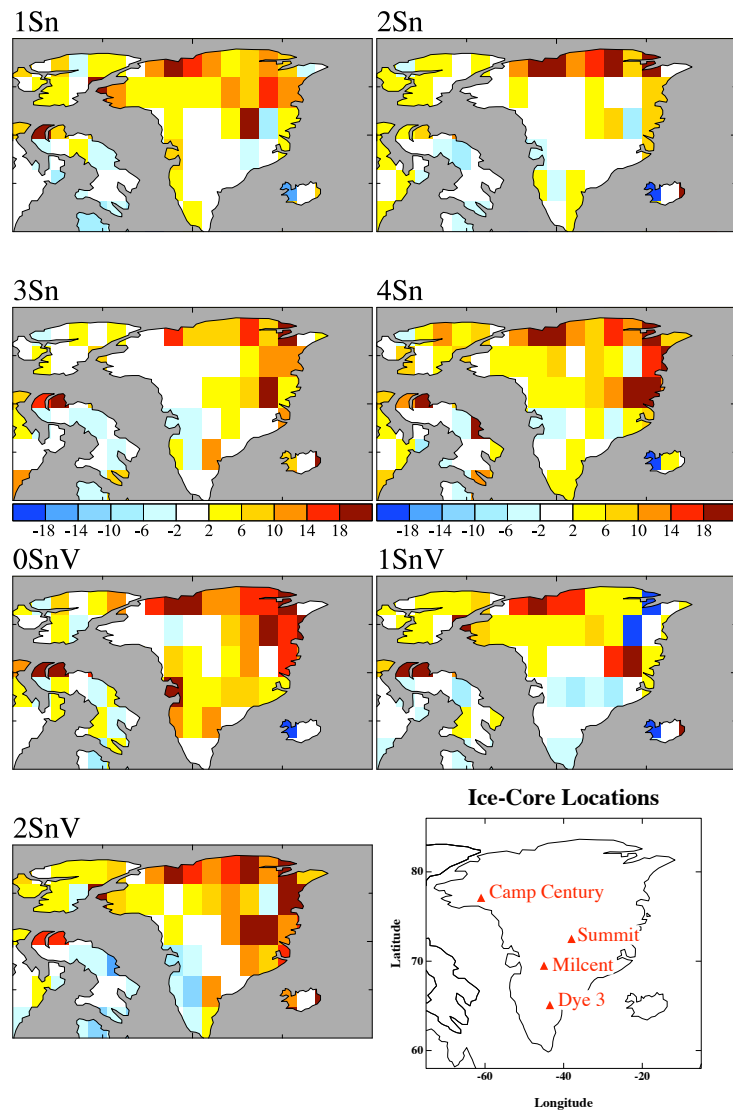
Figure 3.3: Percent change in modeled [10]Be snow concentration due to TSI-related and/or volcanic-related climate changes.
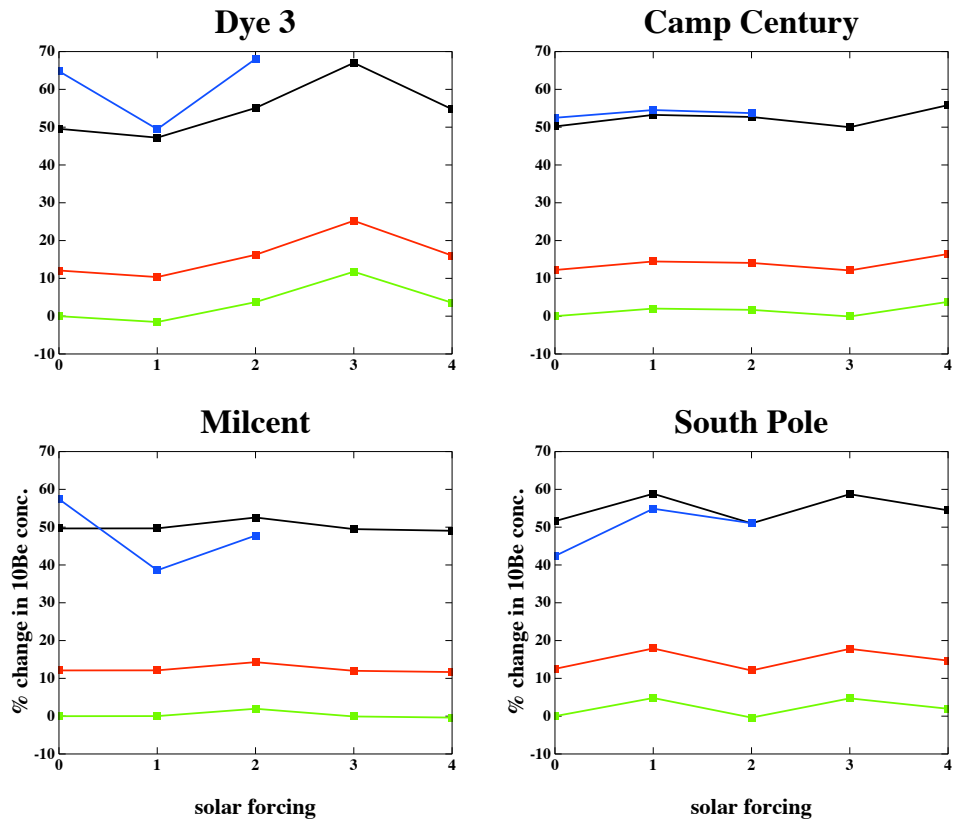
Figure 3.4: Percent change in modeled ^{10}Be snow concentration relative to the Sx run for different ice-core locations. Key: black line shows data for ϕ=100 MeV; red line shows data for ϕ=500 MeV; green line shows data for ϕ=700 MeV; blue line shows data for ϕ=100 MeV with volcanic forcing.

Table 3.3: Percent increase in modeled ^{10}Be snow concentration, experiment - control (Sx, ϕ = 700 MeV), $\pm$ 1σ.

Run, ϕ	Dye 3	Camp Century	Milcent	Summit	Taylor Dome	S. Pole
0Sn, 500	12 $\pm$ 3	12 $\pm$ 1	12 $\pm$ 2	12 $\pm$ 1	13 $\pm$ 1	13 $\pm$ 1
1Sn, 500	10 $\pm$ 2	14 $\pm$ 1	12 $\pm$ 2	15 $\pm$ 1	19 $\pm$ 2	18 $\pm$ 1
2Sn, 500	16 $\pm$ 2	14 $\pm$ 1	14 $\pm$ 2	18 $\pm$ 1	14 $\pm$ 1	12 $\pm$ 1
3Sn, 500	25 $\pm$ 3	12 $\pm$ 1	12 $\pm$ 2	16 $\pm$ 1	17 $\pm$ 1	18 $\pm$ 1
4Sn, 500	16 $\pm$ 2	16 $\pm$ 1	12 $\pm$ 2	22 $\pm$ 1	20 $\pm$ 1	15 $\pm$ 1
0Sn, 100	50 $\pm$ 3	50 $\pm$ 1	47 $\pm$ 2	50 $\pm$ 1	52 $\pm$ 2	52 $\pm$ 1
1Sn, 100	47 $\pm$ 3	53 $\pm$ 1	47 $\pm$ 2	53 $\pm$ 1	61 $\pm$ 2	59 $\pm$ 1
2Sn, 100	55 $\pm$ 3	53 $\pm$ 1	53 $\pm$ 2	57 $\pm$ 2	54 $\pm$ 2	51 $\pm$ 1
3Sn, 100	67 $\pm$ 3	50 $\pm$ 1	49 $\pm$ 2	55 $\pm$ 1	57 $\pm$ 2	59 $\pm$ 1
4Sn, 100	54 $\pm$ 3	56 $\pm$ 1	49 $\pm$ 2	64 $\pm$ 2	62 $\pm$ 2	54 $\pm$ 2
0SnV, 100	65 $\pm$ 3	52 $\pm$ 1	57 $\pm$ 2	58 $\pm$ 2	69 $\pm$ 1	42 $\pm$ 1
1SnV, 100	49 $\pm$ 3	55 $\pm$ 1	39 $\pm$ 2	52 $\pm$ 2	68 $\pm$ 1	55 $\pm$ 1
2SnV, 100	68 $\pm$ 3	54 $\pm$ 1	48 $\pm$ 2	71 $\pm$ 2	67 $\pm$ 2	51 $\pm$ 1

Table 3.4: Observed ^{10}Be snow concentration, percent change during the Maunder Minimum (1645-1715). For Dye 3, Milcent and South Pole, the 70-year reference period is 1730-1800. For Camp Century, the reference period is 1317-1396. Estimates of the uncertainty in the mean are shown when possible. Data: Beer et al. (1990) (Dye 3), Beer et al. (1988) (Camp Century), Beer et al. (1983) (Milcent), Raisbeck and Yiou (2004) (South Pole).

Location	1650-1700 vs. 1550-1600	MM vs. 70-yr ave.	MM vs. long-term ave.
Dye 3	10 ± 6	25 ± 5	12 ± 4
Camp Century	36 ± 14	46 ± 12	53 ± 9
Milcent	47 ± 14	41 ± 10	30 ± 6
South Pole	5 ± 7	30 ± 7	11 ± 5
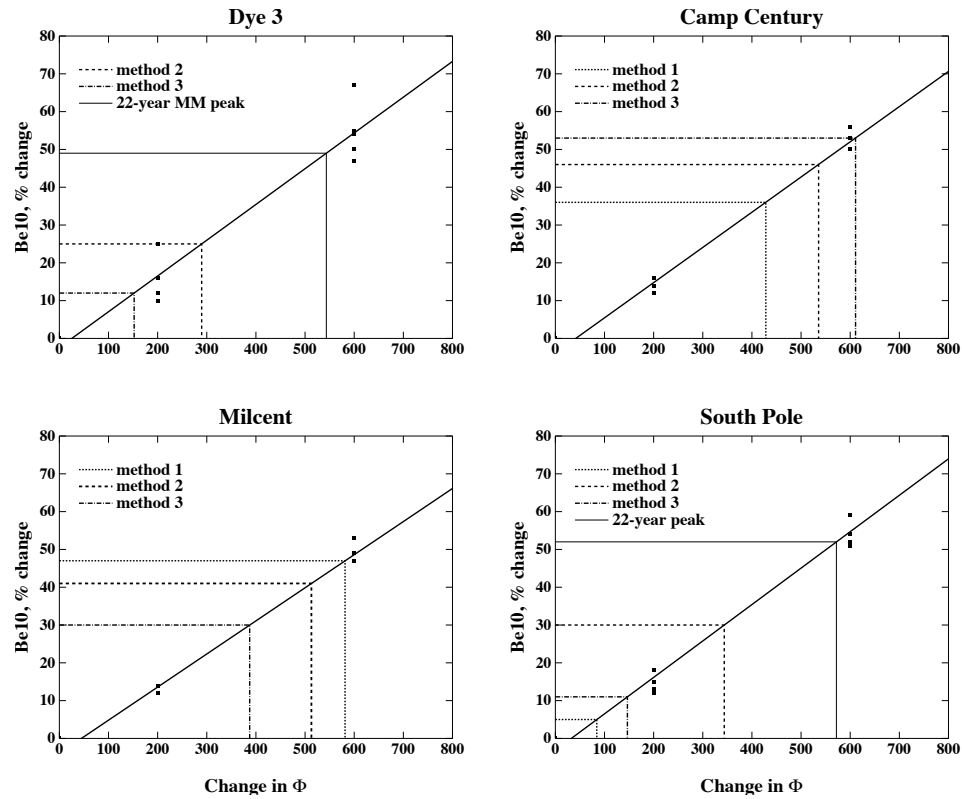
Figure 3.5: Comparison between the percent changes in observed MM ^{10}Be snow concentration for the different methods described in section 6 (dotted lines) and modeled ^{10}Be concentration changes (solid squares). The solid line shows the modeled ^{10}Be snow concentrations regressed against the associated change in ϕ. Key to observed changes in ^{10}Be snow concentration: 1 = 1650-1700 vs. 1550-1600; 2 = MM vs. 70-year mean, 3 = MM vs. long-term mean (see Table 3.4). The 22-year value for Dye 3 is as described in section 6. The corresponding changes in ϕ can be read off the verticals.

3.6.2 Volcanic impacts

The additional impact of volcanic aerosol forcing on simulated ^{10}Be is very small compared to the solar-related climate effects: results for the 0SnV, 1SnV and 2SnV runs differ little from 1Sn and 2Sn runs. The reductions in transformed streamfunction values closely resemble the changes in the simulations with only solar forcing; the increases in atmospheric ^{10}Be concentrations are similar as well (9%). Zonal changes in wet, dry and total ^{10}Be deposition, as mentioned in the previous section, are generally the same as for the solar-forcing runs, with negligible changes in total deposition regardless of the degree of TSI forcing. Similarly, although there are consistent increases in ^{10}Be snow concentration changes over northeast Greenland (figure 3.3), there is no clear trend associated with the magnitude of the applied forcing.

Figure 3.4 compares ^{10}Be snow concentration changes for the runs with additional volcanic forcing (blue line) to the runs with only solar forcing. While the relative changes in snow concentration are basically the same for the different levels of production change in the runs with only solar forcing, the volcanic runs follow different patterns, resulting in ^{10}Be snow concentrations that may be either higher or lower than the concentrations in the runs with solar forcing alone. For Dye 3, all the ^{10}Be concentration values associated with the volcanically forced runs are higher than the $\phi = 100$ MeV solar-forced values. For South Pole and Milcent, the values for the runs with volcanic forcing are mostly lower, while at Camp Century, the values for the volcanic runs are nearly the same as the values for the runs with only solar forcing. Overall, these results suggest that the simulated effects of combined volcanic and solar forcings do not have a clear signature on large spatial scales. This effect can also be seen in Table 3.3 if one compares the volcanic data with the solar data for $\phi = 100$ MeV. At four of the six locations, the snow concentration values for the volcanic runs either contain outliers that are exceptionally low or high relative to the solar runs (such as the 39% value for 1SnV at Milcent or the 71% value for 2SnV

at Summit) – or, as in the case of Taylor Dome, the volcanic concentrations are all larger than the corresponding solar-only values. It therefore seems possible that for the degree of forcing simulated here, volcanic-related climate effects can potentially have an impact on multidecadal [10]Be snow concentrations, which may make it difficult to determine the concomitant level of TSI change or production change.

3.7   Comparison with [10]Be observations

How can these results be used to interpret the observed [10]Be changes during the MM? Considering the tracer's relatively small response to simulated climate impacts, our results confirm that increased [10]Be concentrations during the MM are largely the result of changes in solar magnetic field strength and attendant cosmic ray modulation. That being said, what was the likely magnitude of that production change? In order to compare our modeled results with the ice-core data, we first need to determine the observed change in [10]Be snow concentrations. However given the quality of the observations, there is some ambiguity in choosing a method for making such a calculation. Table 3.4 shows three ways of estimating the percent change in [10]Be snow concentration (relative to specific baselines) for four different ice-core locations. The concentration changes vary depending on whether the MM values (1) are considered as a 50-year period and compared to the 50-year period 100 years prior, (2) are compared to a subset of the time series that has the same duration as the MM (approx. 70 years) but does not occur during (or has relatively little overlap with) other prolonged solar minima, or (3) are compared to the entire timeseries (which includes the effects of other Grand Minima (McCracken et al., 2004)).

We also consider a fourth method which was used in McCracken et al. (2004) to estimate ϕ during the MM. The authors used data from Dye 3 and South Pole, and at each location took the average of the highest 22-year means for [10]Be snow concentration during both the Maunder and Spoerer (approx. 1420-1540 AD) minima. (In the case of the South

Pole data, the highest 22-year average during the Oort minimum (about 1050 AD) was also used). If we perform the same calculation and compare the resulting ^{10}Be concentrations to the 70-year reference period (method 2), the changes in concentration at South Pole and Dye 3 are about $52 \pm 12\%$ and $49 \pm 8\%$ respectively, resulting in an average change of 51 $\pm 15\%$.

With these different estimates, we can compare the production-related ^{10}Be changes from the model in Table 3.3 to the observed changes in Table 3.4 to see what degree of ϕ change best matches the observations. This comparison is shown in figure 3.5. In each of the four plots, the thick solid line shows the modeled change in ^{10}Be regressed against different changes in ϕ (the modeled values from Table 3.3 appear as solid squares for $\Delta\phi$ values of 200 MeV (for the $\phi = 500$ MeV runs) and 600 MeV (for the $\phi = 100$ MeV runs)). The results show the lack of a strong climate signal, with observed percent concentration change values ranging widely depending on location and also on which method of estimating the observed ^{10}Be change is used. For the concentration change estimates based on comparing 1650-1700 with 1550-1600 (method 1), the implied changes in ϕ range from 84 MeV (at South Pole) to 513 ± 228 MeV (at Milcent). For method 3 (MM vs. the long-term mean of the time series), the estimated ϕ changes range from about 152 ± 85 MeV (Dye 3) to 611 ± 193 MeV (Camp Century).

As mentioned earlier, McCracken et al. (2004) has estimated that $\phi = 84 \pm 30$ MeV during the MM, or rather that a change in ϕ of about 616 MeV took place relative to the approximate present-day average value of $\phi = 700$. This $\Delta\phi = 616$ MeV is larger than all but one of our estimated ϕ values. However if we recalculate our estimates based on the 22-year South Pole and Dye 3 averages described earlier, the change in ϕ increases significantly. Depending on which location we use, the change in ϕ ranges from 543 to 572 MeV. While the relationship in this paper between ϕ and ^{10}Be concentration is based on the modeled changes in ^{10}Be at different ice-core locations, in McCracken et al. (2004) the same relationship is determined from the flux function described in Webber and Higbie

(2003) as well as the atmospheric mixing model discussed in McCracken (2004). Despite the differences between these two methodologies, the $\Delta\phi$ that we obtain are slightly smaller but comparable to those estimated in McCracken et al. (2004).

Part of the explanation for the discrepancies between our MM ϕ estimates and that of McCracken et al. (2004) may be due to differences in the amount of atmospheric mixing assumed in McCracken et al. (2004) compared to the amount of mixing in ModelE. As mentioned in section 5.1, in our simulations the ratio of the percent change in polar ^{10}Be deposition to the percent change in global average deposition is approximately 1.3, which implies a greater degree of atmospheric mixing that that used in McCracken et al. (2004). If the McCracken et al. (2004) calculations were repeated allowing for more mixing, it is likely that the resulting change in ϕ would be smaller and closer to more of our larger estimates.

Another part of the difference between the ϕ estimates may be related to climate effects. Horiuchi et al. (2008), Bard et al. (2007) and Muscheler et al. (2007) have highlighted some of these concerns, particularly those relating to geographical and temporal variability of snow accumulation, and the effects of that variability on ^{10}Be ice core records. Luterbacher et al. (2004); Jones et al. (1998); Briffa et al. (2001) have shown that the late 1600s and early 1700s were some of the coldest years of the MM, particularly in the NH and Europe. It is possible that these colder temperatures might have led to reduced precipitation around Greenland, resulting in higher ^{10}Be concentrations in the Dye 3 record for those years. Such an outcome would be similar to the findings discussed in Field et al. (2006), in which it was shown that significant reductions in ^{10}Be snow concentration can be caused by climate forcings alone (with no changes in cosmogenic production levels). As mentioned earlier, we see reduced accumulation in the experiments described here, but no consistent changes in ^{10}Be snow concentration relative to the degree of solar forcing. Nevertheless, even relatively modest amounts of climate variability, such as those shown in the plots for Camp Century and Milcent in figure 3.5, could lead to a difference of as much as 50 MeV

in estimating the potential MM ϕ change. Also, although the relationship between ϕ and sunspots is still incomplete, the fact that sunspot counts for 1690-1715 were about the same or slightly higher than the counts during the rest of the MM suggests the possibility that local climate changes rather than production changes might have been partially responsible for the high [10]Be concentrations at Dye 3 – which, in turn, might lead one to calculate a larger change in ϕ than what might have been inferred in the absence of climate effects.

We see similar climate impacts in the analysis of our runs including enhanced volcanism. The results for Dye 3 in figure 3.4 show that, on average, volcanic-related climate effects (blue line) lead to [10]Be concentration changes that are about 10% higher than those for equivalent runs with no volcanic effects. While this enhancement of the change in modeled [10]Be concentration is not statistically significant, it suggests the possibility that the effects of volcanic aerosols may have led to higher [10]Be concentrations at Dye 3 during the late MM. Elsewhere, however, such as in the 1SnV run at Milcent (39%) and in the 2SnV run at Summit (71%), the volcanic- and solar-forced changes in [10]Be concentration can be either notably reduced or enhanced relative to the simulations forced with TSI changes alone. It is possible that the model might have a different response to intermittent volcanism rather than the constant, sustained, low-level volcanic forcing that we used in these simulations. Our results suggest that longer simulations are needed in order to clearly distinguish the effects of volcanic forcing from the weather noise.

In addition to the ambiguities surrounding the methods for calculating MM [10]Be concentration changes and also the potential effects of climate change during that time, other factors exist that may have contributed to the uncertainties of our results. Regarding the observations, there is a fair amount of site-to-site variability in the changes we have estimated from the [10]Be concentration data. Local climate effects on Greenland are probably one of the main causes of the observed variability (Mosley-Thompson et al., 2001). Additionally, ice-core dating errors could potentially reduce the agreement between observed changes from site to site. Such errors can be as large as 2% over the past 1000 years but

are often smaller and are less likely to be important contributors to the overall uncertainty (Muscheler et al., 2007). There are also issues relating to various characteristics of the experimental design, particularly the fact that estimates for the [10]Be production rate vary by as much as a factor of 2 (Lal and Peters, 1967; Oeschger et al., 1969; O'Brien et al., 1963; Masarik and Reedy, 1995; Masarik and Beer, 1999). However, results here have been reported in terms of percent change from the control run, which should reduce the potential effect of errors in the magnitude of [10]Be production.

Concerning the GCM itself, there are other considerations such as uncertainties relating to the model's climate sensitivity, which we have tried to address by performing simulations using a range of climate forcings. There are also uncertainties in the degree of TSI change and volcanic aerosol forcing during the MM. Another potential issue is the model's ability to simulate the general climate over Greenland and Antarctica. The quality of model results in these areas has been a focus of ongoing work, and we plan to continue this by performing (1) simulations with higher spatial and vertical resolution, which would likely improve stratospheric dynamics and the consistency of gridbox-level performance, (2) simulations with a fully coupled ocean and North Atlantic Deep Water cahnges, and (3) simulations spanning longer time periods, which should help clarify subtler changes such as those caused by volcanic aerosol forcing.

3.8   Conclusions

Using the GISS ModelE GCM, it is possible to recreate the large-scale features of the MM climate using both solar forcings and volcanic forcings, or with solar forcings alone. If both volcanic and solar forcings are applied, the amount of solar forcing required to achieve a realistic amount of surface cooling is reduced. In the experiments with both conventional and relatively large values of [10]Be production changes and solar forcing, the simulated [10]Be snow concentrations are influenced much more strongly by changes in production

than by TSI-related changes in climate. Additional volcanic aerosol forcing does not have a straightforward impact on ^{10}Be over large spatial scales, however, further experiments are needed to better understand the full effects of this type of forcing. In comparing simulated and observed ^{10}Be snow concentration changes, the question of how best to define the observed MM change in ^{10}Be concentration remains ambiguous. The ϕ estimates based on the averages of methods 1, 2 and 3 give MM ϕ values ranging from approximately 280 to 395 MeV. If we look the average of the highest 22-year values for Dye 3 and South Pole, we get an estimate of $\phi = 142 \pm 150$ MeV. However the range of possible ϕ values inferred from time-averaging the other parts of the observed ^{10}Be record that could reasonably be considered representative of the MM suggests that additional analysis and better resolved data are necessary before a more decisive estimate can be made of how ϕ changed during the Maunder Minimum.

CHAPTER 4

MODEL-BASED CONSTRAINTS ON INTERPRETING 20TH CENTURY TRENDS IN ICE CORE ^{10}BE

Submitted to *Journal of Geophysical Research*

Authors: Christy Veeder and Gavin A. Schmidt

4.1   Abstract

Beryllium-10 ice-core records are useful for understanding solar magnetic field changes over time, and in particular over the 20th century, during which there are variety of relevant observations. However, differences between ^{10}Be snow concentration records from different locations complicate the process of developing a coherent understanding of changes in cosmogenic isotope production. We use the Goddard Institute for Space Studies ModelE general circulation model to simulate the production and transport of beryllium isotopes for this time period. We compare our results with surface air observations, and with ice-core records from Dye 3, Taylor Dome and South Pole. We find that unforced weather-related (internal) variability causes modeled trends in ^{10}Be snow concentration to vary from the ensemble mean by 50% and greater at all three ice-core locations. Lower levels of internal variability at Taylor Dome and South Pole relative to Dye 3 make the simulated ^{10}Be values at these locations better estimates of the associated changes in ^{10}Be production. In contrast, a higher degree of climate-related effects at Dye 3 lead to a modeled ^{10}Be snow concentration trend value that is notably more positive than expected based on the applied production changes. Overall, the results imply that during the 20th century, ^{10}Be data from multiple cores are likely to be required to make meaningful inferences about ^{10}Be produc-

tion changes. The model simulations imply that data from Antarctica are likely to be more robust.

4.2   Introduction

Understanding the effect of changes in the sun's activity is an important part of understanding Earth's climate variability, particularly if we want to be able to accurately quantify the effects of anthropogenic climate change relative to natural variations. Cosmogenic isotopes, whose production is linked to variations in solar magnetic activity, can play a key role in this effort. These magnetic activity changes, which affect the degree to which Earth's atmosphere is shielded from galactic cosmic rays (GCR), are correlated with changes in total solar irradiance (TSI) (Lean, 1994; Lean et al., 2002), and have strong 11-year cycles (also known as Schwabe cycles). Increased numbers of sunspots result in both increased TSI and higher levels of GCR shielding (and vice versa during sunspot minima). The physical relationship between this time-varying solar GCR shielding (usually described by the solar modulation parameter ϕ (Gleeson and Axford, 1968)) and sunspot activity is still not completely understood (Muscheler et al., 2005; Mursula et al., 2003). However, the magnitude of ϕ is inversely proportional to the rate of cosmogenic isotope production – hence the usefulness of these isotopes as proxies for changes in TSI.

Two isotopes in particular, beryllium-10 and beryllium-7, are especially useful in this regard. The amplitude of ^{7}Be's production changes is somewhat larger than that for ^{10}Be, and there are also differences between the three-dimensional structures of their production functions, with the ^{7}Be/^{10}Be production ratio varying from about 1.2 at sea level to about 2.6 at the top of the atmosphere (for ϕ=600 MV). However, the fact that ^{7}Be and ^{10}Be share the same transport and removal processes makes analysis of the former a useful analog for understanding the latter. After production in the stratosphere and troposphere, ^{10}Be and ^{7}Be attach to aerosols and are deposited at the surface after 1-2 years, depending on altitude. Beryllium-10's relatively long half life (1.5 million years) makes it well-suited for study on decadal to millenial timescales, and ice-core records provide a rich natural archive for this purpose. While ^{7}Be's 53-day half life makes it unsuitable for ice-core study, it is

much easier to measure, and its concentrations in air are often recorded as part of standard radiation monitoring programs.

Technological developments have made it possible to infer ϕ values – either from neutron monitor data, ionisation chamber data, or various cosmogenic nuclides – over most of the 20th century (Beer, 2000; McCracken and Heikkila, 2003). These can be compared with various ^{10}Be ice-core observations from the same time period. However, ^{10}Be snow concentrations from different ice cores (Beer et al., 1990; Raisbeck et al., 1990; Steig et al., 1996; Vonmoos et al., 2006) often exhibit different features, trends and amplitudes, which complicate the process of comparing and combining records from different locations (Muscheler et al., 2007; Bard et al., 1997, 2007). These discrepancies have led to debate over which ^{10}Be records most accurately reflect changes in ϕ, and by extension, changes in TSI.

General circulation models, with their ability to control climate forcings and cosmogenic isotope production, provide a means for studying these questions. To better understand the relationship between ϕ and records of ^{10}Be from different ice cores, we perform ensemble runs to simulate 20th century climate featuring variable ^{10}Be and ^{7}Be production and forced with transient changes in sea surface temperatures, TSI, and atmospheric composition. We then look at how the model results compare with recent surface air observations and 20th century ice-core records, as well as trends in production and snow concentration at different locations.

4.3 Model Description and Experimental Design

Our experiments were performed using the latest stratospheric version of the Goddard Institute for Space Studies (GISS) ModelE general circulation model (GCM) (Schmidt et al., 2006), which has a horizontal resolution of 4° x 5° (latitude x longitude), 23 vertical layers, and a model top at 0.002 mb. Having the capability to simulate the full stratosphere

is important as approximately half of all ^{10}Be is produced in the stratosphere, and the rate of stratosphere-troposphere exchange is crucial for simulating the correct atmospheric residence time. It is also possible for stratosphere-troposphere exchange to be influenced to some extent by solar activity (Heikkilä et al., 2008). The formulation for the gravity wave drag is slightly changed from Schmidt et al. (2006) to allow for improved stratospheric circulation and stratosphere-troposphere exchange [David Rind, personal communication]. The age of the model's stratospheric air is well simulated in comparison to other GCMs (Shindell et al., 2006), although it is somewhat younger than observed values (Rind et al., 2007).

We assume that the beryllium isotopes attach to sulfate aerosols immediately after production, and that there are always sufficient sulfate aerosols available to scavenge them. Beryllium-bearing aerosols are assumed to be 100% soluble. Aerosol gravitational settling is included, and in stratiform and convective clouds, aerosol species are transported, dissolved, evaporated and scavenged according to processes for each cloud type (Koch et al., 2006). All tracers in the model (including ^{10}Be) are subject to the advection, mixing and convection processes consistent with the model air mass fluxes. The model also allows aerosols to settle more quickly in the stratosphere, where the mean free path exceeds the particle radius (Koch and Rind, 1998).

The dry deposition scheme is based on the resistance-in-series scheme described in Wesely and Hicks (1977) (derived from the Harvard GISS chemical transport model, e.g. Chin et al. (1996)). This deposition scheme is coupled to the GCM processes and makes use of the GCM-assumed leaf area indices, surface types, radiation, boundary layer height, Monin-Obhukov length, etc. (Koch et al., 2006; Wesely, 1989). The turbulent exchange coefficients as the model humidity are also used for ^{10}Be in the boundary conditions near the surface.

To simulate the 20th century, we performed two ensembles, each with five runs. In the first ensemble, we used a preindustrial atmospheric composition and forced the model

only with time-varying 20th century sea surface temperature (SST) and sea ice values. In the second ensemble, we included a comprehensive set of forcings: changing atmospheric composition, transient volcanic eruptions, prescribed SST and sea ice values (the quality of which degrades going back in time), and annually varying solar irradiance with parameterized ozone response (Shindell et al., 2006). In both ensembles, we allowed [10]Be production to vary annually, based on the reconstructed ϕ values based on ^{14}C data from Muscheler et al. (2007) (figure 4.1). For the cosmogenic isotopes, we used a newer version of the Masarik and Beer (1999) production scheme. This newer version more accurately simulates the latitude-dependent production of beryllium isotopes by helium nuclei (alpha particles), which make up about 9% of the GCR particles responsible for [10]Be production (Masarik and Beer, 1999; Field et al., 2006). Use of the newer Masarik and Beer (1999) production scheme results in levels of production that are about 10% higher than those using the earlier version. For all simulations, the model was run from 1880 to 2000. We used the first 20 years of each simulation to allow atmospheric [10]Be concentrations to reach a state of relative equilibrium, and the results shown in this paper are based on the data from 1900 to 2000.
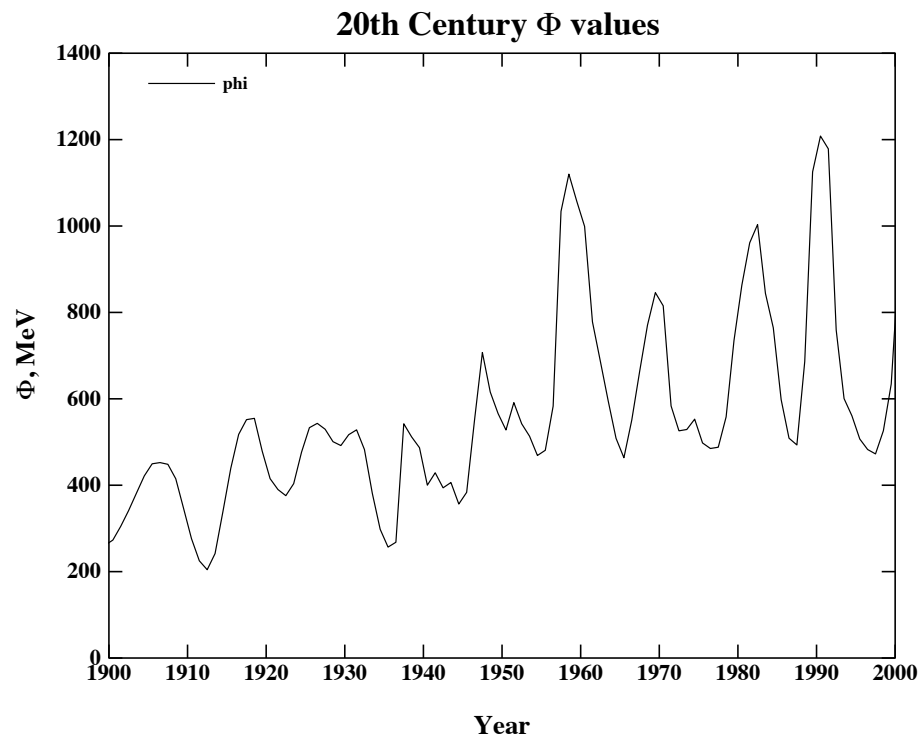
Figure 4.1: 20th century estimated ϕ values (derived from ^{14}C data and neutron monitors) used in the model to drive beryllium isotope production (data: Muscheler et al. (2007)).

4.4 Evaluation with surface-air data

To evaluate how the model simulates beryllium isotopes under 20th century circumstances, we compared the model output with timeseries measurements of [7]Be air concentration from the Environmental Measurements Laboratory's Surface Air Sampling Project (SASP). We compare modeled [7]Be with measurements from 16 SASP stations that have at least 20 years of data. Results for the runs with only SST forcings (not shown) were very similar to those for the simulations with the full set of climate forcings. Figure 4.2 compares the average values of observed [7]Be with the simulated values from the runs with full climate forcings. In an earlier set of ModelE experiments, Koch et al. (2006) found that low-latitude locations tended to have low modeled values of [7]Be relative to the observations, with better performance at mid- and high latitudes. Similarly, in our experiments the low-latitude model values are lower than the corresponding observed values, however the same is also usually true for the data at midlatitude and polar locations. The overall low bias may be due to the production function, which, at 0.035 atoms/cm^2/s, is low relative to some estimates (such as 0.0810 atoms/cm^2/s (Lal and Peters, 1967), 0.0578 atoms/cm^2/s (O'Brien et al., 1978) and 0.062 atoms/cm^2/s (Usoskin and Kovaltsov, 2008)) but higher compared to the estimates of Oeschger et al. (1969) (0.0185 atoms/cm^2/s) and Masarik and Reedy (1995) (0.0129 atoms/cm^2/s).

Figure 4.3 shows the observations as timeseries, at six representative locations, compared with model results for the simulations with the full set of climate forcings. To better illustrate how the model performs despite the bias towards low values, the timeseries plots show variability in terms of percent change from the long-term mean, with the seasonal cycle removed. Solar maxima occurred approximately at 1969, 1980, and 1990, and solar minima occurred approximately at 1977, 1987, and 1996; therefore we would expect to see respectively low and high [7]Be concentrations during those years. These solar-cycle related concentration changes tend not to be as clearly represented at low-latitude locations (like

Peru) as they generally are at midlatitude locations (like Canada and New York). This is expected because of the higher degree of GCR shielding at low latitudes (and because of the higher levels of ^{7}Be production that take place at mid- and high latitudes). While the model does a good job of simulating the relative magnitude of the production-related ^{7}Be concentration changes at midlatitudes, it is less successful in capturing the more extreme variability that is evident in the high-latitude observations. Higher levels of observed variability near the poles may be related to increased ^{7}Be production from low-energy solar particles. These particles can enter the atmosphere more easily at high latitudes, where magnetic shielding is weaker, and are often associated with the solar flares that often characterize the descending limb of the solar cycle (Lal and Peters, 1967; Koch and Mann, 1996). Overall, however, the model does a fairly good job of reproducing the variability of ^{7}Be surface air concentrations, suggesting that the model adequately simulates the transport of ^{7}Be and ^{10}Be, even if the absolute magnitudes of the airborne isotopes are biased low.
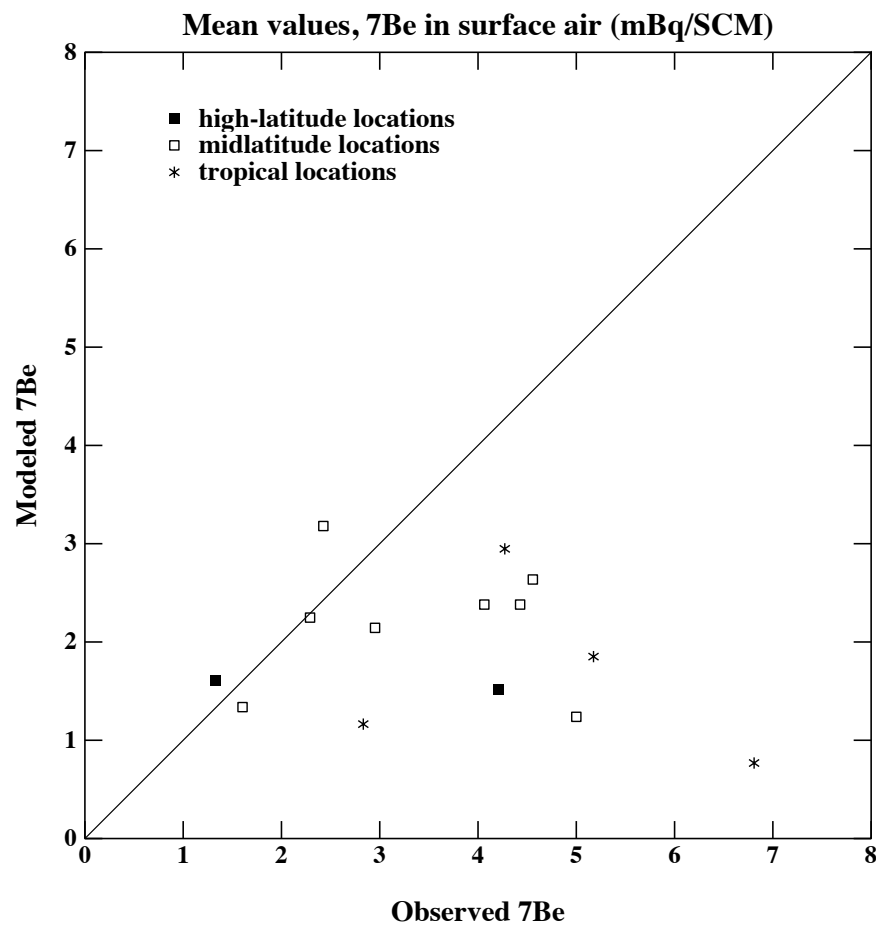
Figure 4.2: Average values for [7]Be air concentrations at SASP locations, except for the Peru, Lima site for clarity (observed value: 13.34 mBq/SCM; model value: 0.98 mBq/SCM. 1 Becquerel = 1 nuclear decay per second.).
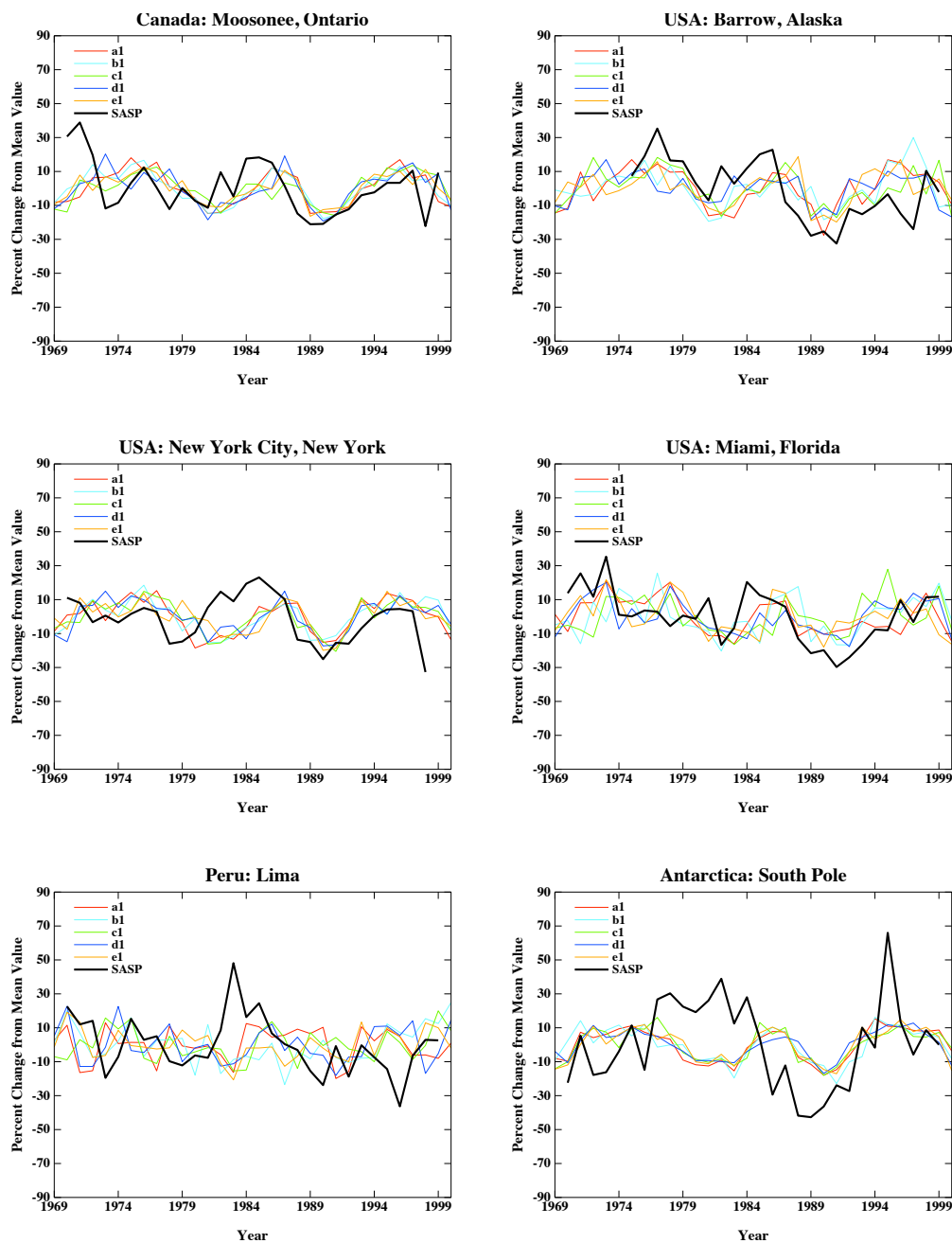
Figure 4.3: [7]Be air concentrations at SASP locations: variabilty in terms of percent change from the long-term mean, with the seasonal cycle removed. The colored lines show the results for the different ensemble members and the black line shows the observations.

4.5   Comparison with ^{10}Be ice-core records

In this section, we compare ice-core data from Dye 3 (Beer et al., 1990) and South Pole (Raisbeck et al., 1990), and firn-core data from Taylor Dome (Steig et al., 1996), with data from the corresponding model gridboxes. Since the observations are given in terms of ^{10}Be snow concentration, we calculate the modeled snow concentration values from the simulated snowfall and ^{10}Be deposition output. Table 4.1 compares observed and modeled snow concentrations at each of the three locations, averaged over the years covered by the observations (1900-1984 for Dye 3, 1922-1994 for Taylor Dome, and 1906-1982 for South Pole). The three data sets collectively cover nearly all of the 20th century, however their overlap period is smaller, spanning the 60 years from 1922-1982. The time resolutions for the three time series also vary: observations at Dye 3 are given on an annual basis, while at Taylor Dome observations are given approximately every 2-3 years, and at South Pole approximately every 6-10 years.

Unlike the general bias toward low model concentrations discussed in the previous section, the modeled ^{10}Be snow concentrations at Dye 3 and Taylor Dome are both very close to but slightly higher than the observed values. At South Pole, however, the simulated concentrations are significantly higher than the observations. While the tendency towards high snow concentrations at South Pole was also the case in earlier work with ModelE (Field et al., 2006), the opposite is the case with the ^{7}Be surface air concentrations discussed in the preceding section: 1.52 mBq/SCM in the model vs. 4.21 mBq/SCM in the observations. The fact that the snow concentrations are high (despite the relatively low surface air concentrations) is mainly due to insufficient snow accumulation in the model. At South Pole, the average 20th century snow accumulation is approximately 1.8 cm/yr (snow water equivalent), lower than the observations, which range from approx. 5 cm/yr to approx. 10 cm/yr (Bromwich, 1988; Mosley-Thompson et al., 1995; Monaghan et al., 2006; van der Veen et al., 1999). Model performance is better at the other two locations: the average

simulated accumulation at Dye 3 is about 60 cm/yr – in good agreement with the 56 cm/yr estimate based on data from 1979-1981 (Vinther et al., 2006) and with the 45 cm/yr estimate based on data from 1976-1997 at North Dye 3 nearby (Mosley-Thompson et al., 2001). At Taylor Dome, the model average is about 16 cm/yr – larger than the approx. 1-12 cm/yr estimate based on ground measurements from 1992-1996 (Morse et al., 1999) and the approx. 7 cm/yr based on firn-core estimates from 1954-1964 (Steig et al., 1998), but more comparable to the approx. 12-14 cm/yr estimate based on satellite data (Morse et al., 1999). Additional discussion of the model climatology can be found in Field et al. (2006) and Field et al. (2009).

Here we normalize our results and the observations by the long-term average value for each location in order to illustrate more robustly the nature of the changes. Figure 4.4 shows [10]Be snow concentration over time at the three locations. The plots show the five-run average for the model runs with the full set of climate forcings, as well as the minimum and maximum simulated values from the ensemble (results for the simulations with SST forcing only were very similar and are not shown here). For Dye 3, the observations and model results are smoothed with a 3-point binomial filter. For Taylor Dome and South Pole, the modeled data have been averaged over the same time intervals as those inferred for the observations. The top panel of figure 4.4 also shows the years of observed solar minima and maxima, according to international sunspot counts: each plus and minus symbol marks the year after the observed sunspot maxima and minima (respectively), in order to account for [10]Be's approximate 1-year atmospheric residence time. The minima and maxima indicated here do not necessarily occur simultaneously with the years of minimum and maximum ϕ values, however they provide a qualitative indication of when those production changes occured. Table 4.2 also shows the minimum and maximum values for both the model data and the observations at each core site.

The 5-run averages can be considered an estimate of the expected climatological depiction of changes in [10]Be snow concentration, while the observations are most analogous to

the results of a single model run. We would therefore hope that the observations fall within the envelope of the minimum and maximum simulated values. Despite some small excursions, this is largely the case for Dye 3. The 11-year solar signal is also visible for most of the record (though somewhat less so from about 1930-1950) and the associated peaks and troughs in the simulated ^{10}Be generally correspond well with those in the observations.

In the plot for Taylor Dome, the model's aforementioned tendency towards lower levels of high-latitude variability is more apparent, with the observations extending both above and below the envelope of the maximum/minimum values at several points in the record. This smaller range of simulated variability can also be seen in the differences in amplitude between the model and observations for sunspot minima (for instance, the minimum around 1977) and maxima (around 1980). Another characteristic of the Taylor Dome record is that the model's production-related peaks and troughs sometimes lag slightly behind the observations, such as around 1934 and 1971, however we note that some uncertainty in the timescales cannot be excluded. This lag may also be partially caused by the local increase in production due to low-energy solar particles during the descending limb of the solar cycle (Koch and Mann, 1996).

The data for South Pole are characterized by a somewhat different set of features than those at Dye 3 and Taylor Dome, perhaps most notable of which is the lower number of observations. As a result, the 11-year solar cycle is obscured at South Pole compared with the data at the other two locations. The downward trend in the simulated South Pole ^{10}Be is stronger than in the observed values, however for the most part the observations fall within the maximum/minimum envelope of the model results. The main exception to this is the large peak in the observations corresponding to the solar minimum around 1977. This feature is also quite pronounced in the Taylor Dome observations but less so at Dye 3, suggesting that anomalous regional weather conditions (for instance, low snowfall over Antarctica, but average conditions over Greenland) might have played a role at this and other points in the ice-core record.

As mentioned earlier, we have focused our discussion on ^{10}Be snow concentration since these are the values directly measured from the ice cores. While it is also possible to discuss ^{10}Be changes in terms of total deposition, this approach is not necessarily advantageous since it requires making estimates of the accumulations rates in the different ice cores and introduces added uncertainties. Furthermore, even if the accumulation rates could be estimated accurately, that does not ensure that the resulting ^{10}Be deposition rate data provide a better indication of solar-related production changes, since ^{10}Be deposition, like snow concentrations, can also be influenced by climate-related factors (Field et al., 2006; Alley et al., 1995). With that in mind, we show modeled snow accumulation and ^{10}Be deposition values in figures 4.5 and 4.6, to provide a qualitative idea of how these processes impact the simulated snow concentration values. Figure 4.6 show downward trends in ^{10}Be deposition that are very similar over time at all three locations, in keeping with the applied ϕ forcing shown in figure 4.1. The alternating high and low values in the deposition data also correspond respectively with the low and high ϕ values associated with the 11-year sunspot cycle.

However, trends in snow accumulation rates vary from site to site (figure 4.5). At Dye 3, the downward trend in ^{10}Be snow concentration is largely caused by the downward trend in ^{10}Be deposition, despite variable accumulation rates. Accumulation plays a more significant role at Taylor Dome, where ^{10}Be snow concentration values more closely resemble the accumulation rate timeseries. At South Pole, Mosley-Thompson et al. (1999) observed increases in snow accumulation from between 1965 and 1999. In the modeled South Pole data, there is a century-long upward trend in accumulation (approximately a 20% increase between 1900 and 2000), and also a downward trend in ^{10}Be deposition, both of which contribute to the negative trend in ^{10}Be snow concentration at that location.

Since the observations at the three locations vary substantially in terms of time resolution, we wanted to get an idea of the timescales on which we might expect them to correlate. For each ensemble member we correlated the ^{10}Be snow concentration time-

Table 4.1: Average ^{10}Be snow concentrations $\pm$ 1 standard deviation. Modeled values are ensemble averages. Units are 10^4 atoms/g water. Note: the estimates of the standard deviations are relative to the different time resolutions for the three data sets; the standard deviations for the modeled data also take these resolution differences into account.

	Dye 3	Taylor Dome	South Pole
observations	$.79 \pm .15$	$1.77 \pm .48$	$3.36 \pm .42$
all forcings	$1.25 \pm .19$	$2.55 \pm .34$	11.34 ± 1.36
SST forcing only	$1.19 \pm .18$	$2.51 \pm .33$	11.24 ± 1.57

series between locations; we then smoothed the records with a 3-point binomial filter and correlated them a second time; then we repeated the process and correlated them a third time. Taylor Dome and South Pole were the only pair of locations for which all ensemble members were significantly correlated without smoothing, implying that relative proximity between ice cores leads to better correlation. For Dye 3/Taylor Dome and Dye3/South Pole, the high correlation values for some ensemble members do increase when successive filters are applied. However, for these multidecadal timescales, we do not see a notable increase in the significance of the correlation for the lower values as a result of smoothing (or successive smoothing). We take this to indicate that smoothing does not necessarily lead to a considerable improvement in the correlation of snow concentration records from different locations, at least over the course of the 20th century.

Table 4.2: Normalized minimum and maximum ^{10}Be snow concentrations over the 20th century. Modeled values show the minimum and maximum values for the ensemble with the full set of forcings.

Location	observed min.	observed max.	modeled min.	modeled max.
Dye 3	0.54	1.50	0.49	4.99
Taylor Dome	0.47	1.67	0.68	1.44
South Pole	0.87	1.25	0.75	1.38
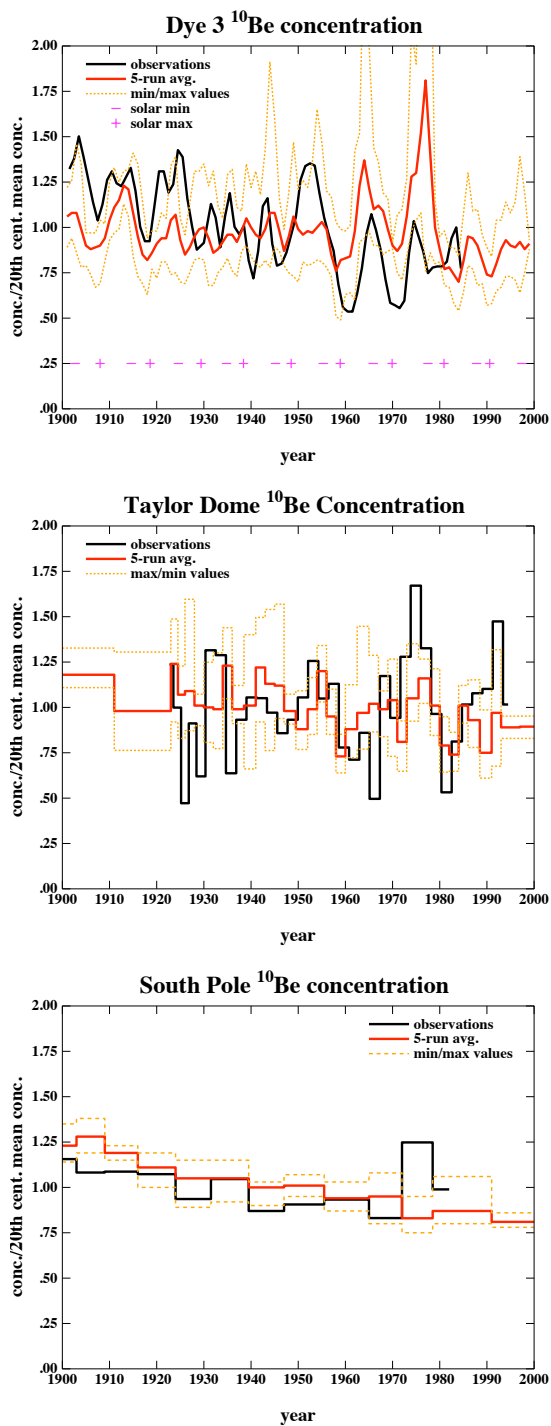
Figure 4.4: Observed ^{10}Be snow concentrations (black line) and the five-run modeled ensemble average concentrations (red line). The dotted orange lines show the minimum and maximum values over time for each ensemble. The minus and plus symbols denote the years of solar minima and maxima respectively, based on international sunspot counts.
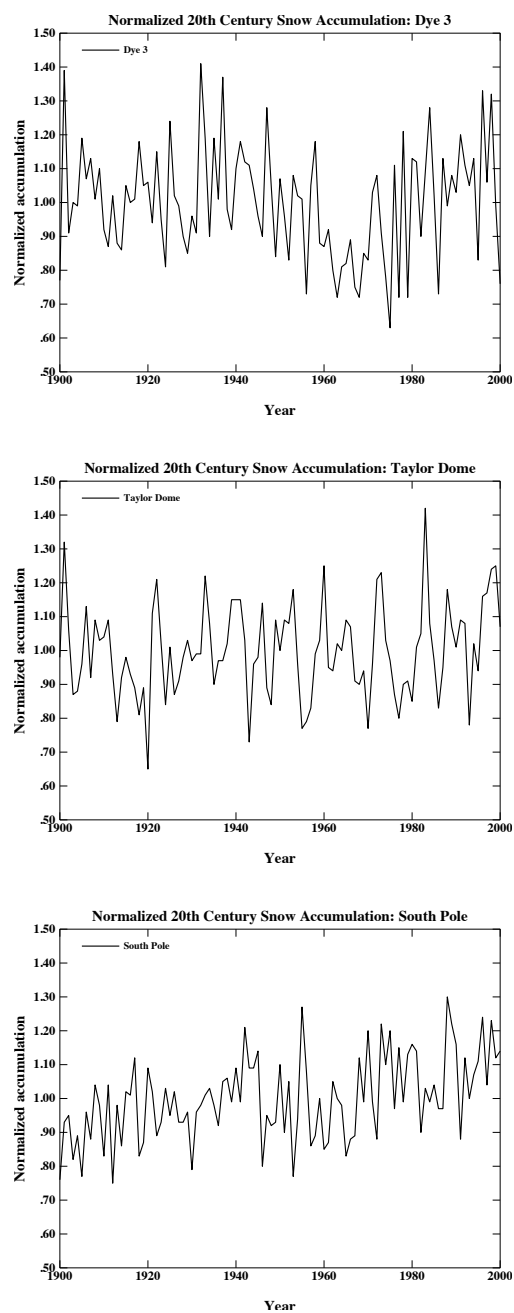
Figure 4.5: Snow accumulation at the three core sites, normalized by the 20th century average value at each location.
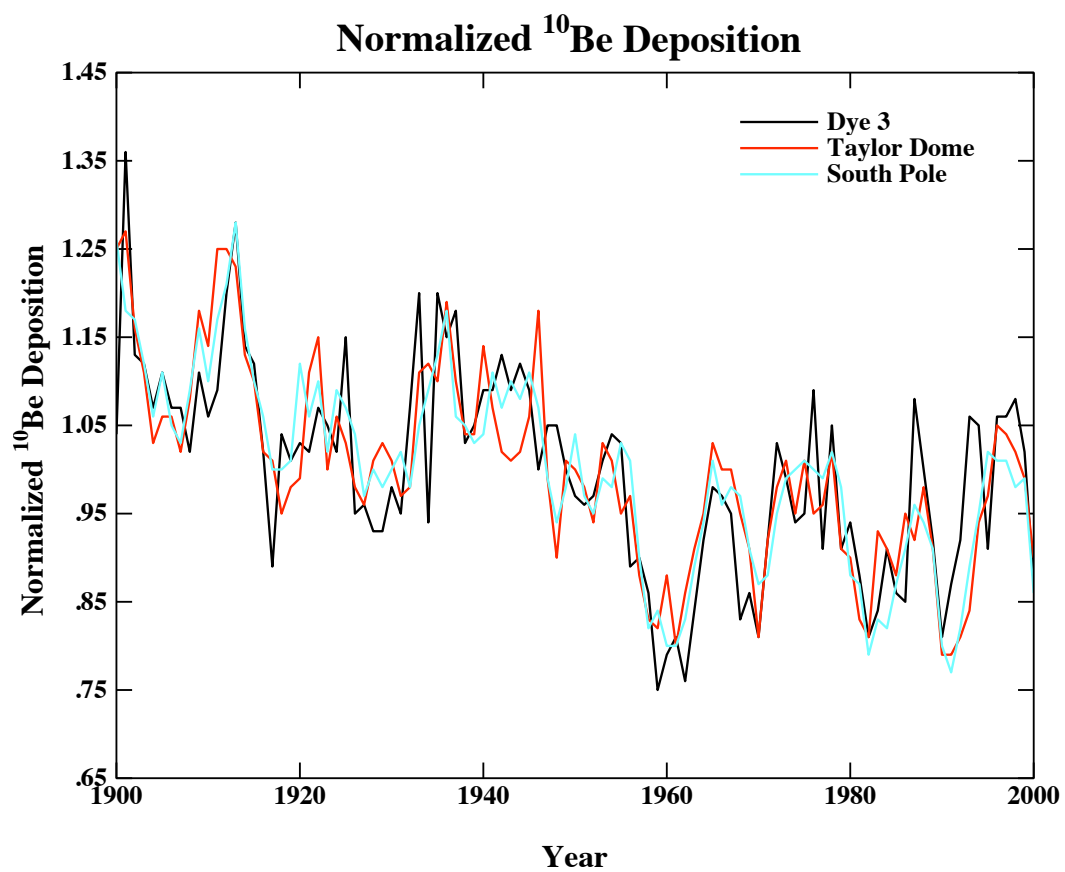
Figure 4.6: Total ^{10}Be deposition, normalized by the 20th century average value at each location.

4.6   Trends in ^{10}Be snow concentration

Figure **??** shows the percent change in snow concentration per decade at the ice-core locations with respect to the 20th century average values. Since the results for both the ensemble with SST forcing only and the ensemble with the complete set of forcings are so similar to each other, we combine all ten ensemble members to calculate the average modeled 20th century trends shown in table 4.3. The green circles in figure 4.7 also show the expected percent change in ^{10}Be deposition at each location based on the years covered by the observations. We calculated these expected deposition changes from the trends in ^{10}Be production, which were forced by the ϕ values shown in figure 4.1. Previous work has shown that because of the increased levels of ^{10}Be production at high latitudes, when ϕ is reduced, global average production increases – however a greater increase in ^{10}Be deposition takes place at latitudes higher than 60° (Field et al., 2006). This additional increase in high-latitude deposition is described by the polar enhancement coefficient (PEC) and its value is about 20%. We calculated the trend in 20th century global average ^{10}Be production and multiplied it by the PEC to get the expected high-latitude deposition changes, shown by the green circles. The expected deposition changes at all locations agree with each other statistically, and all three fall within the uncertainties of the observed concentration trends. The expected deposition trends are slightly different due to the differences in time period relevant for each core.

With the exception of two ensemble members at Dye 3, the modeled trends for all runs as well as the average trends at each location are negative, consistent with the changes in ϕ over the course of the century. However the fact that the observed trend at Taylor Dome is positive (though small) indicates the possibility that climate or weather variability can substantially alter the production signal, and also that two records from the same ice sheet can imply different trends in ϕ. (Although given the very large error bars on the trends at Taylor Dome and South Pole, the observed trends at all three locations agree with each

other within two standard deviations.)

The modeled trends at the two Antarctic locations closely resemble each other both in terms of range and magnitude. Half of the trend values at Taylor Dome and all of the values at South Pole are in statistical agreement with their respective observed trends (again, however, the sizeable error bars at these two locations diminishes to some degree the robustness of this agreement). We also looked at the correlation between locations for all ten of the simulated trend values. Although trends at Taylor Dome and South Pole were somewhat more highly correlated with each other than with Dye 3, none of the trends at each site were significantly correlated, implying that much of the variance seen in the model results in figure 4.7 is simply due to internal unforced variability. These characteristics collectively illustrate that century-scale trends in modeled ^{10}Be snow concentration can be systematically different at different locations.

For the more highly sampled Dye 3 record, none of the simulated concentration trend values fall within the error bars for the observations, and all are less negative than the observed trend. Also, the range of the simulated trends at this location is much greater than at Taylor Dome or South Pole. The size of the range of the trends for the modeled Dye 3 data and for the Antarctic locations suggest that, in the model, the impact of internal variability has a larger expression at Dye 3. Although internal variability plays a smaller role at Taylor Dome and South Pole, the concentration trends for the individual ensemble members at those locations can vary by up to approximately 50% from the mean value.

At least some if not most of the modeled trend values agree with the expected deposition trends at each location – however at Dye 3, the average concentration trend is notably more positive than the expected production trend. Since climate change and production change are the only two factors affecting ^{10}Be snow concentration in these experiments (once weather is averaged out), we can infer that the difference between the mean modeled concentration trends and the expected production-related trend is caused by climate change. Figure 4.7 therefore shows that modeled climate effects at Dye 3 minimize the an-

Table 4.3: Average modeled trends in ^{10}Be snow concentrations $\pm$ 1 standard deviation. Modeled values are averaged over both the runs with all forcing and the runs with SST forcing only. Units are in percent change per decade with respect to the 20th century average value.

Data	Dye 3	Taylor Dome	South Pole
Years	1900-1984	1922-1994	1906-1982
observations	-4.87 $\pm$ 1.33	4.04 $\pm$ 7.58	-2.82 $\pm$ 11.61
model	-0.82 $\pm$ 1.42	-3.56 $\pm$ 1.42	-4.55 $\pm$ 1.03
expected change from production alone	-3.87 $\pm$ 0.91	-3.40 $\pm$ 0.75	-3.97 $\pm$ 1.12

ticipated production change signal. As for Taylor Dome and South Pole, the greater overlap between the closely clustered trend values at these locations and their respective predicted deposition changes implies that modeled ^{10}Be snow concentrations at these locations are perhaps better proxies for changes in ϕ.
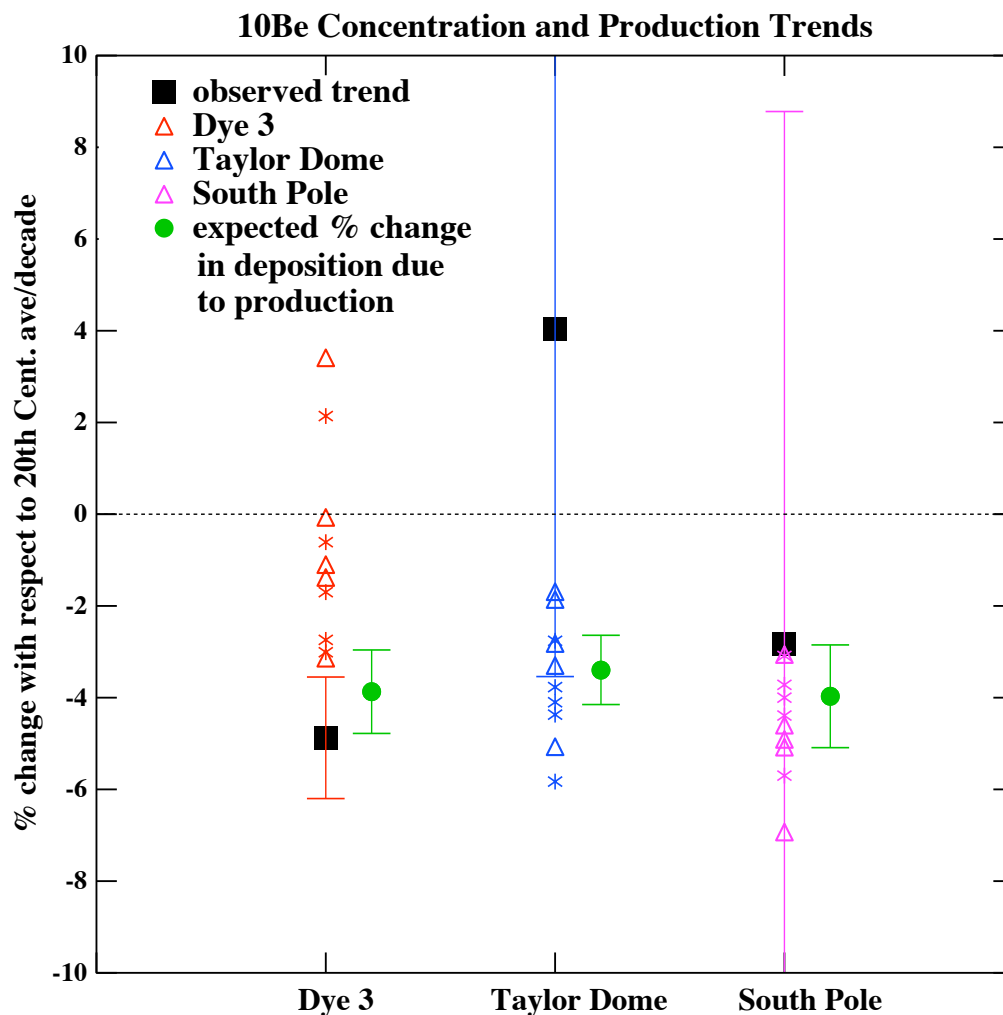
Figure 4.7: Trends in 20th century ^{10}Be snow concentration and production. Black squares show the trend in the observed ^{10}Be concentrations (data: Beer et al. (1990) for Dye 3; Steig et al. (1996) for Taylor Dome; Raisbeck et al. (1990) for South Pole.) The colored triangles (ensemble members with all forcings) and stars (ensemble members with SST forcing only) show the trends in modeled ^{10}Be concentration. The green circles show the expected percent change in total ^{10}Be deposition at each location based on the changes in ^{10}Be production (ϕ) and the expected polar enhancement. All confidence intervals cover two standard deviations.

4.7 Conclusions

We have shown that on interannual and decadal timescales, the relative variability of beryllium isotopes simulated with the GISS ModelE GCM agrees well with changes in observed surface air concentrations, despite the low bias of the modeled [7]Be in surface air with respect to the observations.

In comparison with the [10]Be ice-core records, the model is generally successful at simulating [10]Be snow concentrations over time. It is somewhat more difficult to evaluate how well the model performs at South Pole because of the large sampling interval in the data and the poorly simulated accumulation rates. Improved time resolution in the [10]Be record at this location would be especially helpful in making further analysis. That being said, in terms of agreement between snow concentrations from different core sites, the model results suggest that during the 20th century geographical closeness seems to have a greater impact on correlation than does the use of smoothing functions, or successive smoothing.

At Taylor Dome, the observations show that it is possible to get local trends in 20th century [10]Be concentration that are different from the trends suggested by changes in production, based on the relatively well-constrained inferred ϕ values.

The low levels of correlation between the modeled concentration trends at different locations suggest that internal unforced variability is the main cause for the differences in snow concentration trends from location to location. While internal variability affects all three locations, the relatively narrow range of modeled concentration trends at Taylor Dome and South Pole – and the good agreement between their concentration trends and the corresponding ϕ changes – suggest that, in the model at least, Antarctic locations are more accurate proxies for changes in cosmogenic isotope production on multidecadal timescales during the 20th century. The relatively broad range of simulated concentration trends at Dye 3 shows that climate changes at this site make it possible to get modeled trends in 20th century [10]Be snow concentration that are notably smaller in magnitude than what

one would expect based on the applied changes in ϕ. However the fact that the observed concentration trend at Dye 3 is actually more negative than the production trend suggests that there are shortcomings in the way the model simulates ^{10}Be over southern Greenland, and perhaps over broader areas of the Greenland ice sheet as well. Since the 20th century climate forcings used here are relatively well constrained, it is more likely that the problem lies with the model itself. Future work with higher spatial resolution and improved model physics will allow us to further investigate these issues.

Note: The simulated cosmogenic isotope data used in this article can be downloaded from www.giss.nasa.gov.

CHAPTER 5

SHORT TERM PRODUCTION AND SYNOPTIC INFLUENCES ON ATMOSPHERIC [7]BE CONCENTRATIONS

Authors: Ilya Usoskin, Christy Veeder, Gavin A. Schmidt, Ari-Pekka Leppänen, Ala Aldahan, Gennady A. Kovaltsov, Göran Possnert, and R. Kurt Ungar

5.1 Abstract

Variations of the cosmogenic radionuclide [7]Be in the global atmosphere are driven by co-operation of processes of its production, air transports and removal. We use a combination of the Goddard Institute for Space Studies ModelE and the OuluCRAC:7Be production model to simulate the variations in the [7]Be concentration in the atmosphere for the period from 1st January to 28th February 2005. This period features significant synoptic variability at multiple monitoring stations around the globe, and spans an extreme solar energetic particle (SEP) event that occurred on January 20. Using nudging from observed horizontal winds, the model correctly reproduces the overall level of the measured [7]Be concentration near ground and a great deal of the synoptic variability at timescales of 4 days and longer. This verifies the combined model of production and transport of the [7]Be radionuclide in the atmosphere. The impact of an extreme SEP event on January 2005 is seen dramatically in polar stratospheric [7]Be concentration but is small near the surface (about 2%) and indistinguishable given the amount of intrinsic variability and the uncertainties of the surface observations.

5.2 Introduction

As modern atmospheric air transport models achieve higher level of sophistication, their testing and evaluation becomes increasingly important (see, e.g., Sect. 8.1.2 of IPCC, 2007). Testing of air transport models can be done by measuring the concentration of tracing substances with known sources and comparing them with model predictions. Atmospheric dynamics in the troposphere can be tested in this way using anthropogenic (radioactive, e.g. the Chernobyl accident, or chemical) or natural (e.g., volcanic eruptions) traceable pollutant emissions. The tracing method is more difficult to apply for the stratosphere (e.g., Rind et al., 1999). Here we present a new quantitative method to probe the atmospheric dynamics using the short-lived cosmogenic isotope ^{7}Be as a tracer of air mass. Since it is produced mainly at mid- and high latitudes and mostly in the stratosphere, this tracer is useful for looking at stratosphere-troposphere exchange and also for horizontal transport, and it can also be used as a tracer for aerosol removal processes. The potential usefulness of this cosmogenic tracer was first highlighted long time ago (e.g., Lal and Peters, 1962; Raisbeck et al., 1981; Koch and Rind, 1998) but now its potential can be explored to much greater extent. The method of cosmogenic tracers is applicable for all locations and times, particularly at high latitudes (Koch and Rind, 1998; Aldahan et al., 2001; Jordan et al., 2003; Koch et al., 2006).

Cosmic rays, which are highly energetic nucleons (mostly protons and α particles) of extra-terrestrial origin, continuously bombard the Earth's atmosphere, resulting in various physical and chemical effects (see, e.g., Dorman, 2004). In particular, quite a number of different radioactive isotopes are produced as a byproduct of nucleonic-electromagnetic cascades initiated by cosmic rays in the atmosphere. One of them is the short-lived radionuclide ^{7}Be (half-life $T_{1/2} \approx 53.22$ days), which is a product of spallation of atmospheric O and N nuclei caused by the nucleonic component of the cosmic ray-induced atmospheric cascade. An important advantage of this nuclide is that its concentration in the ambient

air is easy to measure (see Sect. 5.3.1). Accordingly, data on routine ^{7}Be measurements near the ground (typically with weekly resolution) have been performed at different stations around the world for the last several decades, in the framework of radiation safety monitoring and emergency preparedness. It is important to note that cosmic rays are the only natural source of the isotope in the absence of anthropogenic nuclear accidents whose detection is the main purpose of the world-wide monitoring. Atoms of ^{7}Be become quickly attached to atmospheric aerosols, picked up by air masses and thus can trace them. The isotope's life-time is, on the one hand, long enough to allow for long-distance transport (both horizontally and vertically), and on the other hand short enough to prevent long-term accumulation of the isotope in large reservoirs (which would lead to a complicated global cycle). Accordingly, the isotope's transport is quite straightforward and provides a good opportunity to examine the dynamics of air masses on the time scale of days to months (e.g., Koch et al., 1996; Liu et al., 2001; Jordan et al., 2003; Yoshimori, 2005a; Kulan et al., 2006). However, insufficient knowledge of the details about the isotope's production and transport, in particular the lack of a quantitative reliable production model, had limited earlier works to correlative studies and use of the isotopic ratio ^{7}Be/^{10}Be. An appropriate model with special emphasis on the production of ^{7}Be by cosmic rays in the atmosphere has recently been developed: the OuluCRAC:7Be (Cosmic Ray induced Atmospheric Cascade) model (Usoskin and Kovaltsov, 2008). This model makes it possible to numerically simulate the full details of the isotope's production in the low and middle atmosphere. Now, the output of the 3D (geographical coordinates, altitude) and time ^{7}Be production model can be used as an input for an atmospheric circulation model, which can predict the expected concentration of ^{7}Be in air at any location and time. These predicted concentrations can be directly compared with the isotope measurements performed regularly in different sites around the world.

While galactic cosmic rays (GCR) are always present in the Earth's environment, additional sporadic fluxes of solar energetic particles (SEP) can occur due to solar eruptive

phenomena (solar flares or coronal mass ejections), leading to transient changes in the ^{7}Be production. A severe SEP event, one of the strongest ever observed (Plainaki et al., 2007), occurred during the period under investigation, on January 20, 2005 leading also to an observable atmospheric response (Mironova et al., 2008). According to the model computations (Usoskin and Kovaltsov, 2008), production of ^{7}Be was greatly enhanced in polar/sub-polar regions (geomagnetic latitude above $60°$) in the entire atmospheric column during that day without any significant effect in the following days. Therefore, a strong instantaneous "injection" of ^{7}Be trace atoms took place in a limited geographical area leading to a potentially observable effect in the measured ^{7}Be concentration.

In this paper we perform such a comparison using the OuluCRAC:7Be model of ^{7}Be production, the Goddard Institute for Space Studies (GISS) ModelE atmospheric general circulation model (GCM) (Schmidt et al., 2006) and a series of daily measurements of the ^{7}Be concentration in near-surface air at different sites. For the detailed analysis we have chosen the period of January-February 2005, which includes the SEP event mentioned above. The studied period corresponds to the middle of boreal winter/austral summer. Six ^{7}Be monitoring stations in the Northern hemisphere and five in the Southern hemisphere (see Table 5.1), ranging from the tropics to the polar region, provided daily data during the period under investigation.

5.3   Models and data

5.3.1   Measurement

The ^{7}Be measurements used here have been collected by sampling stations of the International Monitoring System (IMS) of the Comprehensive Nuclear Test Ban Treaty Organization (CTBTO). Additionally one station (HEL) from the Finnish national radiation monitoring system was used. The experimental data from the IMS are collected by the

Table 5.1: ^{7}Be measuring sites used in this study

Code	Location	Coordinates
	Northern hemisphere	
SEP63	Stockholm (Sweden)	59.38°N 17.95°E
HEL	Helsinki (Finland)	60.21°N 25.05°E
CAP15	Resolute (Canada)	74.71°N 95.0°W
CAP16	Yellowknife (Canda)	62.47°N 114.47°W
DEP33	Freiburg* (Germany)	47.9°N 7.9°E
USP72	Melbourne (Florida, U.S.A.)	28.1°N 80.6°W
	Southern hemisphere	
AUP04	Melbourne (Australia)	37.7°S 145.1°E
AUP09	Darwin (Australia)	12.43°S 130.9°E
AUP10	Perth (Australia)	31.9°S 116.0°E
NZP46	Chatham Island (New Zealand)	43.82°S 176.5°W
NZP47	Kaitaia (New Zealand)	35.07°S 173.3°E

* Elevation 1208 m a.s.l.

CTBTO in an international data center in Vienna, Austria (Bratt, 2001). All the participating national organizations have access, via national data centers, to the raw measurement data recorded at every other station around the world. The IMS data used in this study has been obtained via the Finnish national data centre (FiNDC) at the Finnish Radiation and Nuclear Safety Authority (STUK). FiNDC and the Finnish radiation monitoring system analyzes the data using Unisampo and Shaman software in almost identical automated analysis pipelines, feeding LINSSI (Linux System for Spectral Information) databases (Ungar et al., 2007; Aarnio et al., 2008; Ala-Heikkilä, 2008). Every measured spectra in the

LINSSI database is analyzed in the same way thus ensuring that the analysis method does not cause any uncertainty between the results from different stations. The only station-to-station uncertainty in the final results comes from sampling and measurement procedure. For all the data used in this study, the necessary permissions to use the data have been obtained from the corresponding national authorities in the countries hosting the IMS stations.

The concentration of ^{7}Be is measured in aerosol samples routinely collected at each station, using a high volume collector. Aerosols are captured by microfiber glass filters (pore size 1–2 μm) with very high retention capability (about 98% of the aerosol particles are captured). While the type and manufacturer of the sampler may vary between individual stations, they all fulfill the same basic requirements necessary for each station (Mathews and Schulze, 2001; Medici, 2001). During the collection of the sample, air is pumped through a fiberglass filter where the aerosols are captured. The sampling volumes may vary between 15,000 and 25,000 m^3 of air per collected sample. The air volume is measured with a flange and pressure gauges where measured air volume is affected by air pressure and moisture. The requirement for air volume uncertainty for the CTBTO IMS stations is $\pm$5 % (Medici, 2001). The uncertainty varies between station types, e.g. the uncertainty of air volume measurement at HEL station is $\pm$2.5 % [Lehtinen J., Senya Oy, personal communication, 2008]. The sampling cycle is divided into three periods – collection, cooling down and measurement, with each period lasting 24 hours. The measurements of ^{7}Be concentration are performed by means of the $\gamma-$ray spectroscopy of the collected samples. The spectrum contains a strong line at 477.59 keV, corresponding to the decay of ^{7}Be. The photo efficiency of the line corresponds to the decay rate of ^{7}Be in the sample, and finally the ^{7}Be activity, typically quantified in μBq/m^3, is computed from the intensity of the 477.59 keV line. Measurements are performed with a HPGe detector to obtain a high resolution $\gamma-$ray spectrum. The detectors are calibrated via standard mixed radionuclide solution or by semi-empirical simulations. The systematic uncertainty caused

by the detector calibration is generally around 3%. The measurement geometries, detector types, models and detector efficiencies vary from station to station, and the homogenous quality of data is ensured through inter-comparison measurements. When all the uncertainties are taken into account, the total uncertainty for the measured ^{7}Be concentration is approximately 7-8%.

5.3.2 ^{7}Be production model

The OuluCRAC:7BE model is based on detailed Monte-Carlo simulations, using COR-SIKA (Heck et al., 1998) and FLUKA (Fassò et al., 2001) numerical packages, of the nucleonic-muon-electromagnetic cascade initiated by cosmic rays in the Earth's atmosphere. All the details of the model can be found elsewhere (Usoskin and Kovaltsov, 2008). The 3D×time production rate Q of ^{7}Be in the atmosphere can be computed as a function of the altitude h, geographical longitude λ, latitude ψ, and time t as

$$Q(h, \lambda, \psi, t) = \int_{E_c(\lambda, \psi)}^{\infty} Y(h, E) \cdot S(t, E) \cdot dE, \qquad (5.1)$$

where $Y(h, E)$ is the ^{7}Be yield function at altitude h, provided by the OuluCRAC:7Be model; $S(t, E)$ is the differential energy spectrum of cosmic rays on the Earth's orbit outside the geomagnetosphere; and integration is over the kinetic energy E of primary cosmic rays above the energy E_c corresponding to the local geomagnetic cutoff. The model can deal with both galactic cosmic rays, which are always present in the near-Earth space, and transient SEP events, via applying the appropriate energy spectrum S in the equation. The digital tables of the ^{7}Be yield function are available from Usoskin and Kovaltsov (2008). We used the force-field approximation of the galactic cosmic ray spectrum (see full details in Usoskin et al. (2005)). The solar modulation potential (Usoskin et al., 2005, see http://cosmicrays.oulu.fi/phi) was taken for January and February 2005, and we include the additional ^{7}Be produced as a result of the severe SEP event on January 20, 2005. The spectrum of SEP for the event of January 20, 2005, was taken using the Ellison-Ramaty

spectral form (Ellison and Ramaty, 1985), which is often used as a handy approximation for strong SEP events (e.g. Lockwood et al., 1990; Stoker, 1995). The SEP spectrum is the same as in the previous work (see Fig. 4 in Usoskin and Kovaltsov, 2008), and is obtained by fitting satellite data (Mewaldt, 2006) and ground based neutron monitor measurements. This computed production of ^{7}Be atoms was then used as an input for the atmospheric circulation model. The daily production of ^{7}Be was simulated for all altitudes and all gridboxes as described above using the parameters of the geomagnetic field from the IGRF-10 (10th generation of the International Geomagnetic Reference Field, http://modelweb.gsfc.nasa.gov/magnetos/igrf.html) model for the epoch 2005. An example of altitude profile of ^{7}Be production is shown in Fig. 5.1 for GCR and SEP. One can see that the maximum production of ^{7}Be due to GCR corresponds to the altitude of 12–15 km. Contribution from SEP becomes important at higher altitudes because of their greater flux but softer energy spectrum.

Since we are primarily interested in the near-ground ^{7}Be concentration measurements, we consider primary particles with energy above 50 MeV/nucleon.

5.3.3 Atmospheric general circulation model

Our simulations of the air mass transport were performed using the latest stratospheric version of GISS ModelE (Schmidt et al., 2006). The model top is at 0.002 mb atmospheric pressure, which is important for capturing the full range of stratospheric ^{7}Be production and also for providing a realistic depiction of transport between the stratosphere and the troposphere (Rind et al., 1999, 2007; Shindell et al., 2006). Previous studies with ModelE have demonstrated its skill in simulating a variety of climatological features, and also in realistically simulating ^{7}Be (Koch et al., 2006; Field et al., 2006; Schmidt et al., 2006). We also note that the ^{7}Be production scheme used in these simulation, which allows for daily varying production and radioactive decay, is slightly improved with respect to our earlier

model (Field et al., 2006) in terms of how the production is partitioned over the vertical pressure levels. Local pressure variations can change the distribution with height of the ^{7}Be production: when local surface pressure is higher (more mass), the ^{7}Be production occurs higher in the column. This was not accounted for in previous versions of the model. However, it makes only a minor difference to the tropospheric ^{7}Be concentrations since they are dominated by advection and mixing rather than by local production. Note that the decay of ^{7}Be is straightforwardly accounted in the model and the 53-day half-life is considerably longer than the weekly and monthly timeseries against which we compare our model output, therefore it does not affect our results.

When simulating the ^{7}Be transport, we assume that there are always sufficient sulfate aerosols available to scavenge the ^{7}Be atoms, and that ^{7}Be attaches to sulfate aerosols immediately after production. We also assume that the sulfate aerosols are 100% soluble. The simulated ^{7}Be is subject to all the advection, mixing and convection processes consistent with the model air mass fluxes. In stratiform and convective clouds, aerosol species are transported and handled according to processes for each cloud type. Aerosol gravitational settling is also included, and fine aerosols are allowed to settle faster in the stratosphere, where the mean free path exceeds the particle radius (Koch and Rind, 1998). The same turbulent exchange coefficients as those used for the model humidity are applied to ^{7}Be near the surface. The resistance-in-series scheme described in Wesely and Hicks (1977) (derived from the Harvard GISS chemical transport model, e.g. Chin et al. (1996)) is the basis for the model's dry deposition scheme. This scheme is fully coupled to the GCM processes and incorporates the GCM-assumed leaf area indices, surface types, radiation, boundary layer height and Monin-Obhukov length (Koch et al., 2006).

Since the SEP event took place on January 20, we ran the simulations from January, 1, through February 27, 2005, in order to capture the effects of the production spike in the weeks that followed. To simulate the conditions in January and February 2005 as realistically as possible, we used a present-day atmospheric composition and forced the model

with observed sea surface temperatures and sea ice values. Also, we used NCEP/NCAR re-analysis data to "nudge" the model winds so that they more closely resemble the observed values. This is done by relaxing the horizontal wind field toward the horizontal components of the reanalysis data (Bauer et al., 2004). Because the vertical mass flux is calculated as a residual of the horizontal winds, sub-gridscale vertical movements will tend to be smoothed out. Since atmospheric ^{7}Be concentrations increase rapidly with altitude, changes associated with storm systems and other vertical mixing processes can have a significant impact on surface air concentrations. To the extent that the residual vertical motions are realistic, we expect that the ^{7}Be concentrations near the surface will be well modelled. However errors in the reanalysis plus deviations from the input winds due to the model's internal dynamics may lead to departures from the observed situation.

The spin-up to January 1, 2005, was over a 10-year period with 2004 nudged wind conditions so that the ^{7}Be was in full equilibrium. There may therefore be small transients that we are not capturing (such as those that are a function of the solar cycle), but these are small compared to the variations due to advection which are dominant on synoptic timescales.

In order to study in detail the effect of the SEP event, we performed two model runs: a "SEP" and a "no SEP" run. In both runs, ^{7}Be production varied on a daily basis, however the "SEP" run included the SEP-induced spike of ^{7}Be production on January 20, and the "no SEP" run was performed without the spike. The model outputs the computed concentration (in ppmv – parts per million by volume) of ^{7}Be averaged over the grid box and time step. An example of the computed ^{7}Be concentration at the level of 192 mb is shown in Fig. 5.2 for a quiet day of January 12, 2005. In order to match individual data locations and heights, we perform a 3D interpolation of the gridded output.

5.4 Testing the air mass transport

The results of the model computations were compared with the measurements for each site individually (Table 5.1). Most of the analyzed stations are located at low altitude, and we use the model results for the atmospheric layer with the pressure boundary of 984 mb, corresponding to about 250 m a.s.l. for the standard atmosphere. The only station situated at higher altitude is DEP33 Freiburg (1208 m a.s.l. - see Table 5.1), for which we used results for the atmospheric layer with the 884 mb pressure boundary. For the purpose of explicit comparison, all the measured data, given originally in μBq/m^3, have been straightforwardly ($1\,\mu$Bq/m^3 $= 2.49825 \times 10^{-19}$ ppmv) translated into the units of ppmv, output by the model. We emphasize that the model results were considered exactly as yielded by the model, without any adjustment or normalization. Therefore, we compare not only the relative variations but also the absolute values of the isotope's concentration in the ambient air.

Comparison between the measured and modeled ^{7}Be concentrations is shown in Figs. 5.3 and 5.4 for all the selected sites. First we check the results for the winter conditions (Northern hemisphere). Agreement between the model and actual measurements of ^{7}Be concentration is very good for the Stockholm station (Panel SEP63 in Fig. 5.3). The absolute value of the modeled concentration matches well with that obtained from measurements, including a relatively low level of 2–4$\times 10^{-16}$ ppmv in January and an enhancement towards late February. The main temporal features are also well reproduced: The major peak of concentration ca. day 38 is precisely reproduced by the model; another peak ca. day 26 is reproduced qualitatively, but the model overestimates its level. A small observed peak ca. day 14 is not reproduced by the model, which instead yields a short peak at day 8, absent in the real data; the oscillatory pattern between days 42 and 59 is fairly well reproduced. Measurements at the Helsinki station (Panel HEL) are also well reproduced by the model. The baseline of the modeled concentration follows nearly

perfectly that of the actual data, except for a period ca. day 26, when a peak (similar to that at the SEP63 station) is predicted by the model but is absent in the data. The major peak ca. day 39 is perfectly modeled. We note that the large enhancement of the ^{7}Be concentration in the Fennoscandic region (sites SEP63 and HEL) ca. day 38–39 was related to a large-scale process of intrusion and lowering of a continental air mass rich in ^{7}Be. The ^{7}Be concentration at the two Canadian sites (CAP15 and CAP16) was relatively stable during the studied period, without distinct peaks. While the overall levels and their slow variations are well reproduced by the model (nearly perfectly for the CAP15 site and reasonably well for the CAP16 site), the variations on the daily scale do not match. Long variations are reasonably well reproduced by the model for the DEP33 site until day 42, when the model and real data begin to diverge. The observed peak ca. day 17 does not appear in the model results. The model reproduces very well the behavior of the ^{7}Be concentration at the USP72 site, including the baseline and a peak ca. day 24. Some spurious peaks appear in the model results in the late part of the analyzed interval.
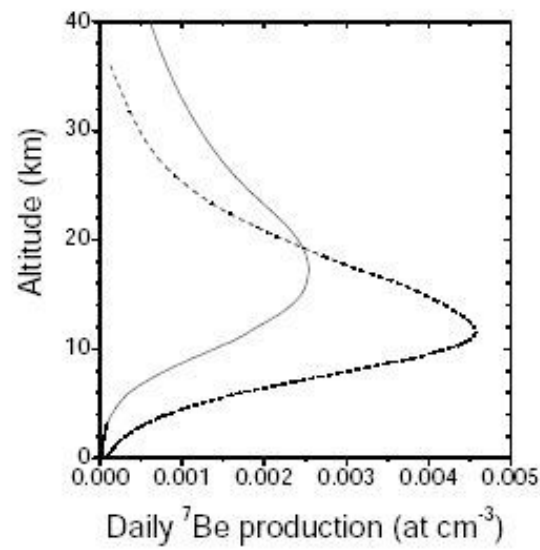
Figure 5.1: Daily production of ^{7}Be in a high-latitude region (P_c=2 GV) as a function of altitude: solid curve – the effect of the SEP event of January 20, 2005; dotted curve – GCR for a quiet day of January 12, 2005.
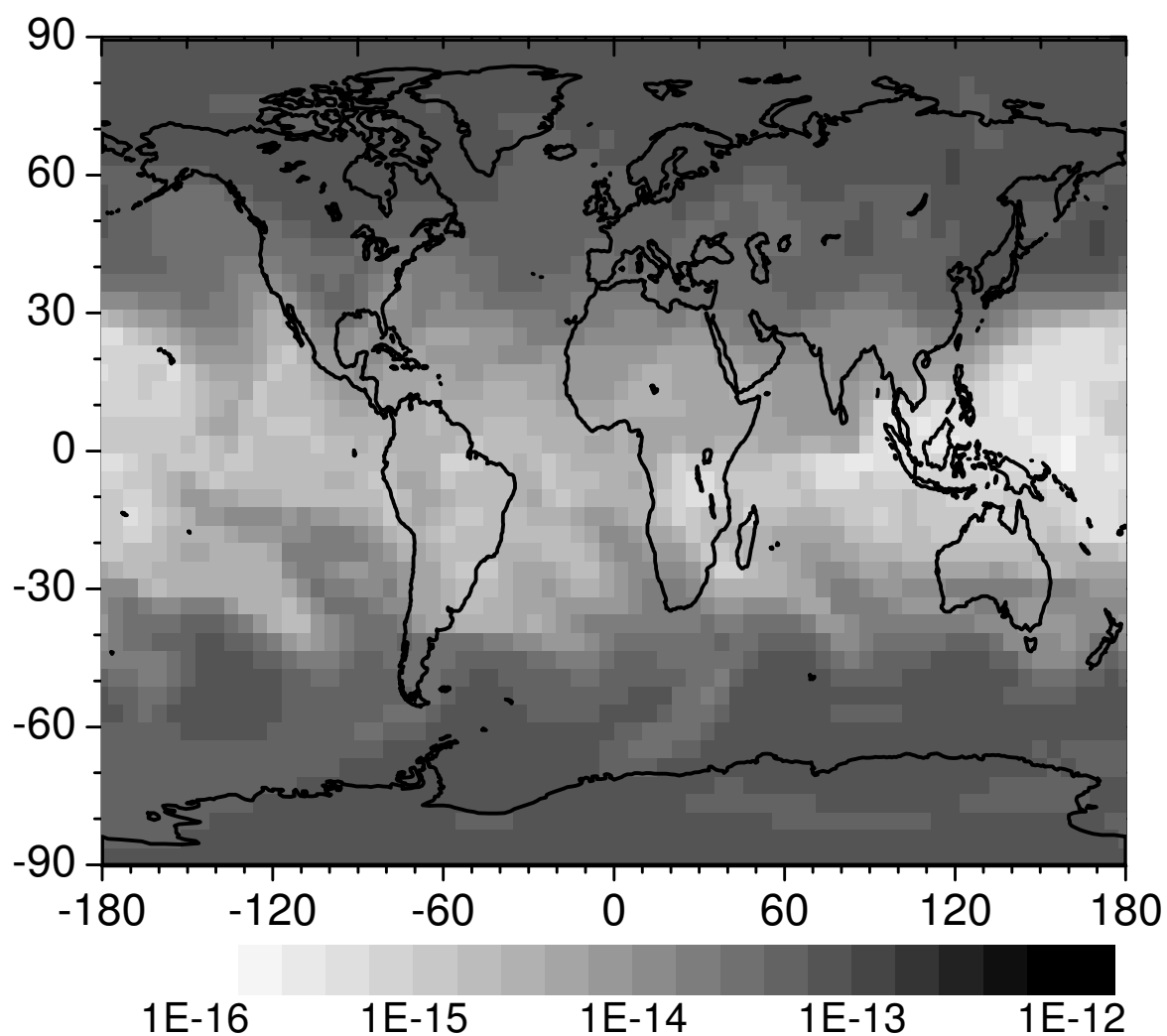
Figure 5.2: An example of the distribution of the computed [7]Be concentration (values in ppmv are given in the bottom grey scale panel) at the atmospheric level of 192 mb for quiet day of January 12, 2005.
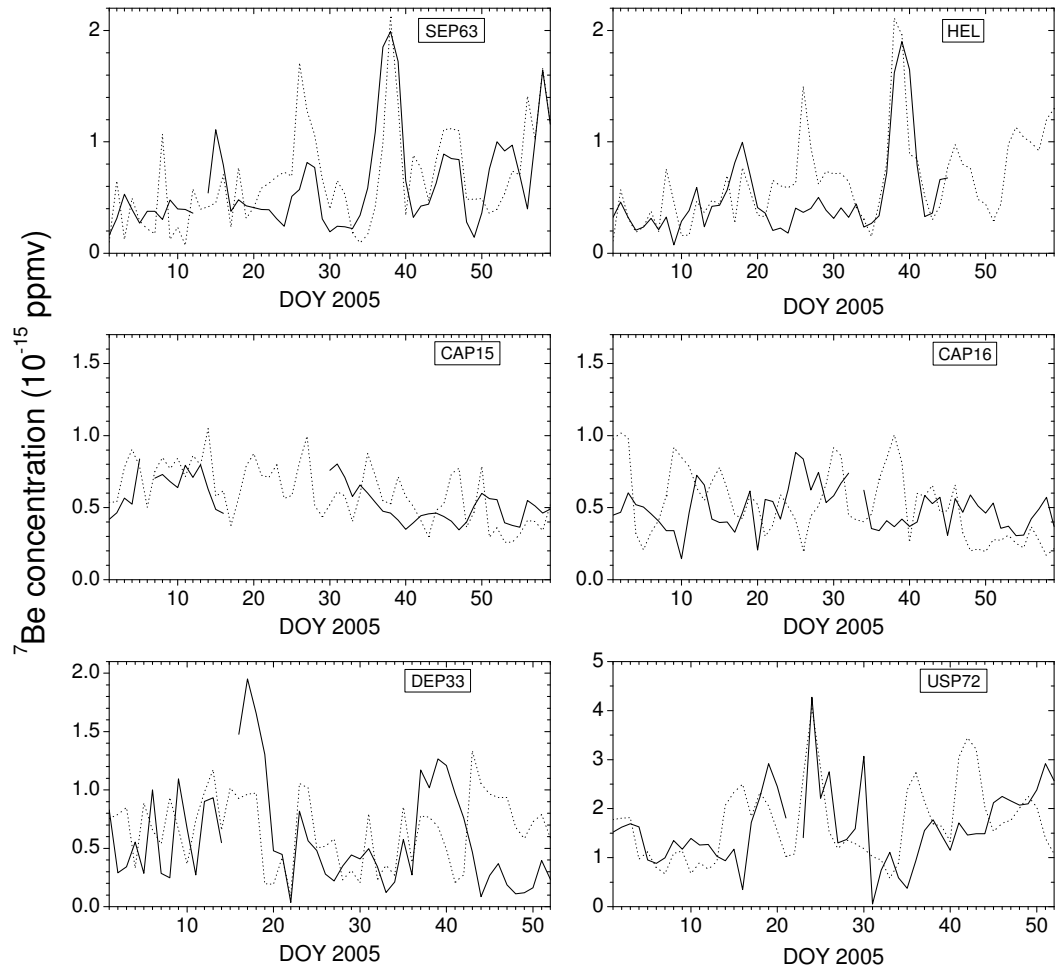
Figure 5.3: Measured (solid curves) and modeled (dotted curves) daily concentration of ^{7}Be in the near-ground air for the beginning of the year 2005. Each panel corresponds to a measuring site (see Table 5.1) in the Northern hemisphere. Concentration is presented in 10^{-15} ppmv (parts per million by volume). Measurements uncertainties (not shown) comprise about 7% (see Sect. 5.3.1).
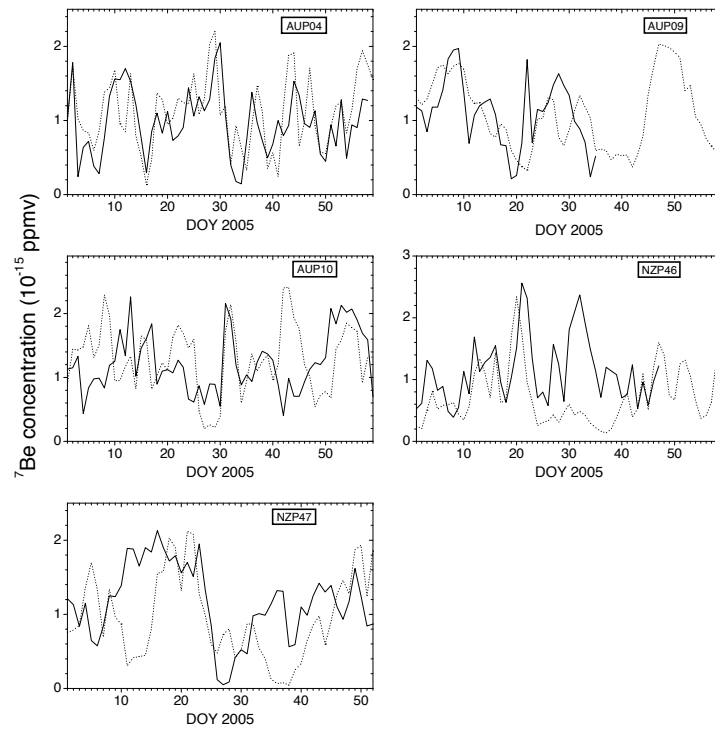
Figure 5.4: The same as Fig. 5.3 but for the Southern hemisphere.

Next we check the results for the mid-summer conditions (Southern hemisphere). The agreement between model and measurements is excellent for the AUP04 site (Fig. 5.4), with all the features being well reproduced by the model. The temporal behavior of [7]Be measured at the AUP09 site is well reproduced in the main pattern (oscillations about 3 weeks in length) but some fine details are missing in the model results. The variations of [7]Be at the AUP10 station is more noisy. While the model reproduces the general pattern, fine details are unevenly resolved: e.g., the peak ca. day 31 is precisely modeled, a similar peak on day 13 is not reproduced. The model also yields a spurious peak ca. day 42. The model precisely reproduces (with maybe a 1-day time inaccuracy) the variations at the site NZP46 before the day 25, but underestimates the isotope's concentration after that. The main pattern at the station NZP47 is captured in general by the model, but the details and the exact timing are only poorly reproduced.

We also analyzed coherence between the measured and modeled concentrations of [7]Be. The coherence can be interpreted as localization of the correlation coefficient in the frequency domain, so that correlation is shown as a function of frequency/period, averaged over the entire time interval. We used the standard magnitude-squared coherence (Kay, 1988), $C_{xy}(f)$, which quantifies (between 0 and 1) the agreement between two series x and y at frequency f:

$$C_{xy}(f) = \frac{|S_{xy}(f)|^2}{S_{xx}(f)S_{yy}(f)} ,$$
(5.2)

where S stands for the power spectral density of either the cross spectrum xy or the individual series x or y. The coherence is shown in Fig. 5.5 for all the selected sites, except the gapped CAP15 and DEP33 series. One can see that short (less than 4 days) variations of the modeled [7]Be concentration are generally not related to the measured fluctuations, as the coherence is low and insignificant. On the other hand, all the analyzed series depict a highly significant coherence at time scales longer than 10 days. Note that, while the absolute value of coherence is high at the time scales above 20 days, the significance may be lower, because of the limited length of the series. The best results are obtained for AUP09,

NZP46, SEP63 and HEL sites, where the variability is adequately modeled already at the 4-day time scale. For such sites as NZP47, AUP10 and CAP16, the model starts significantly reproducing the temporal variations only at a 9 to 10-day scale. Thus, all the analyzed modeled data series reproduce the temporal variability of the measured data with the significance above 90% at time scales longer than approximately a week. This timescale is associated with the synoptic weather systems at these latitudes and is a consequence of the large-scale coherence of the model to the observed sea level pressure patterns.
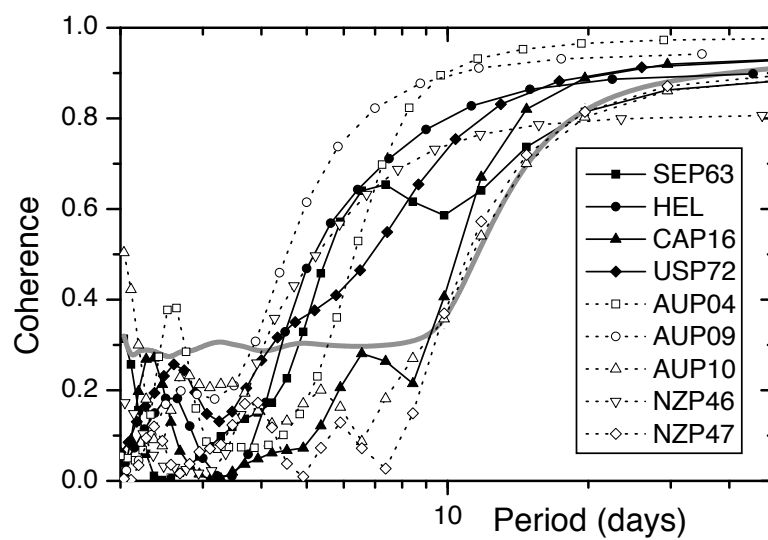
Figure 5.5: Coherence between measured and modeled series of [7]Be concentrations for the sites, as denoted in the Legend. The thick grey curve depicts the 90% confidence level, estimated using the non-parametric random phase test (Ebisuzaki, 1997).

Summarizing this comparison, we can conclude that:

- The model reproduces within about 10% accuracy the overall level of the near-ground ^{7}Be concentration, which varies by an order of magnitude between (sub)polar and tropical sites. The overall level is also correctly reproduced for the mountain site DEP33 (1200 m elevation). This suggest that neither the OuluCRAC:7Be nor the GISS ModelE models make notable errors in the simulations of the ^{7}Be production rate and its large scale transport, or that these diagnostics are not sensitive to such errors.

- The slowly changing (time scales of 4 days and longer) baseline of the ^{7}Be concentration is well reproduced by the model for all the sites in both winter (Northern hemisphere) and summer (Southern hemisphere) conditions.

- Most of the strong peaks in the measured ^{7}Be concentration are well reproduced by the model, in terms of both the timing and amplitude. However, some increases in concentration are not adequately reproduced by the model. The model sometimes yields short spurious peaks, as e.g., ca. day 26 at SEP63 and HEL sites.

We can conclude that, while the model does not resolve all the small scale dynamics in the observed air mass transport, it is pretty good in reproducing the large scale pattern (time scales of 4 days and longer than a week), both qualitatively and quantitatively. While the model's representation of sea level pressure on monthly mean and daily timescales is similar to the observed values, the nudging scheme used in these experiments still creates small discrepancies, with better performance at high- and mid-latitudes than in the tropics. The fidelity of the daily fluctuations in the model are therefore limited by the discrepancies in the sea level pressure fields and the associated patterns in vertical motion. Discrepancies between the modeled and observed ^{7}Be may also be related to the model's inability to resolve small-scale occurrences of stratosphere-troposphere exchange.

5.5   The effect of solar energetic particles

Although the enhanced production of nuclei due to SEPs in the uppermost atmosphere can be directly observed from satellites (Phillips et al., 2001; Share et al., 2002), the effect in the lower atmosphere needs to be studied. In order to resolve the SEP effect, we compare the results of the "SEP" and "no SEP" runs of the ^{7}Be production/transport model, which are identical to each other in all respects except for including/ignoring the additional ^{7}Be production by the SEP event on January 20, 2005 (see Sect. 5.3.3). The effect of the SEP event for every location (λ, ψ), altitude (h) and time (t) is then defined as the normalized excess of the ^{7}Be concentration, calculated by the "SEP" model, C, with respect to that of the "no SEP" model, C_0:

$$R(\lambda, \psi, h, t) = \frac{C(\lambda, \psi, h, t)}{C_0(\lambda, \psi, h, t)} - 1 \,. \tag{5.3}$$

An example of the spatial distribution of the effect of the SEP event is shown in Figs. 5.6 and 5.7 for the altitude of about 12 km (pressure level 192 mb). Panel A shows the SEP effect for the very day of the event and reflects only direct production of the isotope. The enhancement of the ^{7}Be concentration is quite homogeneous (about 7% at this altitude and an order of magnitude greater in the upper stratosphere) and is limited to the geomagnetic latitude above $60°$. Note that this region takes the sigmoid shape because of the tilt of the geomagnetic axis with respect to the geographical axis. A spot of even higher (above 10%) concentration south of Australia corresponds to the southern (geomagnetically northern) magnetic pole and was caused by the highly anisotropic prompt component of the SEP event (Bazilevskaya et al., 2008). Next, panel B in Fig. 5.6 shows the spatial distribution of the effect 11 days later (January, 31). Here both horizontal and vertical transports are important. In the Southern hemisphere with its austral summer, the enhanced (5–6%) concentration occupies all geographical latitudes above $50°$ nearly uniformly with some small plumes extending to $30°$. The situation in the Northern winter hemisphere is more complicated. Because of the intensive air mass transport, the enhanced concentration quickly

advances to subtropical latitudes in the Far East and Pacific regions, but retreated to 50–70° latitude in the North Atlantic region.

Panel C in Fig. 5.7 shows the situation 40 days after the event, when about 40% of the ^{7}Be atoms produced during the event have already decayed. The enhanced concentration (3–4% on average) occupies now all latitudes above $45°$ nearly homogeneously with some signatures of the zonal patterns, particularly in the southern hemisphere.

In summary, the pattern of an SEP event on the ^{7}Be concentration in air is defined by the local production in the very first days after the event, after which it is dominated by the large-scale air mass transport, including vertical transport. Within a month or so, air concentrations are homogenized in the mid-high latitudes (above roughly $45°$ latitude).

We have also analyzed the time and altitude variability of the SEP effect for the high latitude (60–64° N) zonal mean, where the expected effect is high (Fig. 5.8). While the absolute production of ^{7}Be peaks around 15–20 km, the SEP effect starts dominating over the GCR production above 20 km altitude (Fig. 5.1). Accordingly, the immediate SEP effect can be directly observed only in the upper stratosphere. The modelled effect of SEP event is very strong (two orders of magnitude greater than the daily GCR-related production) and instantaneous at the altitude above 50 km. The additionally produced ^{7}Be does not stay at this atmospheric level but moves down as shown in the figure, descending to 40–50 km within a week. After a fortnight there is no indication of the enhanced ^{7}Be concentration at these altitudes.
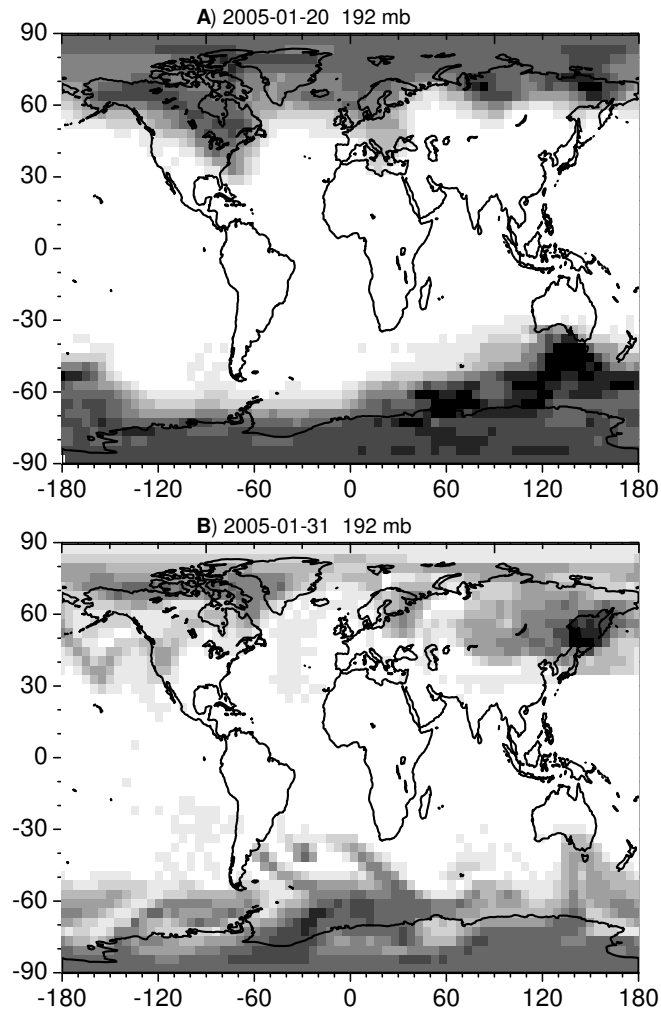
Figure 5.6: Spatial (geographical latitude-longitude) distribution of the computed effect (see text for definition) of SEP event of January 20, 2005, in the ^{7}Be concentration at the atmospheric level of 192 mb (about 12 km altitude). The grey scale in the bottom applies to all the panels. The distribution is shown for days of January, 20 (Panel A), January, 31 (Panel B) and February 27 (Panel C).
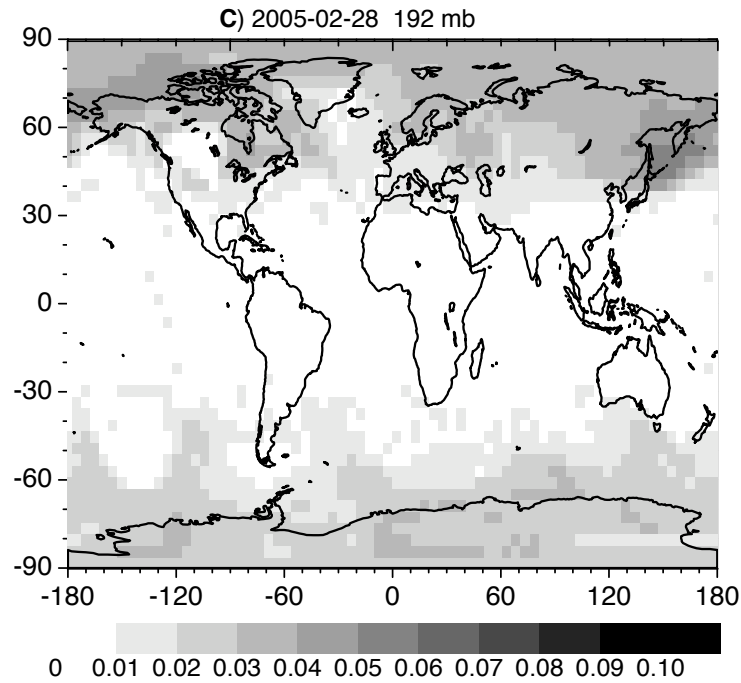
Figure 5.7: Spatial (geographical latitude-longitude) distribution of the computed effect (see text for definition) of SEP event of January 20, 2005, as in fig. 5.6, for February 27 (Panel C).

The ^{7}Be concentration enhanced by an order of magnitude is expected in the middle troposphere (about 25–30 km). While the immediate effect of SEP (on January, 20) was of a factor of 14 at 30 km altitude, the enhanced concentrations stays nearly constant at the level of enhancement by a factor of 10–20 for about a month due to the steady advection of ^{7}Be from upper layers. The effect of the SEP event rapidly decreases with lowering altitude, being factors of 3, 0.25 and 0.07 at about 25 km, 20 km and 14 km, respectively. However, because of the redistribution of the produced isotope (in particular by the vertical motion), the enhanced concentration persists for weeks. The modeled SEP effect is strong enough to be directly observed in the stratosphere, but it is weak in the troposphere, at the level of 2-3%, and is mostly secondary (i.e., due to the downward transport of the additionally produced ^{7}Be), with the direct effect not exceeding 2%, which is smaller than the measurement uncertainties. Some slight enhancements might be expected during a couple of weeks after the event, but these cannot be distinguished over the background variations of several percent (see Sect. 5.3.1).

Summarizing this analysis we can conclude that the instantaneous direct effect of the SEP event is strongest in the upper stratosphere, with concentrations of ^{7}Be increasing by two orders of magnitude due to the enhanced in-site production. In the lower stratosphere and troposphere, the effect is two-fold: a peak of ^{7}Be concentration on the first day is the result of the direct production effect, and enhanced concentration extends for months due to the descent of ^{7}Be produced largely in higher atmospheric layers.

The expected effect (2–3%) of an extreme SEP event, as predicted by the model, is apparently too small to be detected at the near-ground data analyzed here, in agreement with an earlier fragmentary study (Yoshimori, 2005b). Direct measurements in the strato- sphere, where the ^{7}Be concentration is expected to be enhanced by a factor of 2–10 during the weeks following the event, would make it possible to test the model results directly. However, we are not aware of such measurements performed during January or February 2005.
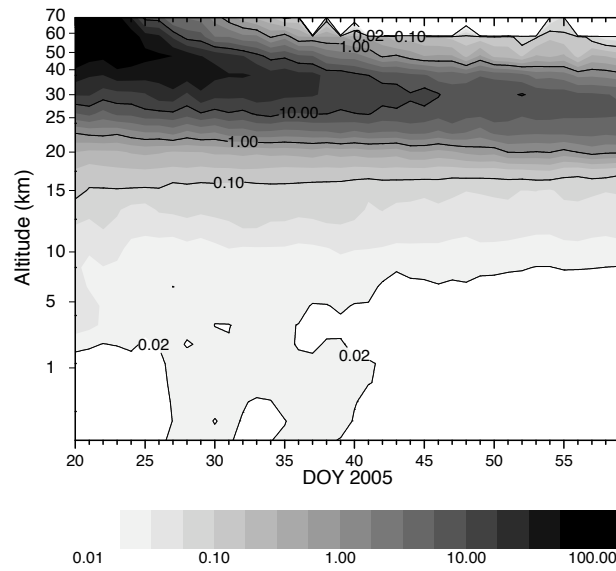
Figure 5.8: Effect (see text for definition) of solar energetic particles from the SEP event of January 20, 2005 on the computed ^{7}Be concentration in the atmosphere in subpolar zonal mean (60–64° N latitude, averaged over all longitudes).

5.6 Discussion and Conclusions

We presented the results of testing of an atmospheric GCM model using the cosmogenic isotope [7]Be as a tracer of air mass transport in the Earth's atmosphere. A combination of a numerical model of [7]Be production and transport has been developed, using the GISS ModelE atmospheric circulation model, where in-situ production of [7]Be by cosmic rays is included explicitly as computed by the OuluCRAC:7Be model. The combined model allows us to trace the air mass transport by means of the [7]Be concentration in full 3D on daily timescales. In order to evaluate the model, its results were directly compared with routine daily measurements of the [7]Be concentration in near-ground air performed by radiation safety authorities in different countries covering the latitudinal range from tropics to polar regions (see Table 5.1). The model reproduces well both the overall level of [7]Be concentration in the near-ground air, which varies by an order of magnitude between different monitoring stations, and also the large scale variations in air concentration, including, e.g., a pronounced peak on February 6–10 in Fennoscandian sites SEP63 and HEL.

We note that while the results of the OuluCRAC:7Be production model are in good agreement with semi-empirical models (Lal and Peters, 1967; Nagai et al., 2000; O'Brien, 1979) and fragmentary in-situ measurements (see Sect. 3 in Usoskin and Kovaltsov (2008)), some numerical models (Masarik and Beer, 1999; Webber et al., 2007) may somewhat underestimate the production as mentioned by Kollár et al. (2000) and Heikkilä et al. (2008). The Monte-Carlo core of the OuluCRAC:7BE model is essentially the same as that of the OuluCRAC:CRII model (Usoskin and Kovaltsov, 2006), which computes the cosmic ray-induced ionization in the atmosphere. The latter has been verified, by comparison with observational data and independent model simulations, to correctly simulate the atmospheric cascade within 10% accuracy (Bazilevskaya et al., 2008; Usoskin et al., 2009), which confirms the correctness of the cascade core simulations by the OuluCRAC model. The overall agreement with measurements obtained here implies that our OuluCRAC:7Be

model correctly simulates the production of ^{7}Be, including the overall normalization.

We also found that our combined model adequately reproduces transport of air masses on large scales (time scales of 4 days or longer). However, details at shorter timescales and on sub-synoptic length scales are unevenly described by the model: while some variations are precisely reproduced (e.g., for the APU04 site), some others are either not reproduced (e.g., a peak ca. January 18 at DEP33 station) or over-reproduced (e.g., a short peak on January 26 at the SEP63 site) by the model. Short-term fluctuations at the diurnal scale are typically not reproduced by the model. This suggests that the combined model simulates correctly the large-scale atmospheric dynamics but does not possess sufficient precision to distinguish small scale effects. This is probably related to the nudging scheme used in these model runs (Sect. 5.3.3). The present comparison is limited to the lowest atmospheric layer, since the routine measurements of ^{7}Be concentration are only performed near the ground. However, since the isotope is mostly produced in the upper atmospheric layers, the present results imply that the model also works correctly for higher altitudes, at least in the troposphere. For that layer, the model succeeds in matching the magnitude of the observed ^{7}Be concentrations, as well as the range of variability and the general trends at the different northern hemisphere and southern hemisphere locations.

We have also studied the effect of a severe solar energetic particle event on ^{7}Be in the atmosphere. The severe SEP event of January 20, 2005, resulted in an instant "injection" of ^{7}Be atoms into the atmosphere. The simulations suggest that the effect of the SEP event on ^{7}Be concentration is two-fold. The instantaneous effect of the enhanced local production due to solar particles is limited to polar regions but occupies the entire atmospheric column, varying from two to three orders of magnitude in the upper stratosphere to a few percent in the lower troposphere. This immediate effect dominates in the upper atmosphere, from where ^{7}Be produced by the SEP event descends to the stratosphere within several days. On the other hand, the enhanced concentration of ^{7}Be in stratosphere and troposphere is prolonged for month(s), mostly because of the downward transport of ^{7}Be

from upper atmospheric layers. The effect of notably enhanced ^{7}Be concentration extends from (geomagnetic) polar regions to occupy the entire mid- and high-latitudes, with a clear zonal structure in the Southern hemisphere (local summer). Unfortunately, the expected effect of the SEP event is too small (about 2%) at the ground level to be securely detected in the measured data. Direct air-borne measurements of ^{7}Be concentration in the upper troposphere or stratosphere, even performed several weeks after a strong SEP event, could provide extremely valuable information for direct tests of air circulation models.

In conclusion, we have developed and directly verified a novel combined model of production and transport of the cosmogenic tracer ^{7}Be in the atmosphere. We have shown that synoptic variations in ^{7}Be can be captured by a nudged GCM including aerosol tracers. Further analysis of the causes of these variations and more detailed studies of stratosphere/troposphere interactions may allow more fundamental tests of the model leading to better understanding of the air mass transport processes.

156

CHAPTER 6

CONCLUSIONS

The experiments discussed in the preceding chapters have examined the influences on the ^{10}Be record from several different angles. In terms of production-related impacts, decreases in geomagnetic field strength and in the solar modulation constant ϕ both result in increased ^{10}Be production, but with distinct differences in latitudinal distribution. The zonal mean changes in ^{10}Be deposition showed a polar enancement coefficient of 1.2 for solar magnetic changes, which may take place on annual to multidecadal timescales, and 0.8 for geomagnetic changes, which are more likely to take place over centennial and millennial timescales.

On shorter timescales, the simulations of January-February 2005 using a daily-varying production function show that solar energetic particle (SEP) events such as the one that took place on January 20, 2005, lead to large increases in stratospheric and mesospheric ^{7}Be air concentrations, and that stratospheric and tropospheric concentrations are enhanced for weeks after as the SEP-produced ^{7}Be is transported downward. However, SEP-related increases in ^{7}Be air concentrations at the surface are only about 2% and therefore too small to be clearly detected amid day-to-day variability. Should tropospheric and stratospheric observations of another SEP event become available sometime in the future, it would be interesting to revisit this project and compare model performance with atmospheric ^{7}Be data.

In looking at climate-related impacts on ^{10}Be, model runs simulating periods of reduced NADW production (the Younger Dryas and the 8.2 kyr event) show increases in ^{10}Be concentration that are about half as large as the observed changes for those time periods. The smaller magnitude of the modeled concentrations in comparison to the ice-core data may be

related to the warmer-than-observed conditions in the modeled climates for those runs. The increased concentrations seen in the model are due both to higher levels of ^{10}Be deposition and decreased accumulation. In the $2xCO_2$ simulation, a slightly different combination of effects takes place: the warmer climate causes increased precipitation over ice sheets, and also leads to higher levels of STE, which would imply that ^{10}Be was being transferred from the regions of its production to the surface at a faster rate. However the higher accumulation rates have the stronger impact, and cause ^{10}Be snow concentrations to decrease by 8-40% over Greenland and Antarctica. Concentration changes related to persistent volcanic eruptions, while also dominated by reduced accumulation, are less consistent and result in 5-15% increases in ^{10}Be snow concentration over parts of central Antarctica, but negligible changes over Greenland.

Overall, the results of the experiments involving climate forcings alone indicate that climate perturbations that are (1) relatively large (such as those caused by sizeable reductions in NADW production), (2) sustained over several decades or longer, and (3) unrelated to changes in ϕ or geomagnetic field strength can lead to notable changes in modeled ^{10}Be snow concentration. The model results also demonstrate that it's possible for the sign of the concentration changes to be consistent with what might be expected had coincident solar irradiance changes taken place – such as in the $2xCO_2$ runs, where the warmer temperatures and reduced ^{10}Be concentrations could appear to be the result of increases in TSI and solar magnetic activity. In order to avoid the mistake of over-attributing ^{10}Be concentration changes to changes in production (and, by extension, changes in TSI), it is therefore important to consider the potential effects of climate, particularly during times of significant climate change.

In order to create a context for understanding how *simultaneous* production changes and climate changes might affect ^{10}Be, I performed experiments to simulate Maunder Minimum-like conditions. The model was forced with a range of TSI changes, volcanic aerosols, and ϕ values to create simulations that captured a range of possible Maunder Min-

imum (MM) climate scenarios. In the runs with TSI changes and production changes, ^{10}Be snow concentration is influenced much more strongly by production changes than by TSI-related climate effects. The addition of volcanic forcing, which is not necessary in order to create realistic MM climate conditions, does not have a notable impact on ^{10}Be over Greenland or Antarctica. Volcanic forcing does however have a variable effect on simulated ^{10}Be snow concentrations at the gridbox level, and presents a possible subject for future study. Finally, I compared the relationship between the ϕ changes used in the experiments, and the resulting ^{10}Be concentration changes, with different estimates of the observed concentration changes during the MM. Taking into account the uncertainties related to the time resolution of the different sets of observations, and the years used as reference periods and averaging periods, our results indicate that over the MM, ϕ values ranged from approximately 280 to 395 MeV, with values as low as 142 MeV during the years with the highest observed ^{10}Be concentrations.

The 20th-century transient simulations address the combined effects of production change and climate change from a different perspective, by looking at how ice-core records from different locations might respond to the combined forcings over time. The model has difficulty simulating high enough accumulation rates at South Pole, however the relative changes in the modeled ^{10}Be concentrations agree fairly well with the observed values. Simulated ^{10}Be concentration trends at Taylor Dome and South Pole agree with each other more closely than at Dye 3, where the trends for the individual ensemble members cover a wider range of values. The greater degree of unforced variability at Dye 3 compared to Taylor Dome and South Pole, as well as the better agreement between the modeled concentration trends at the Antarctic locations and the expected change due to ϕ changes imply that in the model, Antarctic ^{10}Be is likely to be a better proxy for production changes, at least on centennial timescales. While the observed Dye 3 concentration trend agrees with the expected change in deposition due to production, the modeled Dye 3 trend values are all greater than the observed trend, and most of them are higher than the

expected production-related change. These results suggest that there is a strong climate component to the ^{10}Be in southern Greenland and merits more detailed investigation.

Collectively, the results of these experiments indicate that there are a variety of considerations that should be taken into account when interpreting the ^{10}Be record, and the best approach to take will depend significantly on the time period and relevant forcings. When analyzing ^{10}Be snow concentrations, the primary goal is often to make a statement about how ϕ or the geomagnetic field changed during that time. In the most general terms, the results show that on decadal and centennial timescales, ϕ changes are more likely to have a stronger impact on the ^{10}Be record than climate effects. On longer timescales, for which much larger climate forcings are possible, climate-related concentration changes may have an equal or even larger impact on ^{10}Be ice-core records than production changes. It is also possible that, for certain magnitudes of forcing, both production changes and climate changes can have discernible effects on ^{10}Be concentrations, as shown in the 20th-century transient experiments. Caveats apply in all cases, and I have mentioned some possible directions that further modeling studies of ^{10}Be could take. However perhaps even more important at this stage is the need to expand and improve the available observations, and cultivate the analysis and creation of new high-resolution ice-core records.

Bibliography

Aarnio, P. A., J. Ala-Heikkila, A. Isolankila, A. Kuusi, M. Moring, M. Nikkinen, T. Siisko- nen, H. Toivonen, K. Ungar, and W. Zhang (2008). LINSSI: Database for gamma-ray spectrometry. *J. Radioanlyt. Nuc. Chem. 276*, 631–63.

Ala-Heikkilä, J. (2008). *Analysis methods for airborne radioactivity, TKK-DISS-2491*. Helsinki: Helsinki University of Technology.

Aldahan, A., G. Possnert, and I. Vintersved (2001). Atmospheric interactions at northern high latitudes from weekly Be-isotopes in surface air. *Appl. Radiat. Isotopes 54*, 345– 353.

Alley, R. B., R. C. Finkel, K. Nishiizumi, A. Anandakrishnan, C. A. Shuman, G. R. Mer- shon, G. A. Zielinski, and P. A. Mayewski (1995). Changes in continental sea-salt atmo- spheric loadings in central Greenland during the most recent deglaciation: Model based estimates. *J. Glaciol. 41*, 503–514.

Alley, R. B., P. A. Mayewski, T. Sowers, M. Stuiver, K. C. Taylor, and P. U. Clark (1997). Holocene climatic instability: A prominent, widespread event 8200 yr ago. *Geology 25*, 483–486.

Alley, R. B., D. A. Meese, C. A. Shuman, A. J. Gow, K. C. Taylor, P. M. Grootes, J. W. C. White, M. Ram, E. D. Waddington, P. Mayewski, and G. Zielinski (1993). Abrupt in- crease in Greenland snow accumulation at the end of the Younger Dryas event. *Na- ture 362*, 527–529.

Appenzeller, C., T. F. Stocker, and M. Anklin (1998). North Atlantic Oscillation dynamics recorded in Greenland ice cores. *Science 282*, 446–449.

Arthern, R. J., D. P. Winebrenner, and D. G. Vaughan (2006). Antarctic snow accumula- tion mapped using polarization of 4.3-cm wavelength microwave emission. *J. Geophys. Res. 111*, doi:10.1029/2004JD005667.

Barber, D. C., A. Dyke, C. Hillaire-Marcel, A. E. Jennings, J. T. Andrews, M. W. Kerwin, G. Bilodeau, R. McNeely, J. Southons, M. D. Morehead, and J.-M. Gagnon (1999). Forcing of the cold event of 8,200 years ago by castastrophic drainage of Laurentide lakes. *Nature 400*, 344–348.

Bard, E., J. Jouzel, and G. M. Raisbeck (2007). Comment on "Solar activity during the last 1000 yr inferred from radionuclide records" by Muscheler et al. (2007. *Quat. Sci. Rev. 26*, 2301–2304.

Bard, E., G. M. Raisbeck, F. Yiou, and J. Jouzel (1997). Solar modulation of cosmogenic nuclide production over the last millennium: comparison between ^{14}C and ^{10}Be records. *Earth Planet. Sci. Lett. 150*, 453–462.

Bauer, S., Y. Balkanski, M. Schulz, D. Hauglustaine, and F. Dentener (2004). Global modeling of heterogeneous chemistry on mineral aerosol surfaces: Influence on tropospheric ozone chemistry and comparison to observations. *J. Geophys. Res. 109*, D02304.

Bazilevskaya, G. A., I. G. Usoskin, E. O. Flückiger, R. G. Harrison, L. Desorgher, R. Bütikofer, M. B. Krainev, V. S. Makhmutov, Y. I. Stozhkov, A. K. Svirzhevskaya, N. S. Svirzhevsky, and G. A. Kovaltsov (2008, March). Cosmic ray induced ion production in the atmosphere. *Space Sci. Rev. 137*, 149–173.

Beer, J. (1997). Accelerator mass spectrometry: a new tool in environmental sciences. *Nucl. Phys. News 7*, 15–22.

Beer, J. (2000). Neutron monitor records in broader historical context. *Space Sci. Rev. 93*, 107–119.

Beer, J., A. Blinov, G. Bonani, R. C. Finkel, H. J. Hoffman, B. Lehmann, H. Oeschger, A. Sigg, J. Schwander, T. Staffelbach, B. Stauffer, M. Suter, and W. Wölfli (1988). Use of ^{10}Be in polar ice to trace the 11-year cycle of solar activity. *Nature 331*, 675–679.

Beer, J., A. Blinov, G. Bonani, R. C. Finkel, H. J. Hoffman, B. Lehmann, H. Oeschger, A. Sigg, J. Schwander, T. Staffelbach, B. Stauffer, M. Suter, and W. Wölfli (1990). Use of ^{10}Be in polar ice to trace the 11-year cycle of solar activity. *Nature 347*, 164–166.

Beer, J., R. Muscheler, G. Wagner, C. Laj, C. Kissel, P. W. Kubik, and H.-A. Syanl (2002). Cosmogenic nuclides during Isotope Stages 2 and 3. *Quat. Sci. Rev. 21*, 1129–1139.

Beer, J., U. Siegenthaler, G. Bonani, R. C. Finkel, H. Oeschger, M. Suter, and W. Wolfli (1990). Information on past solar activity and geomagnetism from ^{10}Be in the Camp Century ice core. *Nature 347*, 164–166.

Beer, J., U. Siegenthaler, H. Oeschger, M. Andree, G. Bonani, M. Suter, W. Wölfli, R. Finkel, and C. C. Langway (1983). Temporal ^{10}Be Variations. In *Proc. 18th Int. Cosmic Ray Conf.*, pp. 317–320. Bangalore.

Beer, J., S. Tobias, and N. Weiss (1998). An active sun throughout the Maunder minimum. *Solar Physics 181*, 237–249.

Bratt, S. (2001, May). The International Data Centre of the Comprehensive -Nuclear Test Ban Treaty: vision and progress. *Kerntechnik 66*, 134–142.

Briffa, K., T. Osborn, F. Schweingruber, I. Harris, P. Jones, S. Shiyatov, and E. Vaganov (2001). Low frequency temperature variations from a northern tree ring density network. *J. Geophys. Res. 106*, 2929–2941.

Briffa, K. R. (2000). Annual climate variability in the holocene: interpreting the message of ancient trees. *Quat. Sci. Rev. 19*, 87–105.

Broecker, W. S. and G. H. Denton (1990). The role of ocean-atmosphere reorganizations in glacial cycles. *Quat. Sci. Rev. 9*, 305–341.

Bromwich, D. H. (1988). Snowfall in High Southern Latitudes. *Revs. Geophys. 206*, 149–168.

Bromwich, D. H., R. I. Cullather, Q. Chen, and B. M. Csathó (1998). Evaluation of recent precipitation studes for Greenland Ice Sheet. *J. Geophys. Res. 103*, 26,007–26,024.

Brönnimann, S., J. Luterbacher, J. Staehelin, T. Svendby, G. Hansen, and T. Svoe (2004). Extreme climate of the global troposphere and stratosphere in 1940-42 related to El Niño. *Nature 431*, 971–974.

Chin, M., D. J. Jacob, G. M. Gardner, M. S. Foreman-Flower, P. A. Spiro, and D. L. Savoie (1996). A global three-dimensional model of tropospheric sulfate. *J. Geophys. Res. 101*, 18,667–18,690.

Christl, M., C. Strobl, and A. Mangini (2003). Beryllium-10 in deep-sea sediments: a tracer for the Earth's magnetic field intensity during the last 200,000 years. *Quat. Sci. Rev. 22*, 725–739.

Crowley, T. J. (2000). Causes of climate change over the past 1000 years. *Science 289*, 270–277.

Crowley, T. J. and T. S. Lowery (2000). How warm was the medieval warm period? *Ambio 29*, 51–54.

Crowley, T. J., G. Zielinski, B. Vinther, R. Udisti, K. Kreutz, J. Cole-Dai, and E. Castellano (2008). Volcanism and the Little Ice Age. *PAGES 16*, 22–23.

Csathó, B., H. Xu, R. Thomas, D. Bromwich, and Q.-S. Chen (1997). Comparison of accumulation and precipitation maps of the Greenland Ice Sheet. *Eos. Trans. AGU, Fall Meet. Suppl. 78*.

Cubasch, U., G. Meehl, G. Boer, R. Stouffer, M. Dix, A. Noda, C. Senior, S. Raper, and K. Yap (2001). *Projections of future climate change, in Climate Change, 2001: The Scientific Basis, Contribution of Working Group 1 to the Third Assessment Report of the Intergovernmental Panel on Climate Change*. edited by J. Houghton et al., Cambridge Univ. Press, New York.

Cuffey, K. M. and G. C. Clow (1997). Temperature, accumulation, and ice sheet elevation in central Greenland through the last deglacial transition. *J. Geophys. Res. 102*, 26,383–26,396.

Dansgaard, W., S. J. Johnsen, H. B. Clausen, D. Dahl-Jensen, N. S. Gundestrup, C. U. Hammer, C. S. Hvidberg, J. P. Steffensen, A. E. Sveinbjörnsdottir, J. Jouzel, and G. Bond (1993). Evidence for general instability of past climate from a 250-kyr ice-core record. *Nature 364*, 218–330.

Davidson, C. L., T. C. Chu, M. A. Grimm, N. A. Nasta, and M. P. Qamoos (1981). Wet and dry deposition of trace elements onto the Greenland ice sheet. *Atmos. Environ. 15*, 1429–1437.

Dorman, L. (2004). *Cosmic Rays in the Earth's Atmosphere and Underground.* Dordrecht: Kluwer Academic Publishers.

Ebisuzaki, W. (1997, September). A method to estimate the statistical significance of a correlation when the data are serially correlated. *J. Climate 10*, 2147–2153.

Eddy, J. A. (1976). The Maunder Minimum. *Science 192*, 1189–1202.

Ellison, D. and R. Ramaty (1985). Shock acceleration of electrons and ions in solar flares. *Astrophys. J. 298*, 400–408.

Fassò, A., A. Ferrari, J. Ranft, and P. Sala (2001). Fluka: Status and prospective of hadronic applications. In A. K. et al. (Ed.), *Proc. Monte Carlo 2000 Conf.*, pp. 955–960. Berlin: Springer.

Field, C. V., G. A. Schmidt, D. Koch, and C. Salyk (2006). Modeling production and climate-related impacts on ^{10}Be concentration in ice cores. *J. Geophys. Res. 111*, D15107, doi:10.1029/2005JD006410.

Field, C. V., G. A. Schmidt, and D. T. Shindell (2009). Interpreting ^{10}Be changes during the Maunder Minimum. *J. Geophys. Res. 114*, D02113, doi:10.1029/2008JD010578.

Finkel, R. C. and K. Nishiizumi (1997). Beryllium-10 concentrations in the Greenland Ice Sheet Project 2 ice core from 3–40 ka. *J. Geophy. Res. 102*, 26,699–26,706.

Fortuin, J. P. F. (1992). *The surface mass balance and temperature of Antarctica.* Ph. D. thesis, Universiteit Utrecht, Utrecht, Netherlands.

Foukal, P., C. Frohlich, H. Spruit, and T. M. L. Wigley (2006). Variations in solar luminosity and their effect on Earth's climate. *Nature 443*, doi:10.1038/nature05072.

Foukal, P., G. North, and T. Wigley (2004). A stellar view on solar variations and climate. *Science 306*, 69–69.

Free, M. and A. Robock (1999). Global warming in the context of the Little Ice Age. *J. Geophys. Res. 104*, 19,057–19,070.

Fröhlich, C. (2004). Solar Irradiance Variability, in Solar Variability and its Effect on climate, Chapter 2: Solar Energy Flux Variations. *American Geophysical Union, Geophysical Monograph Series 141*, 97–110.

Genthon, C. (1994). Antarctic modeling with general circulation models of the atmosphere. *J. Geophys. Res. 99*, 12,953–12,961.

Gillett, N. P., M. R. Allen, R. E. McDonald, C. A. Senior, D. T. Shindell, and G. A. Schmidt (2002). How linear is the Arctic Oscilliation response to greenhouse gases? *J. Geophys. Res. 107*, D3, 10.1029/2001JD000589.

Giovinetto, M. B., N. M. Walters, and C. R. Bentley (1990). Dependence of Antarctic surface mass balance on temperature, elevation and distance to open ocean. *J. Geophys. Res. 95*, 3517–3531.

Gleeson, L. J. and W. I. Axford (1968). Solar modulation of galactic cosmic rays. *Astrophys. J. 154*, 1011–1018.

Haigh, J. D. (1996). The impact of solar variability on climate. *Science 272*, 981–984.

Hanna, E., P. Valdes, and J. McConnell (2001). Patterns and variations of snow accumulation over Greenland, 1979-98 from ECMWF analysis, and their verification. *J. Clim. 14*, 3521–3535.

Hansen, J. E., L. Nazarenko, R. Ruedy, M. Sato, J. Willis, A. D. Genio, D. Koch, A. Lacis, K. Lo, S. Menon, T. Tovakov, J. Perlwitz, G. Russel, G. A. Schmidt, and N. Tausnev (2005). Earth's energy imbalance: Confirmation and implications. *Science 308*, 1431–1435.

Hansen, J. E., R. Ruedy, M. Sato, M. Imhoff, W. Lawrence, D. Easterling, T. Peterson, and T. Karl (2001). 2001: A closer look at United States and global surface temperature change. *J. Geopys. Res. 106*, doi:10.1029/2001JD000354.

Heck, D., J. Knapp, J. Capdevielle, G. Schatz, and T. Thouw (1998). *CORSIKA: A Monte Carlo code to simulate extensive air showers*. Karlsruhe: FZKA 6019, Forschungszentrum.

Heikkilä, U., J. Beer, and J. Feichter (2008). Modeling cosmogenic radionuclides $^{1}0$Be and ^{7}Be during the Maunder Minimum using the ECHAM5-HAM General Circulation Model. *Atmos. Chem. Phys. 7*, 2797–2809.

Horiuchi, K., T. Uchida, Y. Sakamoto, A. Ohta, H. Matsuzaki, Y. Shibata, and H. Motoyama (2008). Ice core record of ^{10}Be over the past millennium from Dome Fuji, Antarctica: A new proxy record of past solar activity and a powerful tool for stratigraphic dating. *Quat. Geochrono. 3*, 253–261.

Hoyt, D. V. and K. H. Schatten (1993). A discussion of plausible solar irradiance variations, 1700-1992. *J. Geophy. Res. 98*, 18,895–18,906.

Hoyt, D. V. and K. H. Schatten (1998). Group sunspot numbers: A new solar activity reconstruction. *Solar Phys. 179*, 189–219.

IPCC (2007). *Climate Change 2007 - The Physical Science Basis, Contribution of Working Group I to the Fourth Assessment Report of the IPCC*. Cambridge: Cambridge University Press.

Johnsen, S. J., D. Dahl-Jensen, W. Dansgaard, and N. Gundestrup (1995). Greenland paleotemperatures derived from GRIP core hole temperature and ice isotope profiles. *Tellus 47*, 624–629.

Jones, P. D., K. R. Briffa, T. P. Barnett, and S. F. B. Tett (1998). High-resolution paleoclimatic records fo rhte last millennnium: interpretation, integration and comparison with General Circulation Model control-run temperatures. *Holocene 8*, 455–471.

Jones, P. D. and M. E. Mann (2004). Climate over past millennia. *Revs. Geophys. 42*, RG2002, doi:10.1029/2003RG000143.

Jordan, C. E., J. E. Dibb, and R. C. Finkel (2003). ^{10}Be/^{7}Be tracer of atmospheric transport and stratosphere-troposphere exchange. *J. Geophy. Res. 108*, No. D8, 4234, doi:10.1029/2002JD002395.

Kay, S. (1988). *Modern Spectral Estimation: Theory and Application*. New Jersey: Prentice Hall.

Koch, D., D. Jacob, I. Tegen, D. Rind, and M. Chin (1999). Tropospheric sulfur simulation and sulfate direct radiative forcing in the Goddard Institute for Space Studies general circulation model. *J. Geophy. Res. 104*, 23,799–23,822.

Koch, D., G. A. Schmidt, and C. Field (2006). Sulfur, sea salt and radionuclide aerosols in GISS modelE. *J. Geophys. Res. 111*, D06206, doi:10.1029/2004JD005550.

Koch, D. M., D. J. Jacob, and W. C. Graustein (1996). Vertical transport of aerosols in the troposphere as indicated by ^{7}Be and ^{210}Pb in a chemical tracer model. *J. Geophy. Res. 101*, 18,651–18,666.

Koch, D. M., D. J. Jacob, and W. C. Graustein (1996). Vertical transport of tropospheric aerosols as indicated by ^{7}Be and ^{210}Pb in a chemical tracer model. *J. Geophys. Res. 101*, 18651–18666.

Koch, D. M. and M. E. Mann (1996). Spatial and temporal variability of ^{7}Be surface concentrations. *Tellus 48B*, 387–396.

Koch, D. M. and D. Rind (1998). Beryllium 10/beryllium 7 as a tracer of stratospheric transport. *J. Geophy. Res. 103*, 3907–3917.

Kolb, W. (1992). *Aktivitatskonzentrationen von Radionukliden in der bodennahen Luft Norddeutschlands und Nordnorwegens im Zeitraum von 1963 bis 1990*. In PTB-Ber. Ra-29, Phys.-Tech. Bundesanst. Braunschweig, Germany.

Kollár, D., I. Leya, J. Masarik, and R. Michel (2000). Calculation of cosmogenic nuclide production rates in the earth atmosphere and in terrestrial surface rocks using improved neutron cross sections. *Meteorit. Planet. Sci., Supplement 35*, A90.

Kulan, A., A. Aldahan, G. Possnert, and I. Vintersved (2006). Distribution of ^{7}Be in surface air of Europe. *Atmos. Envir. 40*, 3855–3868.

Lal, D. (1987). ^{10}Be in polar ice: data reflect changes in cosmic ray flux or polar meteorology. *Geophys. Res. Lett. 14*, 785–788.

Lal, D. and B. Peters (1962). Cosmic ray produced isotopes and their application to problems in geophysics. In J. Wilson and S. Wouthuysen (Eds.), *Progress in Elementary Particle and Cosmic Ray Physics*, Volume 6, pp. 77–243. Amsterdam: North Holland.

Lal, D. and B. Peters (1967). Cosmic ray produced radioactivity on the Earth. *Handb. Phys. 46*, 551–612.

Land, C. and J. Feichter (2003). Stratosphere-troposphere exchange in a changing climate simulated with the general circulation model MAECHAM4. *J. Geophys. Res. 108*, doi:10.1029/2002JD002543.

Langematz, U., A. Claussnitzer, K. Matthes, and M. Kunze (2005). The climate during the Maunder Minimum: a simulation with the Freie Universitat Berlin Climate Middle Atmosphere Model (FUB-CMAM). *J. Atmos. Solar-Terr. Phys. 67*, 55–69.

Lean, J. (1994). Solar forcing of global change. In *The Solar Engine and Its Influence on Terrestrial Atmosphere and Climate*, Volume 25 of *NATO ASI Ser.*, pp. 163–184. Springer Verlag.

Lean, J. (2000). Evolution of the sun's spectral irradiance since the maunder minimum. *Geophys. Res. Lett. 27*, 2425–2428.

Lean, J., J. Beer, and R. Bradley (1995). Reconstruction of solar irradiance since 1610: Implications for climate change. *Geophys. Res. Lett. 22*, 3195–3198.

Lean, J. L., Y.-M. Wang, and J. N. R. Sheeley (2002). The effect of increasing solar activity on the Sun's total and open magnetic flux during multiple cycles: Implications for solar forcing of climate. *Geophys. Res. Lett. 29*, 77–1 – 77–4.

LeGrande, A. N., G. A.Schmidt, D. T. Shindell, C. V. Field, R. L. Miller, D. M. Koch, G. Faluvegi, and G. Hoffmann (2006). Consistent simulations of multiple proxy responses to an abrupt climate change event. *Proc. Natl. Acad. Sci. 103*, 837–842, doi:10.1073pnas.0510095103.

Liu, H., D. J. Jacob, I. Bey, and R. M. Yantosca (2001, June). Constraints from ^{210}Pb and [7]Be on wet deposition and transport in a global three-dimensional chemical tracer model driven by assimilated meteorological fields. *J. Geophys. Res. 106*, 12109–12128.

Lockwood, J. A., H. Debrunner, E. O. Flueckiger, and H. Graedel (1990). Proton energy spectra at the sun in the solar cosmic-ray events on 1978 may 7 and 1984 february 16. *Astrophys. J. 355*, 287–294.

Luterbacher, J., D. Dietrich, E. Xoplaki, M. Grosjean, and H. Wanner (2004). European seasonal and annual temperature variability, trends, and extremes since 1500. *Science 303*, 1499–1503.

Mann, G. W., P. S. Anderson, and S. D. Mobbs (2000). Profile measurements of blowing snow at Halley, Antarctica. *J. Geophys. Res. 105*, 24,491–24,508.

Mann, M. E., R. S. Bradley, and M. K. Hughes (1999). Northern hemisphere temperatures during past millenium: Inferences, uncertainties and limitations. *Geophys. Res. Lett. 26*, 759–762.

Masarik, J. and J. Beer (1999). Simulation of particle fluxes and cosmogenic nuclide production in the Earth's atmosphere. *J. Geophys. Res. 104*, 12,099–12,111.

Masarik, J. and R. C. Reedy (1995). Terrestrial cosmogenic-nuclide production systematic calculated from numerical simulations. *Earth Planet. Sci. Lett. 136*, 381–395.

Mathews, S. and J. Schulze (2001, May). The radionuclide monitoring system of the Comprehensive-Nuclear Test Ban Treaty Organisation: from sample to product. *Kerntechnik 66*, 102–112.

Mazaud, A., C. Laj, and M. Bender (1994). A geomagnetic chronology for Antarctic ice accumulation. *Geophys. Res. Lett. 21*, 337–340.

McConnell, J. R., R. C. Bales, and D. R. Davis (1997). Recent intra-annual snow accumulation at South Pole: Implications for ice core interpretation. *J. Geophys. Res. 102*, 21,947–21,954.

McCracken, K. G. (2004). Geomagnetic and atmospheric effects upon the cosmogenic [10]Be observed in polar ice. *J. Geophys. Res. 109*, A12103, doi:10.1029/2003JA010060.

McCracken, K. G. and B. Heikkila (2003). The cosmic ray intensity between 1933 and 1965. In *Proc. 28th Int. Cosmic Ray Conf.*, pp. 4117–4120. Univ. Acad. Press, Tokyo.

McCracken, K. G., F. B. McDonald, J. Beer, G. Raisbeck, and F. Yiou (2004). A phenomenological study of the long-term cosmic ray modulation 850-1958 ad. *J. Geophys. Res. 109*, A12103, doi:10.1029/2004JA010685.

McHargue, L. R. and P. E. Damon (1991). The global beryllium 10 cycle. *Revs. Geophys. 29*, 141–158.

Medici, F. (2001). Particulate sampling in the IMS radionuclide network of the Comprehensive-Nuclear Test Ban Treaty. *Kerntechnik 66*, 121–125.

Mewaldt, R. A. (2006). Solar energetic particle composition, energy spectra, and space weather. *Space Sci. Rev. 124*, 303–316.

Miller, R. L., G. A. Schmidt, and D. T. Shindell (2006). Forced annular variations in the 20th century Intergovernmental Panel on Climate Change Fourth Assessment Report models. *J. Geophys. Res. 111*, D18101, doi:10.1029/2005JD006323.

Mironova, I. A., D. Desorgher, I. G. Usoskin, E. Flückiger, and R. Bütikofer (2008). Variations of aerosol optical properties during the extreme solar event in January 2005. *Geophys. Res. Lett. 35*.

Monaghan, A. J. et al. (2006). Insignificant change in Antarctic snowfall since the International Geophysical Year. *Science 313*, doi:10.1126/science.1128243.

Morse, D. L., E. D. Waddington, H.-P. Marshall, T. A. Neumann, E. J. Steig, J. E. Dibb, D. P. Winebrenner, and R. J. Arthern (1999). Accumulation rate measurements at Taylor Dome, East Antarctica: techniques and strategies for mass balance measurements in polar environments. *Geograf. Ann. 81*, 683–694.

Mosley-Thompson, E., J. R. McConnell, R. C. Bales, Z. Li, P.-N. Lin, K. Steffen, L. G. Thompson, R. Edwards, and D. Bathke (2001). Local to regional-scale variability of annual net accumulation on the Greenland ice sheet from PARCA cores. *J. Geophys. Res. 106*, 33839–33851.

Mosley-Thompson, E., J. F. Paskievitch, A. J. Gow, and L. G. Thompson (1999). Late 20th Century increase in South Pole snow accumulation. *J. Geophys. Res. 104*, 3877–3886.

Mosley-Thompson, E., L. G. Thompson, J. F. Paskievitch, M. Pourchet, A. J. Gow, M. E. Davis, and J. Kleinman (1995). South pole snow accumulation has increased in recent decades. *Ann. Glaciol. 21*, 131–138.

Mursula, K., I. G. Usoskin, and G. A. Kovaltsov (2003). Reconstructing the long-term cosmic ray intensity: linear relations do not work. *Ann. Geophys. 21*, 863–867.

Muscheler, R., J. Beer, P. W. Kubik, and H.-A. Synal (2004). Geomagnetic field intensity during the last 60,000 years based on ^{10}Be and ^{36}Cl from the summit ice cores and ^{14}C. *Quat. Sci. Rev. 24*, 1849–1860.

Muscheler, R., J. Beer, and M. Vonmoos (2004). Causes and timing of the 8200 yr BP event inferred from the comparison of the grip ^{10}Be and the tree ring ^{14}C record. *Quat. Sci. Rev. 23*, 2101–2111.

Muscheler, R., J. Beer, G. Wagner, and R. C. Finkel (2000). Changes in deep-water formation during the Younger Dryas event inferred from ^{10}Be and ^{14}C records. *Nature 408*, 567–570.

Muscheler, R., F. Joos, J. Beer, S. A. Muller, M. Vonmoos, and I. Snowball (2007). Solar activity during the last 1000 yr inferred from radionuclide records. *Quat. Sci. Rev. 26*, doi:10.1016/j.quascirev.2006.07.012.

Muscheler, R., F. Joos, S. A. Müller, and I. Snowball (2005). How unusual is today's solar activity? *Nature 436*, doi:10.1038/nature04045.

Nagai, H., W. Tada, and T. Kobayashi (2000). Production rates of ^{7}be and ^{10}be in the atmosphere. *Nucl. Instrum. Meth. Phys. Res.B 172*, 796–801.

O'Brien, K. (1979). Secular variations in the production of cosmogenic isotopes in the Earth's atmosphere. *J. Geophys. Res. 84*, 423–431.

O'Brien, K., H. A. Sandmeier, G. Hansen, and J. E. Campbell (1963). Cosmic-ray induced neutron background sources and fluxes for geometries of air over water, ground, iron, and aluminum. *J. Geophys. Res. 84*, 423–431.

O'Brien, K., H. A. Sandmeier, G. E. Hansen, and J. E. Campbell (1978). Cosmic-ray induced neutron background sources and fluxes for geometries of air over water, ground, iron, and aluminum. *J. Geophys. Res. 83*, 114–120.

Oeschger, H., J. Houtermann, H. Loosli, and M. Wahlen (1969). *The constancy of cosmic radiation from isotope studies in meteorites and on the Earth, in Radiocarbon Variations and Absolute Chronology*. Edited by I. Olsen, John Wiley, New York.

Ohmura, A. and N. Reeh (1991). New precipitation and accumulation maps for Greenland. *J. Glaciol. 37*, 140–148.

Overpeck, J., K. Hughen, D. Hardy, R. Bradley, R. Case, M.Douglas, B. Finney, K. Gajewski, G. Jacoby, A. Jennings, S. Lamoureux, A. Lasca, G. MacDonald, J. Moore, M. Retelle, S. Smith, A. Wolfe, and G. Zielinski (2004). Arctic environmental changes of the last four centuries. *Science 278*, 1251–1256.

Palmer, M. A., L. J. Gray, M. R. Allen, and W. A. Norton (2004). Solar forcing of climate: model results. *Adv. Space Res. 34*, 343–348.

Phillips, G. W., G. H. Share, S. E. King, R. A. August, A. J. Tylka, J. H. Adams, M. I. Panasyuk, R. A. Nymmik, B. M. Kuzhevskij, V. S. Kulikauskas, D. A. Zhuravlev, A. R. Smith, D. L. Hurley, and R. J. McDonald (2001). Correlation of upper-atmospheric [7]be with solar energetic particle events. *Geophys. Res. Lett. 28*, 939–942.

Plainaki, C., A. Belov, E. Eroshenko, H. Mavromichalaki, and V. Yanke (2007). Modeling ground level enhancements: Event of 20 January 2005. *J. Geophys. Res. 112*, 04102.

Radick, R. R., G. W. Lockwood, and S. L. Baliunas (1990). Stellar Activity and Brightness Variations: A Glimpse at the Sun's History. *Science 247*, 39–44.

Raisbeck, G. M. and F. Yiou (2004). Comment on "Millennium Scale Sunspot Number Reconstruction: Evidence for an Unusually Active Sun Since the 1940s". *Phys. Rev. Lett. 92*, 199001–1.

Raisbeck, G. M., F. Yiou, D. Bourles, C. Lorius, J. Jouzel, and N. I. Barkov (1987). Evidence for two intervals of enhanced ^{10}Be in Antarctic ice during the last glacial period. *Nature 326*, 273–277.

Raisbeck, G. M., F. Yiou, M. Fruneau, J. M. Loiseaux, M. Lieuvin, and J. C. Ravel (1981). Cosmogenic ^{10}Be/^{7}Be as a probe of atmospheric transport processes. *Geophys. Res. Lett. 8*, 1015–1018.

Raisbeck, G. M., F. Yiou, M. Fruneau, J. M. Loiseaux, M. Lieuvin, J. C. Ravel, and C. Lorius (1981). Cosmogenic ^{10}Be concentrations in Antarctic ice during the past 30,000 years. *Nature 292*, 825–826.

Raisbeck, G. M., F. Yiou, J. Jouzel, J. R. Petit, N. O. Weiss, J. Alsop, and G. de Q. Robin (1990). ^{10}Be and δ^2H in polar ice cores as a probe of the solar variability's influence on climate. *Phil. Trans. Roy. Soc. 330*, 463–470.

Rasch, P. J., J. Feichter, K. Law, N. Mahowald, J. Penner, C. Benkovitz, C. Genthon, C. Giannakopoulos, P. Kasibhatla, D. Koch, H. Levy, T. Maki, M. Prather, D. L. Roberts, G.-J. Roelofs, D. Stevenson, Z. Stockwell, S. Taguchi, M. Kritz, M. Chipperfield, D. Baldocchi, P. McMurry, L. Barrie, Y. Balkanski, R. Chatfield, E. Kjellstrom, M. Lawrence, H. N. Lee, J. Lelieveld, K. J. Noone, J. Seinfeld, G. Stenchikov, S. Schwartz, C. Walcek, and D. Williamson (2000). A comparison of scavenging and deposition processes in global models: Results from the WCCRP Cambridge Workshop of 1995. *Tellus 52B*, doi:10.1034/j.1600–0889.2000.00980.

Ribes, J. C. and E. Nesme-Ribes (1993). The solar sunspot cycle in the Maunder Minimum AD 1645 to AD 1715. *Astron. Astrophys. 276*, 549–563.

Rind, D., P. Demenocal, G. L. Russell, S. Sheth, D. Collins, G. A. Schmidt, and J. Teller (2001). Effects of glacial meltwater in the GISS Coupled Atmosphere-Ocean Model: Part I: North Atlantic Deep Water response. *J. Geophys. Res. 106*, 27,335–27,354.

Rind, D., J. Lerner, J. Jonas, and C. McLinden (2007). Effects of resolution and model physics on tracer transports in the NASA Goddard Institute for Space Studies general circulation models. *J. Geophys. Res. 112*, D09315, doi:10.1029/2006JD007476.

Rind, D., J. Lerner, K. Shah, and R. Suozzo (1999). Use of on-line tracers as a diagnostic tool in general circulation model development 2. Transport between the troposphere and stratosphere. *J. Geophys. Res. 104*, 9151–9167.

Rodrigo, F. S., D. Pozo-Vazquez, M. J. Esteban-Parra, and Y. Castro-Diez (2001). A reconstruction of the winter North Atlantic Oscillation index back to A.D. 1501 using documentary data from southern Spain. *J. Geophys. Res. 106*, 14805–14818.

Rossow, W. B. and R. A. Schiffer (1999). Advances in understanding clouds from ISCCP. *Bull. Amer. Meteor. Soc. 80*, 2261–2288.

Sato, M., J. Hansen, M. McCormick, and J. Pollack (1993). Stratospheric aerosol optical depths, 1850–1990. *J. Geophys. Res. 98*, 22,987–22,994.

Schmidt, G. A., R. Ruedy, J. E. Hansen, I. Aleinov, N. Bell, M. Bauer, S. Bauer, B. Cairns, V. Canuto, Y. Cheng, A. DelGenio, G. Faluvegi, A. D. Friend, T. M. Hall, Y. Hu, M. Kelley, N. Y. Kiang, D. Koch, A. A. Lacis, J. Lerner, K. K. Lo, R. L. Miller, L. Nazarenko, V. Oinas, J. Perlwitz, J. Perlwitz, D. Rind, A. Romanou, G. L. Russell, M. Sato, D. T. Shindell, P. H. Stone, S. Sun, N. Tausnev, D. Thresher, and M.-S. Yao (2006). Present day atmospheric simulations using GISS ModelE: Comparison to in-situ, satellite and reanalysis data. *J. Clim. 19*, 153–192, doi:10.1175/JCLI3612.1.

Schwander, J., T. Sowers, J. M. Barnola, T. Blunier, A. Fuchs, and B. Malaize (1997). Age scale of the air in the summit ice: Implications for glacial-interglacial temperature changes. *J. Geophys. Res. 102*, 19483–19493.

Severinghaus, J. P., T. Sowers, E. J. Brook, R. B. Alley, and M. L. Bender (1998). Timing of abrupt climate change at the end of the younger dryas interval from thermally fractionated gases in polar ice. *Nature 391*, 141–146.

Share, G. H., R. J. Murphy, B. R. Dennis, R. A. Schwartz, A. K. Tolbert, R. P. Lin, and D. M. Smith (2002). Rhessi observation of atmospheric gamma rays from impact of solar energetic particles on 21 april 2002. *Solar Phys. 210*, 357–372.

Shindell, D. T., G. Faluvegi, R. L. Miller, G. A. Schmidt, J. E. Hansen, and S. Sun (2006). Solar and anthropogenic forcing of tropical hydrology. *Geophys. Res. Lett. 33*, L24706, doi:10.1029/2006GL027468.

Shindell, D. T., G. Faluvegi, N. Unger, E. Aguilar, G. A. Schmidt, D. M. Koch, S. E. Bauer, and R. L. Miller (2006). Simulations of preindustrial, present-day, and 2100 conditions in the NASA GISS composition and climate model G-PUCCINI. *Atmos. Chem. Phys. 6*, 4427–4459.

Shindell, D. T., R. L. Miller, G. A. Schmidt, and L. Pandolfo (1999). Simulation of recent northern winter climate trends by greenhouse-gas forcing. *Nature 399*, 452–455.

Shindell, D. T., D. Rind, N. Balachandran, J. Lean, and P. Lonergan (1999). Solar cycle variability, ozone, and climate. *Science 284*, 305–308.

Shindell, D. T., G. A. Schmidt, M. E. Mann, and G. Faluvegi (2004). Dynamic winter climate response to large tropical volcanic eruptions since 1600. *J. Geophys. Res. 109*, doi:10.1029/2003JD004151.

Shindell, D. T., G. A. Schmidt, M. E. Mann, D. Rind, and A. Waple (2001). Solar forcing of regional climate change during the Maunder Minimum. *Science 294*, 2149–2152.

Shindell, D. T., G. A. Schmidt, R. L. Miller, and M. E. Mann (2003). Volcanic and solar forcing of climate changes during the preindustrial era. *J. Clim. 16*, 4094–4107.

Steig, E. J., E. J. Brook, J. W. C. White, C. M. Sucher, M. L. Bender, S. J. Lehman, D. L. Morse, E. D. Waddington, and G. D. Clow (1998). Synchronous climate changes in Antarctica and the North Atlantic. *Science 282*, 92–95.

Steig, E. J., D. L. Moore, E. D. Washington, and P. J. Polissar (1998). Using the sunspot cycle to date ice cores. *Geophys. Res. Lett. 25*, 163–166.

Steig, E. J., D. L. Morse, E. D. Waddington, M. Stuiver, and P. M. Grootes (2000). Wisconsinan and Holocene climate history from an ice core at Taylor Dome, western Ross Embayment, Antarctica. *Geograf. Ann. 82*, 213–235.

Steig, E. J., P. J. Polissar, M. Stuiver, P. M. Grootes, and R. C. Finkel (1996). Large amplitude solar modulation cycles of [10]Be in Antarctica: Implications for atmospheric mixing processes and interpretation of the ice core record. *Geophys. Res. Lett. 23*, 523–526.

Steinhilber, F., J. A. Abreu, and J. Beer (2008). Solar modulation during the Holocene. *Astrophys. Space Sci. Trans. 4*, 1–6.

Stoker, P. H. (1995). Relativistic solar proton events. *Space Sci. Rev. 73*, 327–385.

Stuiver, M. and P. D. Quay (1980). Changes in atmospheric C-14 attributed to a variable sun. *Science 207*, 11–19.

Textor, C., M. Schulz, S. Guibert, S. Kinne, S. E. Bauer, Y. Balkanski, T. Berntsen, T. Berglen, O. Boucher, M. Chin, F. Dentener, T. Diehl, H. Feichter, D. Fillmore, S. Ghan, T. Iversen, A. Kirkevag, D. Koch, J. E. Kristjansson, M. Krol, A. Lauer, J. F. Lamarque, X. Liu, V. Montanaro, G. Myhre, J. Penner, G. Pitari, S. Reddy, O. Seland, P. Stier, T. Takemura, and X. Tie (2005). Analysis and quantification of the diversities of aerosol life cycles within AEROCOM. *Atmos. Chem. Phys. 7*, 4489–4501.

Tzeng, R.-Y., D. H. Bromwich, T. R. Parish, and B. Chen (1994). NCAR CCM2 simulation of the modern Antarctic climate. *J. Geophys. Res. 99*, 23131–23148.

Ungar, K., W. Zhang, P. Aarnio, J. Ala-Heikkila, H. Toivonen, T. Siiskonen, A. Isolankila, A. Kuusi, M. Moring, and M. Nikkinen (2007). Automation of analysis of airborne radionuclides observed at Canadian CTBT radiological networks using LINSSI. *J. Radioanalyt. Nucl. Chem. 272*, 285–291.

Usoskin, I. G., K. Alanko-Huotari, G. A. Kovaltsov, and K. Mursula (2005). Heliospheric modulation of cosmic rays: Monthly reconstruction for 1951-2004. *J. Geophys. Res. 110*, 12108.

Usoskin, I. G., L. Desorgher, P. Velinov, M. Storini, E. O. Flückiger, R. Bütikofer, and G. A. Kovaltsov (2009). Ionization of the earth's atmosphere by solar and galactic cosmic rays. *Acta Geophysica 57*, 88–101.

Usoskin, I. G. and G. A. Kovaltsov (2006, November). Cosmic ray induced ionization in the atmosphere: Full modeling and practical applications. *J. Geophys. Res. 111*, 21206.

Usoskin, I. G. and G. A. Kovaltsov (2008). Production of cosmogenic ^{7}be isotope in the atmosphere: Full 3-D modeling. *J. Geophys. Res. 113*, doi:10.1029/2007JD009725.

van der Veen, C. J., E. Mosley-Thompson, A. J. Gow, and B. G. Mark (1999). Accumulation at South Pole: Comparison of two 900-year records. *J. Geophys. Res. 104*, 31067–31076.

Vinther, B. M. et al. (2006). A synchronized dating of three Greenland ice cores throughout the Holocene. *J. Geophys. Res. 111*, D13102, doi:10.1029/2005JD006921.

von Grafenstein, U., H. Erlenkeuser, J. Miller, J. Jouzel, and S. Johnsen (1998). The cold event 8200 years ago documented in oxygen isotope records of precipitation in Europe and Greeland. *Clim. Dyn. 14*, 73–81.

Vonmoos, M., J. Beer, and R. Muscheler (2006). Large variations in holocene solar activity: Constraints from ^{10}Be in the greenland ice core project ice core. *J. Geophys. Res. 111*, doi:10.1029/2005JA011500.

Wagnon, P., R. J. Delmas, and M. Legrand (1999). Loss of volatile acid species from upper firn layers at Vostok, Antarctica. *J. Geophys. Res. 104*, 3423–3431.

Webber, W. R. and P. R. Higbie (2003). Production of cosmogenic Be nuclei in the earth's atmosphere by cosmic rays: Its dependence on solar modulation and the interstellar cosmic ray spectrum. *J. Geophys. Res. 108*, doi:10.1029/2003JA009863.

Webber, W. R., P. R. Higbie, and K. G. McCracken (2007). Production of the cosmogenic isotopes ^{3}H, ^{7}Be, ^{10}Be, and ^{36}Cl in the Earth's atmosphere by solar and galactic cosmic rays. *J. Geophys. Res. 112*.

Wesely, M. L. (1989). Parameterization of surface resistances to gaseous dry deposition in regional-scale numerical models. *Atmos. Environ. 23*, 1293–1304.

Wesely, M. L. and B. B. Hicks (1977). Some factors that affect the deposition rates of sulfur dioxide and similar gases on vegetation. *J. Air Pollut. Control Assoc. 27*, 1110–1116.

Willson, R. C. and H. S. Hudson (1988). Solar luminosity variations in solar cycle 21. *Nature 332*, 95–97.

Yiou, F., G. M. Raisbeck, S. Baumgartner, J. Beer, C. Hammer, S. Johnsen, J. Jouzel, P. W. Kubik, J. Lestringuez, M. Stéivenard, M. Suter, and P. Yiou (1997). Beryllium 10 in the Greenland Ice Core Project ice core at Summit, Greenland. *J. Geophy. Res. 102*, 26,783–26,794.

Yoshimori, M. (2005a). Beryllium 7 radionucleide as a tracer of vertical air mass transport in the troposphere. *Adv. Space Res. 36*, 828–832.

Yoshimori, M. (2005b). Production and behavior of beryllium 7 radionuclide in the upper atmosphere. *Adv. Space Res. 36*, 922–926.

Zanis, P., E. Gerasopoulos, A. Priller, C. Schnabel, A. Stohl, C. Zerefos, H. W. Gäggeler, L. Tobler, P. W. Kubik, H. J. Kanter, H. E. Scheel, J. Luterbacher, and M. Berger (2003). An estimate of the impact of stratosphere to troposphere transport (STT) on the lower free tropospheric ozone over the Alps using ^{10}Be and ^{7}Be measurements. *J. Geophy. Res. 108*, 8520, doi:10.1029/202JD002604.